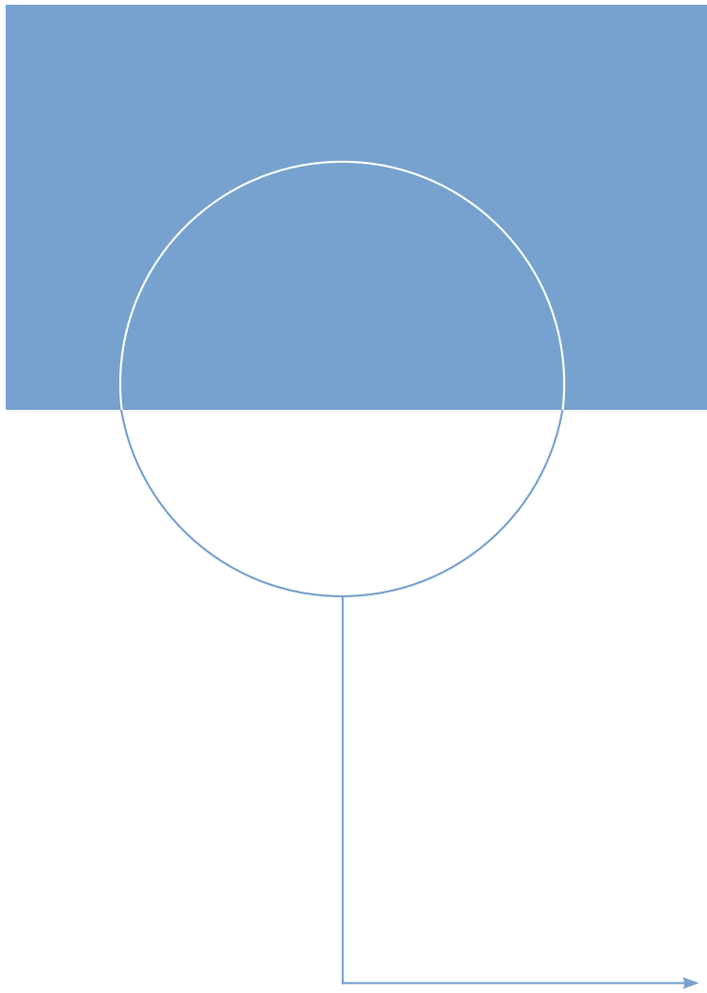

Master's thesis

2022

Sofie Brandtzæg Hårberg

NTNU
Norwegian University of
Science and Technology
Faculty of Natural Sciences
Department of Materials Science and Engineering

Sofie Brandtzæg Hårberg

Spark Plasma Sintering of Silicon Carbide and the Effect of α-SiC and ß-SiC on Sintering Properties

June 2022

NTNU
Norwegian University of
Science and Technology

NTNU
Norwegian University of
Science and Technology

NTNU

Norwegian University of
Science and Technology

Spark Plasma Sintering of Silicon Carbide and the Effect of α-SiC and ß-SiC on Sintering Properties

Sofie Brandtzæg Hårberg

Chemical Engineering and Biotechnology
Submission date: June 2022
Supervisor: Kjell Wlik, IMA
Co-supervisor: Mari-Ann Einarsrud, IMA
Guttorm Syvertsen-Wiig, Washington Mills
Anne Marie Moe, Washington Mills

Norwegian University of Science and Technology
Department of Materials Science and Engineering

Preface

The present study has been conducted as part of the course TMT4900 - Materials Chemistry and Energy Technology, Master's Thesis. The work has been supervised by Prof. Kjell Wiik, with Prof. Mari-Ann Einarsrud, Dr. Guttorm Syvertsen-Wiig and Dr. Anne Marie Moe as co-supervisors. Experiments have been performed at the Department of Material Science and Engineering at NTNU Norwegian University of Science and Technology during the spring 2022, using powders provided by Washington Mills AS. This thesis is a continuation of the specialization project "Spark Plasma Sintering of Silicon Carbide and the Effect of α-SiC and β-SiC on Sintering Properties", performed during the fall 2021 by the same author. The aim of this collaboration has been to establish a method of characterizing α-SiC and β-SiC, and investigate how the difference between the two polytypes may impact the sinterability of a coarse silicon carbide powder.

I would like to express my gratitude to my supervisor, and co-supervisors for the inspiration, weekly guidance, support and help I received throughout this semester. I also want to thank the members of the FACET group at NTNU for interesting discussions, sharing their insights and giving constructive feedback during the last year. I am grateful to the engineers and lab technicians at the Department of Materials Science and Engineering at NTNU for their help and technical support in the lab. A special thanks goes to the team at the XRD lab for running my samples and teaching me the EVA and TOPAS software. I would also like to express my gratitude to Prof. Hilde Lea Lein for taking the time to test the set-up for ball-on-ring testing. I am very grateful to Johannes Ofstad for the invaluable help with the spark plasma sintering. I would not have overcome the challenges I met without his guidance, our discussions and help in the lab. Finally, a big thanks goes to my fellow students and friends for making the last five years of hard work so fun and rewarding. This thesis would not have been the same without any of you.

Abstract

Silicon carbide (SiC) is known for its excellent thermal and mechanical properties, making it useful for a wide range of applications. Properties such as high hardness and strength retention at high temperatures are caused by the high degree of covalent bonding, which is also what makes SiC challenging to sinter. The objective of this study is to investigate the effect of α-SiC and β-SiC additives on the sinterability of a coarse SiC powder by spark plasma sintering. As-received powders and powder mixtures were spark plasma sintered at 1900 °C for 5 min while simultaneously applying a 50 MPa uniaxial pressure. The sintered samples were then characterized according to density, microstructure, phase composition, biaxial strength and hardness.

Phase analyses by X-ray diffraction of the as-received powders established the presence of polytypes 4H, 6H and 15R. Raman spectroscopy of as-received powders confirmed that the 3C polytype was only present in the β-SiC sintering aid. The Raman spectra of sintered samples showed no 3C and it was concluded that the 3C $\rightarrow$ 6H phase transformation had occurred during sintering.

Spark plasma sintering of the coarse SiC powder resulted in a mean relative density of 73 %. Adding 10 wt% α-SiC and 10 wt% β-SiC as sintering aids increased the relative density to 78 % and 76 %, respectively. The particle size of the sintering aids was considered most important for densification purposes. The highest biaxial strength of 21 MPa was observed for samples added β-SiC. This was attributed to better necking between grains due to the 3C $\rightarrow$ 6H phase transformation. The spark plasma sintered samples exhibited homogeneous microstructure with interconnected and open porosity. The improved knowledge of the 3C $\rightarrow$ 6H phase transformation and the correlation between its effect on density and biaxial strength will be a useful tool to obtain the desired properties of future SiC products.

Sammendrag

Silisiumkarbid (SiC) er kjent for sine utmerkede termiske og mekaniske egenskaper, noe som gjør det nyttig innen mange bruksområder. Egenskaper som høy hardhet og styrke ved høy temperatur skyldes de sterke kovalente bindingene, noe som også gjør SiC utfordrende å sintre. Målet med denne studien er å undersøke effekten av å tilsette α-SiC og β-SiC på sintringsegenskapene til et grovt SiC-pulver ved spark plasma sintring. Pulver og pulverblandinger ble spark plasma sintret ved 1900 °C i 5 min samtidig som et 50 MPa enakset trykk ble påført. De sintrede prøvene ble deretter karakterisert i henhold til tetthet, mikrostruktur, fasesammensetning, biaksiell styrke og hardhet.

Faseanalyser ved røntgendiffraksjon av pulverene bekreftet tilstedeværelsen av polytypene 4H, 6H og 15R. Raman spektroskopi av mottatte pulvere bekreftet at 3C-polytypen kun var til stede i sintringshjelpemidlet β-SiC. Ramanspektrene av sintrede prøver viste ikke 3C, og det ble konkludert med at fasetransformasjonen 3C $\rightarrow$ 6H hadde skjedd under sintring.

Spark plasma sintring av det grove SiC-pulveret resulterte i en gjennomsnittlig relativ tetthet på 73 %. Tilsetning av 10 vekt% α-SiC og 10 vekt% β-SiC som sintringshjelpemidler økte den relative tettheten til henholdsvis 78 % og 76 %. Partikkelstørrelsen til sintringshjelpemidlene ble ansett som det viktigste for fortetting under sintring. Den høyeste biaksielle styrken på 21 MPa ble observert for prøver tilsatt β-SiC. Dette ble tilskrevet bedre "necking" mellom korn på grunn av fasetransformasjonen fra 3C $\rightarrow$ 6H. De sintrede prøvene viste homogen mikrostruktur med sammenkoblet og åpen porøsitet. Kunnskapen om faseendringen fra 3C til 6H og hvordan denne påvirker tetthet og biaksiell styrke vil være et nyttig hjelpemiddel for å oppnå ønskede egenskaper i fremtidens SiC-produkter.

Contents

List of Abbreviations

BET	Brunauer, Emmett and Teller
BOR	Ball-on-ring
CNB	Chevron-notched beam
COD	Crystallography open database
CVP	Chemical vapor deposition
EBSD	Electron backscatter diffraction
EC	Evaporation-condensation
FTO	Folded transverse optical
GB	Grain boundary
HV	Vickers hardness
ICDD	International centre of diffraction data
LO	Longitudinal optical
POB	Piston-on-ball
PSD	Particle size distribution
PVC	Polyvinyl chloride
PVT	Physical vapor transport
ROR	Ring-on-ring
SCF	Surface crack in flexure
SD	Surface diffusion
SEM	Scanning electron microscopy
SPS	Spark plasma sintering
SSL	Solid-state lattice
TEM	Transmission electron microscopy
TOPAS	Total pattern analysis solution
VSEPR	Valence-shell electron-pair repulsion
XRD	X-ray diffraction
YSZ	Yttrium stabilized ZrO_2

1 Background

1.1 Motivation

Silicon carbide (SiC), also known as carborundum, was first synthesized in 1891 by Edward G. Acheson. He fused coke and clay by electric heat in an attempt of synthesizing diamonds, but the experiment resulted in blue crystals [1]. These crystals had many similar properties as diamonds and Acheson patented the process, which to this day is used to produce the vast majority of SiC on the market [2].

During the Acheson process different polytypes and qualities of SiC are produced, depending on the temperature and distance from the electrically heated core. Today, more than 250 polytypes have been documented, and these exhibit variations in their properties [3][4]. It is therefore of great interest to find methods of separating the polytypes, and further to establish applications of each polytype. The correlation between the polytypes, although complicated, may become a new and powerful tool to modify material properties if well understood [5].

Compared to most materials, SiC exhibits higher mechanical strength and hardness, combined with low thermal expansion and excellent thermal conductivity. In addition, SiC is chemically inert even at high temperatures, hence SiC can be used as a structural and functional ceramic material [6]. Many of the properties originate from the strong covalent bonding between Si and C. However, this also means that the self-diffusion is low, and densification of SiC by sintering therefore requires a lot of energy. This could either be achieved by adding sintering aids to increase the diffusion or by combining driving forces such as temperature and pressure [7].

While the sinterability of SiC added sintering aids such as boron carbide (B_4C) and $Y_2O_3-Al_2O_3$ has been extensively investigated, the research on pure SiC sinterability is limited [8]. The motivation of this work is therefore to establish a method of identifying the considered polytypes, and investigate the sinterability of coarse SiC only using fine fractions of α-SiC and β-SiC as sintering aids. To overcome the low self-diffusion of SiC a combination of pressure and temperature is applied simultaneously by spark plasma sintering.

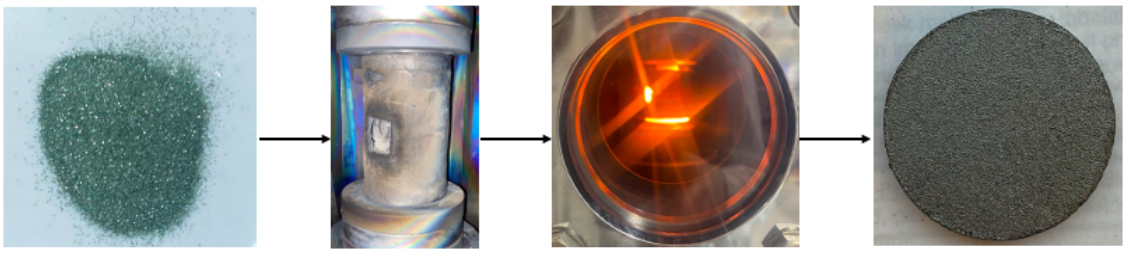

Figure 1.1: The coarse SiC powder, the set-up inside the SPS chamber before and during sintering, and the sintered product.

1.2 Aim and Scope of the Thesis

The primary objective of this work was to assess the properties of spark plasma sintered SiC and separate the effects of using α-SiC and β-SiC as sintering aids. The focus was to successfully sinter pure SiC to cohesive pellets and test the properties, not to obtain a high densities which can compete with existing SiC products added other sintering aids. Powder mixtures were made by mixing a coarse α-SiC powder (60 µm) with 10 wt% α-SiC and β-SiC of approximately the same particle size distribution. The powders were delivered by Washington Mills and their phase composition, microstructure and particle size distribution were investigated as-received.

The powder mixtures and the coarse SiC powder were spark plasma sintered at 1900 °C and 50 MPa for 5 min. The resulting pellets were characterized according to biaxial strength and hardness, and their microstructure, phase composition and density was investigated. The correlation between the results and the type of sintering aid was discussed based on existing theories and research.

2 Introduction

2.1 Silicon Carbide

2.1.1 The Structure of Silicon Carbide

SiC has a stoichiometric ratio of silicon and carbon atoms. Their arrangement corresponds to a framework of silicon atoms with carbon atoms occupying half of the tetrahedral sites. All atoms are bonded to heteroatoms and form tetrahedra, either SiC_4 or CSi_4. The tetrahedra create atomic layers, and depending on the stacking order of these layers the different polytypes of SiC arise [7]. This means that one-dimensional changes in the structure occur without alterations of the stoichiometry, which can be seen by comparing the structures presented in Fig. 2.1 [9]. More than 250 polytypes of SiC have been reported, where the number of layers vary from two to several hundreds [10][4].

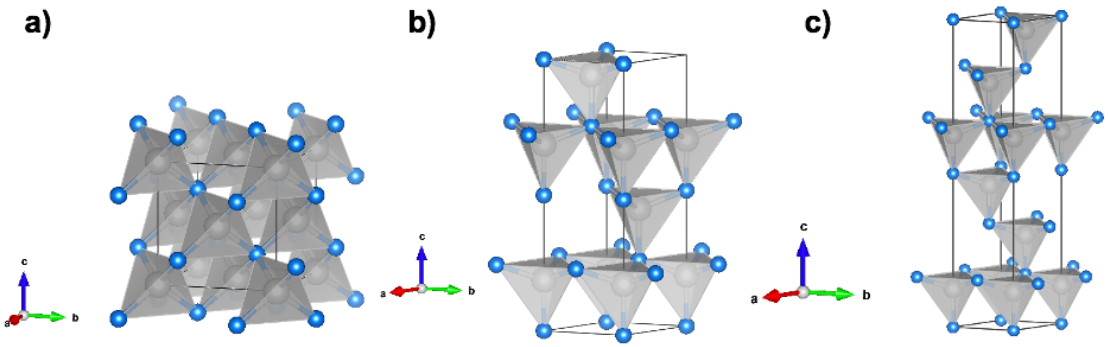

Figure 2.1: The a) 3C (COD-id 1011031), b) 4H(mp-11714) and c) 6H (COD-id 9010158) polytypes of SiC [11]. Carbon atoms are blue and silicon atoms are gray.

Further, twinning also gives rise to different polytypes. This can be explained by looking at the symmetry of a single tetrahedron. Choosing a c-axis along one bond between heteroatoms, as marked by an arrow in Fig. 2.2, there is a threefold rotational symmetry about this axis. A 120° rotation, or any multiple of 120°, would thus lead to an identical structure. Any other rotation would however lead to a twinned structure, as presented in Fig. 2.2 [12]. The only requirement is that two neighbouring tetrahedra share a corner [5].

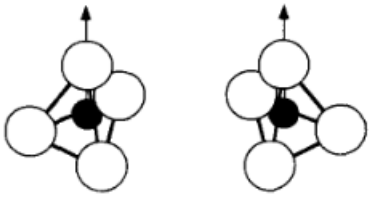

Figure 2.2: An illustration of the Si_4C-tetrahedron with a chosen c-axis along the vertical Si-C-bonds marked by arrows. On the right side the same tetrahedron is rotated 180° around the c-axis, illustrating a twinned version [12].

The most common notation used to classify the SiC polytypes is the Ramsdell notation, where each polytype is assigned a letter and number based on the crystal system and number of layers in the unit cell [9]. The three letters C, R and H are used for cubic, rhombohedral and hexagonal crystal systems, respectively. The only cubic structure, 3C, can be seen in Fig. 2.1a and is generated by stacking the layers of tetrahedra in the same relative orientation. This results in a zinc blende structure (ABCA) and is the only polytype in the category β-SiC. Further, when every second layer of tetrahedra is anti-parallel to the previous layer, hexagonal and rhombohedral structures are formed. A twinned structure is then indicated by a dash in the stacking order, e.g. for 6H, where the order is ABC'A'. The rhombohedral and hexagonal polytypes are referred to as α-SiC. At ambient conditions the most common polytypes include 3C, 4H, 6H and 15R [10][13][4].

Si- and C-atoms have four valence electrons, meaning that every atom can form four covalent bonds to fill the valence shell. The electron density is then enhanced in this region and the VSEPR model can be used to predict the arrangement [14]. As expected for a compound of group IV elements with covalent bonds and sp^3 hybridization, the three-dimensional arrangement is always a tetrahedron [10]. Due to the difference in electronegativity between Si and C there is also an ionic contribution to the bonds. Literature suggests that there is a 12 % ionic contribution, while the remaining 88 % is covalent [7].

2.1.2 The Properties of Silicon Carbide

Selected properties of α- and β-SiC are presented in Table 2.1.

Table 2.1: SiC properties represented by the 6H and 3C structures [6][2][15].

Property	**Unit**	**6H**	**3C**
Physical			
Space group	-	C46v-P63mc	T2d-F43m
Lattice parameter a	[Å]	3.0806	4.3582
Lattice parameter c	[Å]	15.1173	-
Mechanical			
Hardness	[GPa]	32	32
Density	[g/cm^3]	3.166	3.211
Fracture toughness	[MPa$\sqrt{\text{m}}$]	2.5-3	2.5-3
Young's modulus	[GPa]	390-690	310-550
Flexure strength*	[MPa]	450-520	450-520
Thermal			
Thermal expansion coefficient**	[K^{-1}]	$5.8{\cdot}10^{-6}$	$5.8{\cdot}10^{-6}$
Thermal conductivity	[W/cmK]	3.2	4.9
Electrical			
Band gap at 4 K	[eV]	3.023	2.390

* Obtained experimentally on sintered SiC ($\approx$ 2 % porosity) [2].
** Linear thermal expansion from 20-2000°C [16].

The directional and periodic bonding with a high degree of covalency imparts the extreme hardness of 9-9.5 on the Mohs scale [7][17][18]. This bonding, in addition to the differences between the polytypes, governs many of the SiC properties. Other properties of SiC include low density, high thermal conductivity, low thermal expansion and chemical inertness. The combination of these properties makes SiC interesting as an engineering material [12].

The high degree of covalent bonding also leads to a structure which is not close-packed. This facilitates the low thermal expansion, as there is some room within the structure for expansion to occur [2]. Mechanical properties, being dependent on specimen microstructure and configuration of the test method, often varies from material to material [2].

2.1.3 Production of Silicon Carbide

The natural occurrence of SiC is scarce and has only been observed in meteorite rocks. Thus, SiC is man-made through the Acheson process. To achieve this, a mixture of silica and carbon is charged into an Acheson graphite electric resistance furnace as depicted in Fig. 2.3. The furnace is typically cylindrical or u-shaped with carbon electrodes passing a current through the graphite core. The temperature of the core then increases due to resistance heating. The temperature-time cycles vary depending on dimensions, design and desired outcome, but the core is typically heated to 2500 - 3000 °C over a period of two days [19]. The heat provides enough energy for the overall exothermic reaction presented in Eq. (2.1) to occur [4][2][20].

$$\mathrm{SiO_2(s) + 3C(s) \longrightarrow SiC(s) + 2CO(g)} \tag{2.1}$$

The overall reaction is the result of several sub-reactions presented in Eq. (2.2) - Eq. (2.5). The kinetics of these reactions can be controlled by several parameters such as temperature, pressure, grain size, time and amount and type of impurities. Because these sub-reactions involve gaseous phases it is important to note that even though conduction is the main mode of heat transfer, convection also plays an important role [20].

$$\mathrm{SiO_2(s) + C(s) \longrightarrow SiO(g) + CO(g)} \tag{2.2}$$

$$\mathrm{SiO_2(s) + CO(g) \longrightarrow SiO(g) + CO_2(g)} \tag{2.3}$$

$$\mathrm{C(s) + CO_2(g) \longrightarrow 2\,CO(g)} \tag{2.4}$$

$$\mathrm{2\,C(s) + SiO(g) \longrightarrow SiC(s) + CO(g)} \tag{2.5}$$

During firing the core remains carbon, while a high-temperature gradient is developed from the core to the periphery. In the core, where the temperature is highest, high quality crystals are grown [4]. Further out, the size of the crystals decrease in size before reaching a zone with polycrystalline SiC. The process typically produces α-SiC closest to the core with a decreasing size moving outwards, while β-SiC is produced further out where the temperature is lower. The outer layer of the mixture remains unreacted and work as heat insulation. The unreacted part is reused in a new firing [19].

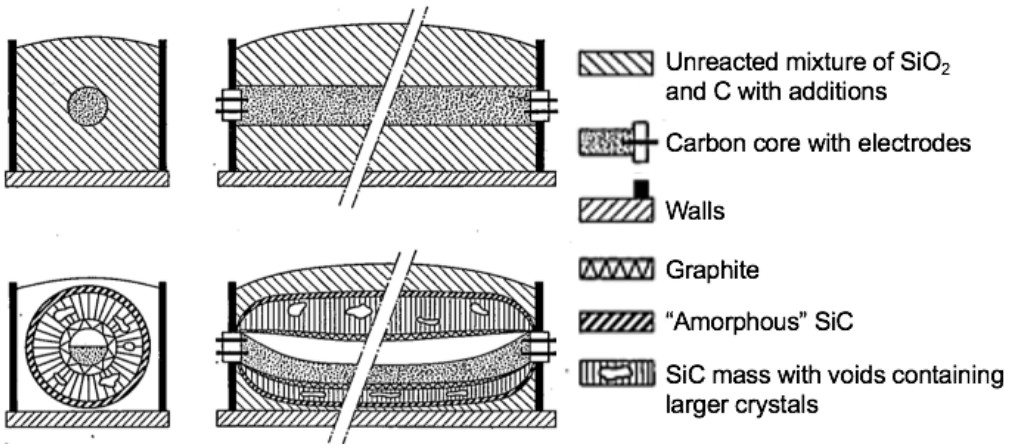

Figure 2.3: Cross section of the Acheson furnace before and after firing with central components and illustration of the reactive zones [19].

The final product is a coarse powder with an inevitable contamination of oxygen. Other impurities that are common include nitrogen, aluminium, free carbon and free silicon. The presence of nitrogen can be seen by a green coloring of the SiC, while aluminium typically leaves a blue/black colour [4]. To achieve a higher purity SiC with less stacking defects, methods such as seeded sublimation growth, chemical vapour deposition (CVP) or sol-gel processing are used. These are typically more time-consuming, costly and challenging to industrialize than the Acheson process, but can provide large SiC single crystals [4][21].

Because different qualities of SiC are synthesized by the Acheson process the products can be used for a variety of applications, such as electronics and abrasives. The commercial yield is 15-19 %, and the process is energy intensive. It is therefore considered an inefficient method. However, as the different zones after firing can be used for different applications, the process is cost-effective.

2.1.4 The Si-C System

In addition to pure carbon and silicon, SiC is the only stable condensed compound that can be formed upon mixing of the two elements. As can be seen from the binary phase diagram of SiC (Fig. 2.4), more than 50 at% C gives a mixture of SiC and graphite, while a majority of Si gives SiC and solid or liquid Si. Further, Fig. 2.4 shows that SiC does not melt, but decomposes peritectically at 2540 °C± 40 °C.

The eutectic temperature is documented to be 1414 °C, and when the temperature exceeds 2830 °C± 40 °C SiC decomposes to graphite and Si-rich vapor [22][10]. Due to the high temperatures there are few experimental data available and amongst the reported phase diagrams there are some variations. Especially the solubility of carbon in liquid silicon when in equilibrium with SiC shows some variations.

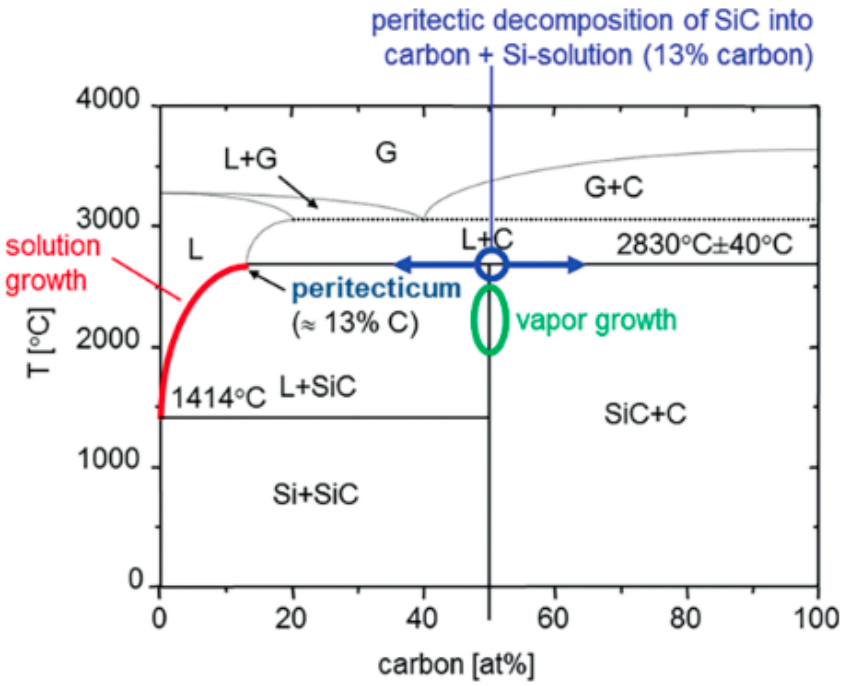

Figure 2.4: The binary phase diagram of the Si-C system with the possible routes of crystal growth [22].

Søiland [23] compared eight studies on the solubility of carbon in liquid Si and concluded that results attained by Hall [24], Ottem [25], Yanaba et al. [26] and Dalaker and Tangstad [27] were the most reliable. The amount of carbon at the peritecticum was observed to vary between 12 - 17 at% in these studies. The variation is caused by the challenge of measuring solubility at such high temperatures, as well as the different set-ups used in the studies. By establishing the solubility curves of C in liquid Si in coexistence with SiC, the behaviour above the peritecticum can be predicted with more certainty [10][23].

2.2 Sintering

The term sintering is used about the process where a powder compact is heated to a temperature that, while still below the melting point, enables material transport and forms a polycrystalline solid [28][29]. From a thermodynamic point of view the sintering is driven by a reduction in free energy, which requires reduction of the surface free energy, application of a pressure or chemical reactions. Further, a mechanism of material transport as well as an energy source to activate and sustain this transport is necessary [2]. The three main types of sintering are solid-state

sintering, liquid-phase sintering and viscous flow, and they can either work alone or be combined.

The criterion for densification of the powder compact is that the distance between the centres of adjacent particles is reduced. Extensive research has therefore been done to identify the transport mechanisms causing densification or coarsening, as well as postulating rate equations. Understanding these physical mechanisms is crucial to control the properties of the sintered product by experimental variables [30].

The type of sintering determines which mass transport mechanisms are active, and the six possibilities are surface diffusion (1), lattice diffusion from surface (2), evaporation-condensation (3), grain boundary diffusion (4), lattice diffusion from grain boundaries (5), and plastic flow(6) [2]. These mechanisms describe the material paths during sintering and are illustrated in Fig. 2.5. Transport mechanisms 1, 2, and 3 are classified as coarsening as they contribute to inter-particle neck growth without adjacent particle centres approaching each other. Mechanisms 4, 5, and 6 show neck growth with simultaneous densification and are therefore densifying [28]. This means that the knowledge about the rate equations can help encourage the densification by facilitating for mechanism 4, 5 and 6 and restricting mechanisms 1, 2 and 3 [29].

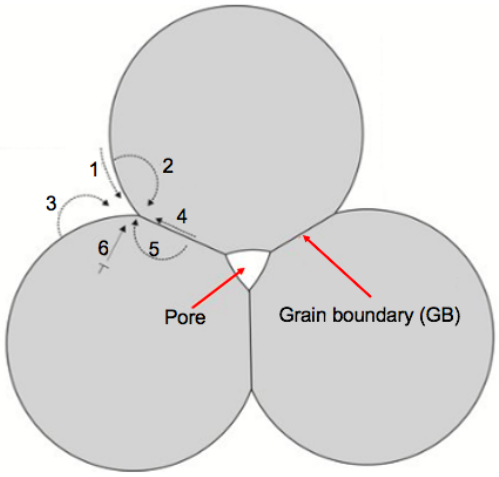

Figure 2.5: An illustration of the six possible transport mechanisms during sintering inspired by Tesfaye [31].

Which sintering type to use depends on the starting material as well as the desired outcome. Viscous flow applies for amorphous materials and is very common for silica-containing ceramics and traditional porcelains [2]. Liquid-phase sintering is often a good option for materials with low self diffusion, as the liquid phase can facilitate for material transport. The material transport is then driven by capillary forces caused by the wetting of the powder by the liquid.

However, liquid-phase sintering requires introduction of additives to the material, and these can be challenging to remove after sintering. SiC is one of the materials with a low self diffusion, meaning that a lot of energy is required for formation

and migration of vacancies and defects [7]. It is therefore common to add sintering aids such as $Y_2O_3-Al_2O_3$ [2]. However, if high purity of the final product is more important, solid-state sintering might be a better option. Eventually it will be a trade-off between purity and density [2]. Independent of method, the aim of sintering is to make products with the desired and reproducible microstructure and properties. By understanding the mechanisms and their driving forces, control of the sintering variables can help reach this goal [32].

2.2.1 Solid-State Sintering

During solid-state sintering the densification is caused by changes in particle shape, and because no additives are required high purity can be obtained. The material transport occurs by diffusion [28]. The rate of diffusion is determined by the temperature and the vacancy concentration in the powder compact, and it is governed by Fick's first law,

$$J_i = -D_i \cdot \frac{c}{RT} \cdot \nabla \mu_i \tag{2.6}$$

where J is the flux, D is the diffusion constant of material i, R is the gas constant, T is the temperature, c is the concentration and μ is the chemical potential [32].

The Role of Curvature

The curvature of the surfaces influences the chemical potential and is therefore important during sintering. An atom at a convex surface has less neighbouring atoms than one at a concave surface, and thus has better mobility. These atoms will therefore diffuse to the concave surface, while vacancies diffuse the opposite direction, as described by Fig. 2.6 [33]. In other words, there is a higher chemical potential at the convex surface, and the surface will become flat after some time. This movement is driven by difference in vapor pressure for gas phase transport and by the defect concentration gradient for diffusion.

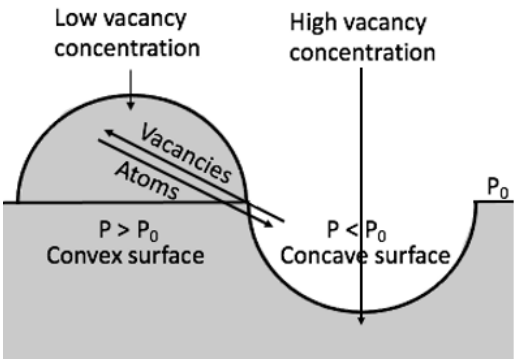

Figure 2.6: A schematic illustration of the atom and vacancy movement driven by the difference in vapor pressure at curved surfaces for gas phase transport, and by a defect concentration gradient at curved surfaces for diffusion.

Further, the curvature will also affect the driving force for pore removal and grain growth. By supplying energy to change the microstructure, e.g. by increasing the temperature, curved surfaces will move towards the centre of the pore or grain. A pore surrounded by convex surfaces will therefore disappear, while a pore surrounded by concave surfaces will grow [32]. This follows from the relationship described by Eq. (2.7), where the dihedral angle, Ψ, is the angle between the interfaces [28].

$$\gamma_{GB} = 2\gamma_{SV} \cdot \cos\left(\frac{\Psi}{2}\right) \tag{2.7}$$

Here, γ_{GB} is the grain boundary energy and γ_{SV} is the solid-vapor interfacial energy. The dihedral angle is defined to be zero for parallel planes, meaning that if a pore only shares flat interfaces with neighbouring grains there is no driving force for pore removal. This is because the energy gained by shrinkage of the pore is equal to the energy needed for extension of the grain boundaries [28]. The same mechanisms also apply for grains, and very large grains will lead to exaggerated grain growth. If the rate of the grain growth exceeds that of vacancy diffusion, porosity will be trapped inside the grain and full densification will not be possible [32]. Because the initial stage of sintering is most dependent on neck geometry, Kang [32] suggests that the discussion of pore stability and curvature is most relevant for the final stage.

Mass Transport Mechanisms

Table 2.2 shows that mass transport by evaporation-condensation is the only mechanism with the difference in vapor pressure above curved surfaces, Δp, as a driving force. The four remaining mechanisms are driven by the difference in vacancy concentration, where some are densifying and some are coarsening. It is therefore important to identify the dependency of the transport rate on different process variables.

Table 2.2: The microscopic driving force of each transport mechanism in solid-state sintering and their classification as densifying or non-densifying [34].

Transport mechanism	**Microscopic driving force**	**Densifying**	**Coarsening**
Evaporation-condensation	Δp		X
Lattice diffusion (from GB)	Δc	X	
Lattice diffusion (from surface)	Δc		X
Grain boundary diffusion	Δc	X	
Surface diffusion	Δc		X

McColm and Clark [28] derived a general relation for the time it takes to reach a specific degree of densification, Δt, using the material flux in response to microscopic driving force. This expression is described by Eq. (2.8) and can be further used to find more specific relations for each of the mass transport mechanisms.

$$\Delta t \propto \frac{V}{J \cdot A \cdot \Omega} \tag{2.8}$$

Here, V is the volume of the transported mass, J is the material flux, A is the surface area the flux passes through and Ω is the atomic volume. The volume, V, is proportional to the particle size, d^3 and the flux increases with increasing particle size. By comparing to Fick's law the following relation is established

$$J \propto \frac{D \cdot \gamma_\pi}{k \cdot T \cdot d^2} \tag{2.9}$$

where J is the flux, D is the diffusion constant, γ_π is the surface energy, k is the Boltzmann's constant and T is the temperature.

Assuming the mechanism is surface diffusion (SD), A from Eq. (2.8) is proportional to δd, where δ is the thickness of the surface layer. This yields the expression presented in Eq. (2.10). Please refer to the work of McColm and Clark for the detailed derivation [28].

$$\Delta t_{SD} = \frac{\beta' \cdot d^4 \cdot k \cdot T}{D_{SD} \cdot \delta \cdot \gamma \cdot \Omega} \propto d^4 \tag{2.10}$$

Similar considerations for grain boundary (GB) diffusion, lattice diffusion from grain boundary (SSL), lattice diffusion from surface (SSL) and evaporation-condensation (EC) result in the following relations between Δt and the grain size.

$$\Delta t_{GB} = \frac{\beta_B \cdot d^4 \cdot k \cdot T}{D_B \cdot \delta_B \cdot \gamma \cdot \Omega} \propto d^4 \tag{2.11}$$

$$\Delta t_{SSL} = \frac{\beta_L \cdot d^3 \cdot k \cdot T}{D_L \cdot \gamma \cdot \Omega} \propto d^3 \tag{2.12}$$

$$\Delta t_{EC} = \frac{\beta'' \cdot 4 \cdot \pi \cdot n^2 \cdot d^2 \cdot R \cdot T}{A_x \cdot A_y \cdot \gamma \cdot \Omega} \propto d^2 \tag{2.13}$$

From the equations introduced above the contribution from each mass transport mechanism can be evaluated as a function of particle size, as illustrated graphically in Fig. 2.7. Because surface diffusion and grain boundary diffusion show the same dependency of the particle size they will have to be separated by other process or material variables. This could be done by introducing dopants, varying the sintering atmosphere or changing the temperature [32][28].

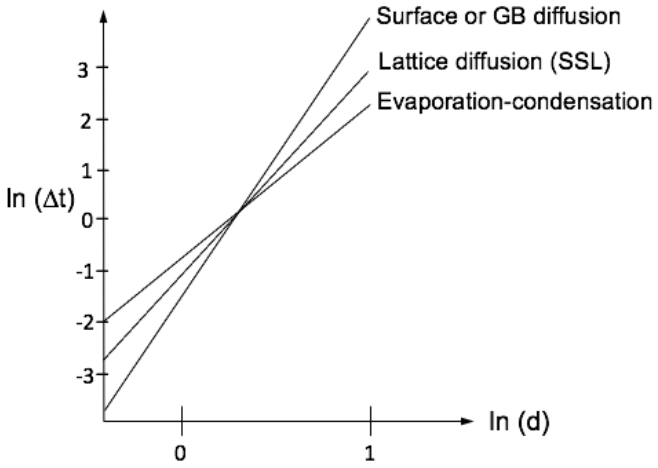

Figure 2.7: A plot relating the particle size to the time necessary to form a given area of neck region for the five sintering mechanisms in solid-state sintering [28].

The Stages of Solid-State Sintering

Solid-state sintering is typically divided into three overlapping stages referred to as the initial, intermediate and final stage. The stages are classified according to the physical changes that occur during sintering. The classic interpretation of the stages as a function of density and sintering time is shown in Fig. 2.8 [32][35].

The initial stage involves rearrangement of particles, yielding many contact points between particles. This makes neck formation, and thus densification, easier, as it is in these contact points the surface energy is highest and mass transport occurs [35]. The surface free energy is reduced by a reduction of surface area and grain boundary area via the formation of grain boundaries [36]. Coarsening mechanisms will dominate in this stage and occurs by evaporation-condensation and surface diffusion. The densification is facilitated by grain boundary diffusion and lattice diffusion, and typically measures only 3 - 5 % [28].

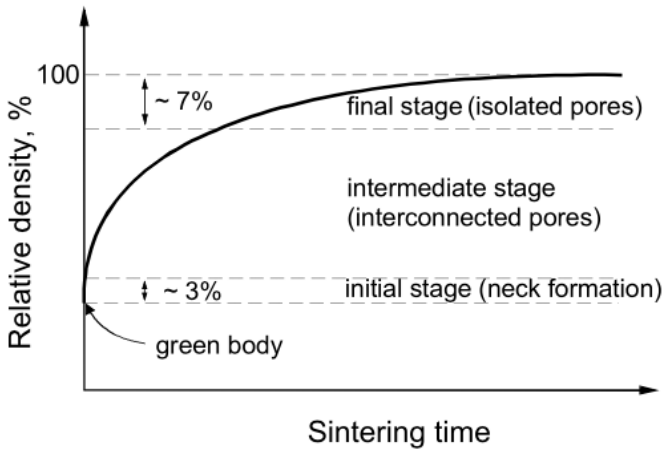

Figure 2.8: A typical densification curve showing the three stages of solid-state sintering as a function of sintering time and relative density [32].

In the intermediate stage most of the densification occurs, meaning that the densifying mass transport mechanisms are dominating. Necks continue forming and the pores create interconnected channels along the edges of grains [32]. Geometrical changes facilitating further neck growth is achieved by movement of grain boundaries such that some grains grow by consuming others [2]. When reaching approximately 93 % relative density the channels of porosity will disconnect and form isolated pores. These pores are too small to hinder grain growth and this is the beginning of the final stage [36][2].

During the final stage of sintering, the remaining porosity is eliminated given a sufficient energy supply. Kang [32] states that for fine powders the densification in this stage is dominated by grain boundary diffusion, while for coarse powders the lattice diffusion dominates. The movement of vacancies and pores is aided by movement of grain boundaries and grain growth. The rate of the grain growth must be controlled to avoid closed porosity inside large grains, making it impossible to reach 100 % density [2].

2.2.2 Spark Plasma Sintering

To enhance the densifying mechanisms and provide additional driving force for sintering, pressure can be applied simultaneously as temperature. Spark plasma sintering (SPS) provides many advantages over other pressure-assisted sintering methods. These advantages include ease of operation, high sintering speed, high reproducibility and reliability. SPS allows for a uniaxial force to be applied while a low voltage pulsed direct current heats the powder sample by resistance heating, as the sample is placed on an adjustable stage between two steel electrodes. Also, the energy is dissipated exactly where needed, namely at the particle contact points. This allows for very high heating and cooling rates, making SPS a time and energy efficient process [37][38].

Graphite is often chosen as material for the die, punches and disks due to its high electrical conductivity, mechanical properties at high temperatures and chemical stability. This is necessary because a low voltage, typically 1-10 V, can produce currents in the range 1-10 kA. The temperature generated by the resistance heating depends on the material and can reach 2500 °C, and in addition a force up to 250 kN may be applied. The continuous temperature measurement is performed by a thermocouple at temperatures below 1000 °C or a pyrometer above 400 °C [38].

Several theories exist on how the particles are bonded, and because so high temperatures are required it is challenging to confirm such physical phenomena [38]. However, Suárez et al. [37] and Hu et al. [39] have described the process believed to take place during spark plasma sintering. The pulsed direct current generates spark plasma, spark impact pressure, Joule heating, and an electrical field diffusion effect [37]. The spark discharge is of special interest because its occurrence at a contact point or gap between particles causes a momentarily high-temperature state. The gas between the particles is then believed to transform to plasma by ionization, allowing for necks to form between the particles. This process is illustrated in Fig. 2.9 [37][2].

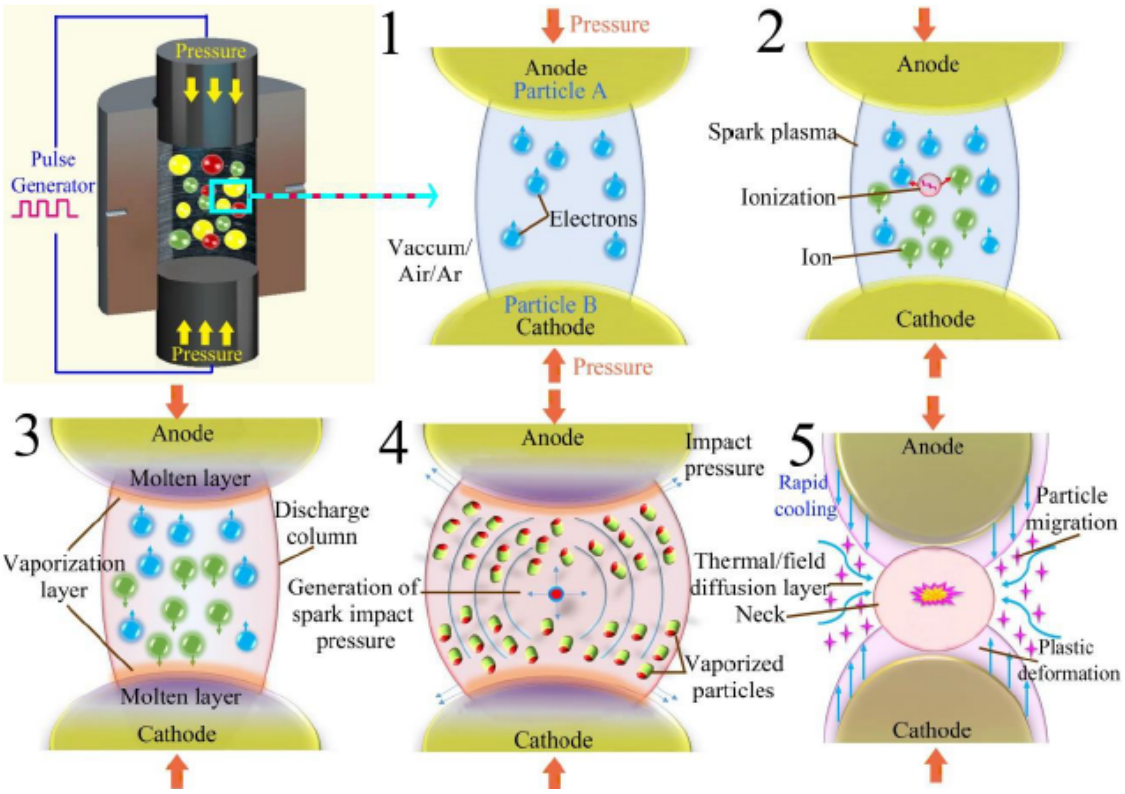

Figure 2.9: The basic mechanism behind the formation of spark plasma and sintered necks [39].

Upon spark plasma sintering of conductive materials the pulse current will flow directly through the powder, punches and die. Even though the intrinsic resistance of the powder is low, the measured resistance is often increased by 4-5 orders of magnitude and local Joule heating is therefore high [39]. Locci et al. [40] suggested that the presence of oxide layers covering the particles was the main reason for the increased resistance, causing local overheating far beyond the measured temperature of the bulk using a thermocouple. Further, Diouf and Molinari [41] concluded that an increase in the particle size dramatically increased the local overheating. Using copper samples they registered a surface temperature of 920 °C at 0.2 µm depth when the SPS was set to 650 °C. As the local overheating involves a thin surface layer the temperature of the bulk is not affected.

The main advantage of applying an external pressure during sintering is that agglomerates fracture, leading to better packing of particles and reduced pore size. Further, the sintering temperature may be reduced and grain growth is limited [39]. Finally, the pressure may also induce phase transformations.

Even though SPS is superior to conventional pressure assisted sintering methods such as hot pressing, there are challenges related to achieving a homogeneous temperature distribution through the specimen. A homogeneous sintering behaviour will result in a higher quality of the sintered product, reflected by e.g. an even distribution of high hardness over the sample surface [37]. In addition to the temperature gradients, Diatta et al. [42] suggested that stress gradients form due to the applied pressure.

The numerical and experimental study on alumina samples (20 mm · 5 mm and 50 mm · 10 mm) indicated that the variations in electric resistance of the die, foils and sample caused differences in the Joule heating of these materials. Thus, a mismatch in the thermal expansion, in addition to the thermal gradients, can contribute to stress gradients when applying the external pressure [39][42].

Experiments performed by Biswas [7] showed that spark plasma sintering of pure SiC with a grain size of 0 - 50 nm resulted in fully dense (> 98 %) samples. Holding the samples for 10 min at 1700 °C and 40 MPa was optimal for retaining the nano grained structure. Increase of temperature and holding time led to grain growth. Another study [43] obtained the same densification for SiC with particles ranging from 30 to 50 nm. Montón et al. [44] performed SPS of as-received SiC (2 µm) by heating to 2200 °C and applying 50 MPa. The conditions were held for 1 min and a relative density of 91 % was obtained for each sample.

2.2.3 Factors Influencing Silicon Carbide Sinterability

How well a powder sinters depends on the material properties and the process parameters. In addition, the particle size, particle size distribution, grain morphology, packing structure and presence of agglomerates can have an effect on the result [2]. Khalil et al. [45] investigated the effect of dispersion in PSD on the sinterability of SiC ceramics using spark plasma sintering. The coefficient of variation, C_v, was used as an alternative dispersion measure as it is a more reliable measure than the variance and standard deviation when the mean particle size is not the same for each powder. C_v is a dimensionless and normalized measure which is highest for the powder with the highest relative dispersion around the mean value, and is described by Eq. (2.14) [45].

$$C_v = \frac{s}{\overline{X}} \tag{2.14}$$

Here, s is the standard deviation and $\overline{X}$ is the mean particle size. Khalil et al.[45] concluded that the ideal SiC powder for sintering had a small mean particle size with a high coefficient of variation. The good sinterability of this powder was attributed to the higher surface area of small particles in combination with a higher degree of packing due to the broad particle size distribution. This is because the high surface area provides a higher driving force for densification, while the high degree of packing provides shorter diffusion distances for atoms [45].

Further, a study by Jensen [46] suggests that the shape of the grains may also affect the microstructure after sintering. If the powder consists of elongated grains it may impact the packing of the powder before and during sintering. This can give preferred orientation in the sample [46]. Another study observed that the presence of polytype 4H in the powder increased the probability of forming elongated grains, and thus preferred orientation, during sintering [47].

Sintering aids such as carbon (C) and boron (B) are often added to enable sintering at lower temperatures and achieve more dense products. Addition of carbon limits the grain growth and facilitates for removal of SiO_2 on the SiC grain surface by Eq. (2.15) above 1520 °C [48] [49]. Literature suggests that boron can substitute for both silicon and carbon in the SiC-matrix, leading to vacancy formation because the atomic radius of B is larger and causes lattice frustration. The vacancies then increase the self-diffusion of SiC [50].

$$SiO_2(s) + 3C(s) \longrightarrow SiC(g) + 2CO(g) \tag{2.15}$$

Elder et al. [49] demonstrated how additions of boron to β-SiC retained the high surface area of the starting powder, and thus preserved the driving force for densification. Without this addition a significant reduction in powder surface area was observed below the sintering temperature of 1800 °C. Addition of B_4C has also resulted in superior mechanical properties compared to that of pure SiC (of equal density) due to the changed bonding characteristics [7].

The presence of sintering aids, impurities and non-stoichiometry can cause a variety of results, and has an impact on the density and polytypes of the sintered samples. The most pronounced effect is observed when impurities of group III or V elements are present, because they act as electron acceptors and donors, respectively. The presence of aluminium stabilizes the polytype 4H [19], while Lundquist [51] showed that phosphorus stabilizes polytype 3C.

2.3 Polytypic Transformation

Although some polytypes (2H, 4H, 6H, 15R, 3C) of SiC are common at ambient conditions, there is still not one single theory which sufficiently describes the origin of all polytypes and transformations between them. The most accepted phase diagram describing the thermodynamic stability regions of these polytypes was suggested by Knippenberg and is presented in Fig. 2.10 [19].

Experimental work [52] [10] [53] has concluded that a polytypic transformation from 3C to 6H occurs at temperatures ranging from 1600 to 2300 °C, depending on the other process and material parameters. Ortiz et al. [54] stated that one contributing factor to this transition was the structural defects of the β-SiC starting powder used in their experimental work. This was because stacking faults and twinned crystals of the 3C structure already possessed the α-SiC configuration, providing many nucleation sites for α-SiC. Further growth is then driven by a reduction of the free energy as the polytypes correspond to the Gibbs energy surface minima [55][53].

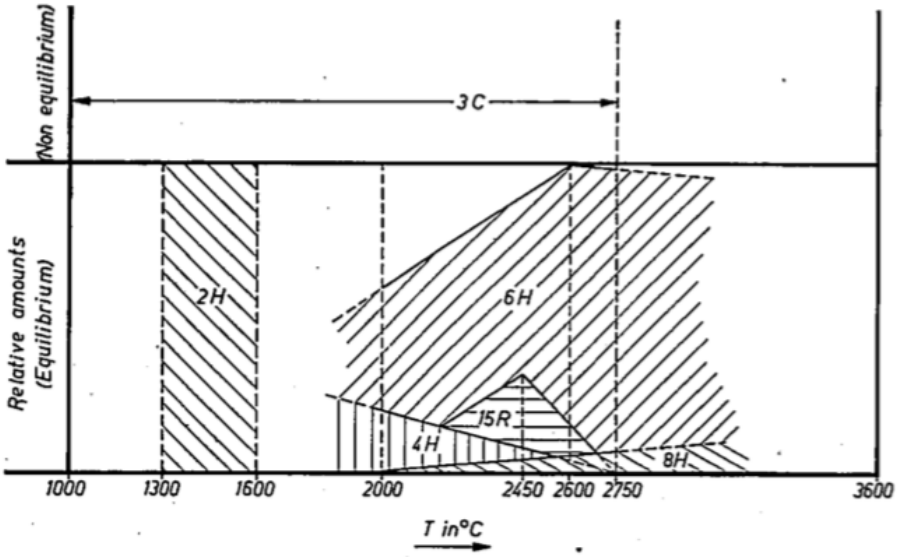

Figure 2.10: The stability diagram of common polytypes of SiC at ambient conditions suggested by Knippenberg [19].

Eom and Kim [56] also concluded that the nucleation sites of α-SiC transformed from β-SiC occurred at existing α-SiC crystals. Hence, the ratio between α- and β-SiC in the powder mixture determined the grain size of the sintered product. If α-SiC is the dominating phase in the powder there are many nucleation sites available and the grain size is retained due to the impingement of growing grains.

A quantum model by Kukushkin [55] has also assessed the mechanism behind the 3C $\rightarrow$ 6H transformation. The work considers a system corresponding to one 6H cell/two 3C cells and uses the nudged elastic beam method to describe the atomic displacements. This means that the most likely path of the transition is used. The main results of their work was that the transition requires both breaking and formation of bonds between homo- and heteroatoms, as can be seen by Fig. 2.11. A lot of energy is therefore necessary for the transition to initiate.

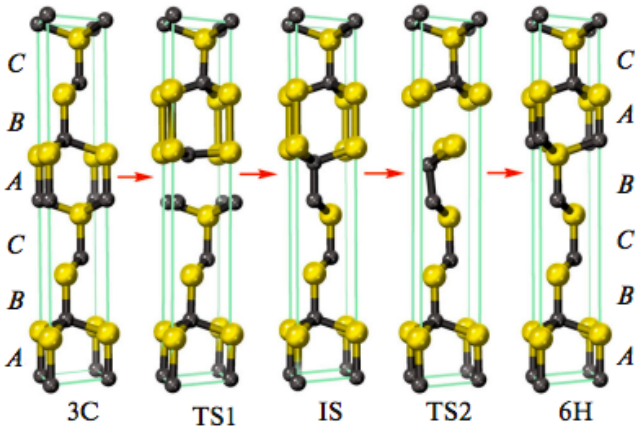

Figure 2.11: Illustration of the mechanism behind the 3C $\rightarrow$ 6H transformation suggested by Kukushkin et al. [55].

Lodeh et al. [52] observed a phase transformation from 3C to 6H at 1600 °C after spark plasma sintering of SiC at 1600 °C and 50 MPa for 10 min. They used their recorded data and an analytical model suggested by Bernard-Granger and Guizard [57] to deduce the stress exponent. This was done by comparing the measured creep rate during SPS with the creep deformation in dense materials. Depending on the value of the stress exponent the observed polytypic transformation was governed by diffusion or dislocation climb or glide.

Independent of which mechanism is proposed to cause the polytypic transformation, there is a general consensus that the temperature is the most important factor. This is because thermal diffusion increases with temperature [19][10]. In addition, a high surface area increases the thermodynamic driving force for nucleation and growth of α-SiC, and thus the transformation rate [58]. Finally, work by Jayakumari [10] suggests that the growth rate of α-SiC increases when performing sintering in vacuum, compared to an Ar or N_2 atmosphere.

2.4 Phase Identification of Silicon Carbide

Reliable phase characterization of SiC is necessary to determine the effects of the presence of different polytypes, but can in some cases be challenging. X-Ray diffraction is traditionally used for phase characterization, and is frequently used on SiC samples. However, for the special case of separating polytype 3C from 6H, XRD alone may be insufficient due to the overlapping diffraction lines. Therefore, other methods such as electron backscatter diffraction (EBSD), Raman spectroscopy and transmission electron microscopy (TEM) are occasionally used in addition to the XRD [59][3][60].

2.4.1 X-Ray Diffraction of Silicon Carbide

An XRD analysis provides a unique diffraction pattern for each material. These patterns of known materials and compounds are stored in a database and can later be used to characterize unknown samples by crystalline phases, preferred orientations, lattice spacing and much more [61]. An example of a diffractogram is presented in Fig. 2.12, where a SiC powder has been analyzed by XRD. This illustrates how no diffraction lines identifying 3C-SiC are isolated, and thus the challenge of separating the polytype from 6H.

Because the intensity is a function of the amount of a specific component in a mixture, XRD is an excellent technique to do a quantitative assessment of the phase composition [62]. According to Ortiz et al. [62] the most reliable method to perform this quantitative assessment is the Rietveld method. However, the method can be limited by factors such as preferred orientation, which can severely impact the intensities of specific peaks. This attribute is typically discovered by high intensities located at 2Θ angles representing symmetrical lattice planes [63].

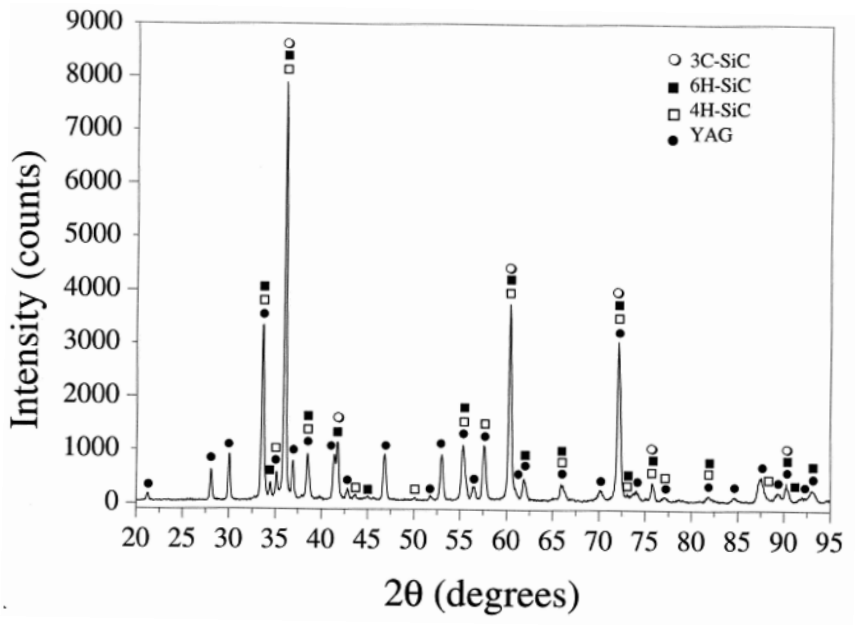

Figure 2.12: The diffractogram of a SiC ceramic with markers identifying the polytypes 3C, 6H and 4H [62].

Fig. 2.13 shows that an experimental diffractogram may have additional diffraction lines, higher background intensity and peak broadening compared to a calculated diffraction pattern. For the case of SiC, Pujar et al. [60] attributed these effects to the stacking faults present in the specimen, as their energy of formation is very low. In addition, sample preparation and contamination from the radiation source may cause deviations from the calculated diffractogram [64].

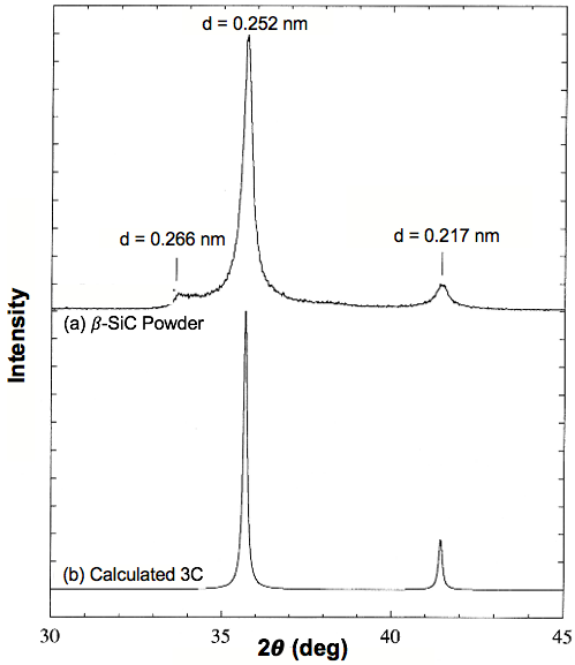

Figure 2.13: The diffraction pattern of the 3C polytype of SiC obtained experimentally (a) and by calculations (b) [60].

2.4.2 Raman Spectroscopy of Silicon Carbide

Phase characterization by Raman spectroscopy is particularly useful for materials with strong molecular bonds, such as SiC [65][66]. Several studies [67][68] have used Raman scattering to identify polytypes in SiC ceramics. Nakashima et al. [3] confirmed that this is possible for several polytypes, including 3C and 6H. Raman frequencies for the folded modes of the most common polytypes were obtained and longitudinal optical (LO) bands of 3C and 6H were observed at $972\,\mathrm{cm}^{-1}$ and $965\,\mathrm{cm}^{-1}$, respectively.

The 3C $\rightarrow$ 6H transformation in SiC has been investigated by Raman spectroscopy of physical vapor transport (PVT) and chemical vapor deposition (CVD) grown 3C crystals. The Raman spectra confirmed the 3C $\rightarrow$ 6H transformation for temperatures above 1800 °C. From 1700 °C a partial conversion was observed. The same results were obtained for both growth methods, and the polytypic transformation was therefore attributed to the heat treatment, not the growth process [68].

If the investigated grains contain stacking disorder, the Raman bands will exhibit broadening. The broad bands are often located at frequencies related to modes of common polytypes, and the broadening implies the presence of many short-range stacking structures of the polytype. Such spectral profiles are often observed for crystals produced by the Acheson process and can be seen in Fig. 2.14 [3].

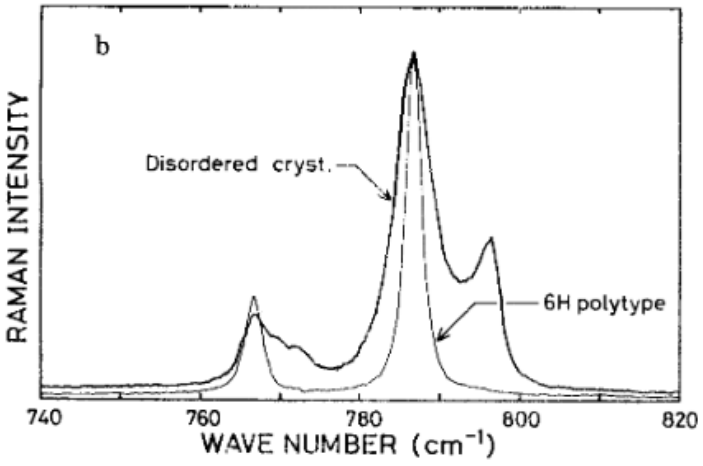

Figure 2.14: Raman spectra of a SiC crystal with stacking disorder exhibiting broadening in the folded transverse optical (FTO) modes [3].

2.5 Mechanical Properties and Testing

Whether a material is appropriate for structural applications or not is determined by its mechanical properties, such as elasticity, hardness, strength and fracture toughness. To investigate these properties there are several methods that can be used depending on sample material, geometry and porosity. The brittle nature of ceramics, including SiC, makes it more challenging to perform certain tests, as will be discussed in the following sections.

2.5.1 Strength

The different types of strength include theoretical strength, tensile strength, compressive strength and biaxial strength, amongst others [2]. The theoretical strength, σ_t, of a material is defined as the tensile stress needed to break the atomic bonds and thereby pull the structure apart (given a tensile test). This can be expressed by the following equation

$$\sigma_t = (\frac{E\gamma}{a_0})^{1/2} \tag{2.16}$$

where E is the elastic modulus, γ is the fracture surface energy and a_0 is the interatomic spacing [69]. This is the maximum strength of the material, but it has never been achieved in experimental work due to the inevitable presence of fabrication flaws and structural defects in a ceramic [2]. These flaws can lead to a measured strength of only 1/100 of the estimated theoretical strength according to experiments by Stokes [70].

The type of flaws and defects that contribute to a reduction of the strength includes pores and cracks, as well as contamination by other elements. The pore geometry is often irregular in ceramic materials, and both size and shape are important factors when determining the strength [71]. Further, the position of the pore is also critical. An internal pore close to the surface of a sample can lead to breakage of the material above this point, leading to a critical flaw due to the concentration of stress. Similarly, if many pores are clustered together they will weaken the sample and crack initiation is likely to occur in this point [2].

Existing relationships between strength and porosity can be separated into two main categories, being power-law functions and exponential functions. Knudsen [72] compared these two categories and concluded that within a limited range of porosity they provided almost equivalent results. However, the exponential relationship proved to be more reliable in a broader range [73]. This exponential relationship was derived by Ryshkewitch and Duckworth [74], who stated that the strength of a sample varied with open porosity according to Eq. (2.17).

$$\sigma_{true} = \sigma \cdot e^{-Bp} \tag{2.17}$$

Here, σ is the strength at 0 % porosity, B is an empirical constant and p is the porosity expressed as a fraction. It should be mentioned that this expression has its limitations as it predicts a bearing capacity even though the porosity is beyond 100 % [73]. The empirical constant B is the slope of the $\log \sigma$ vs P curve and was estimated to be 7, independent of the material and pore size by Ryshkewitch and Duckworth [74].

The main advantage of biaxial testing methods is that they produce a biaxial stress field, meaning that the specimen is exposed to tensile and shear stresses simultaneously. This is achieved by applying a normal force and a tangential force at the same time and can be performed using methods such as ball-on-ring (BOR), ring-on-ring (ROR) and piston-on-3 ball (POB).

The BOR, ROR and POB are all considered to be more reliable than e.g. three-point bending test, as they produce similar stress distributions independent of geometry and avoid the problem of tensile loaded edges [75]. To determine which of these methods is the preferred choice for specific measurements a summary of the advantages and disadvantages of the different set-ups is presented in Table 2.3.

Table 2.3: A summary of the advantages and disadvantages of some different set-ups for biaxial strength measurements inspired by Morrell [76] and de With [77].

Method	**Advantages**	**Disadvantages**
Ball-on-ring	Symmetrical Self-aligning Minimum friction during loading	Requires flat specimen Limited volume under stress Ball/specimen contact area dependent on load
Ring-on-ring	Symmetrical Large region of constant stress	Requires flat specimen Friction effects are hard to control 20% increase in stress under the loading ring
Piston-on-3 ball	Copes with non-flat specimen	Limited volume under stress Possible misalignment of specimen relative to piston end Friction effects unknown nonuniform stress under piston

2.5.2 Ball-on-Ring Mechanical Testing

During the ball-on-ring testing, a flat specimen is supported on a ring holder and loaded by a coaxially located ball, as can be seen in Fig. 2.15. The load generates an equibiaxial stress field which is most intense in the centre of the sample and decreases outwards [76][77]. Fig. 2.15 illustrates how the stress has a compressive nature on the ball-side surface and tensile on the ring-side surface. The magnitude of the tensile and compressive stresses are the same, $|\sigma_{max}|(r)$, while the neutral plane remains stress free.

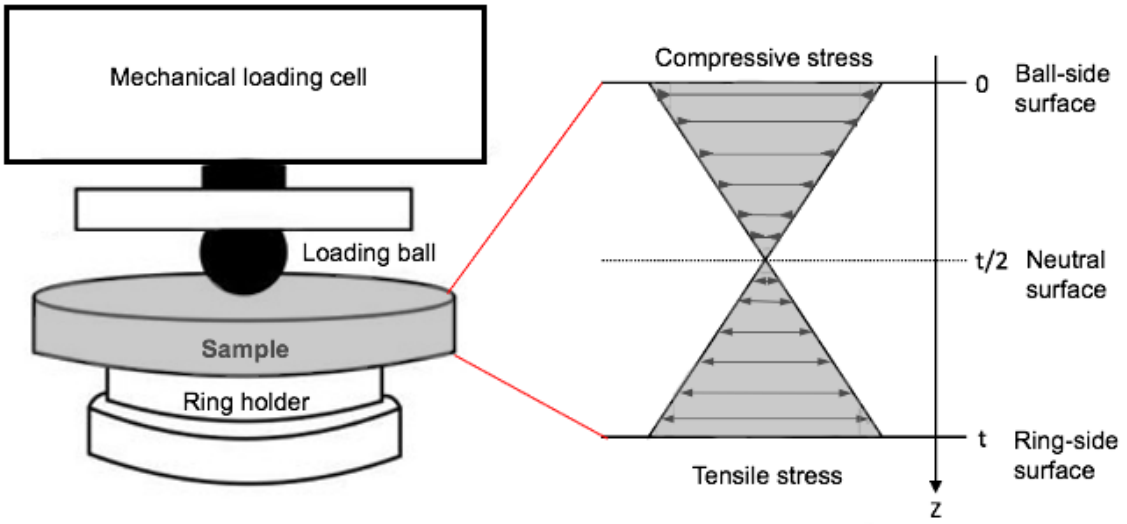

Figure 2.15: The set-up during biaxial strength measurements by ball-on-ring testing and an illustration showing the stress distribution in the cross-section of a sample during the test. The arrows indicate the magnitude of the stress [78].

To find this stress based on the ball-on-ring method a closed-form solution developed by Kirstein and Woolley [79] is applied. Their solution is adapted from Bassali's [80] solution for transverse flexure of thin perforated elastic plates supported at several points and is independent of the number of supporting points [77]. The maximum stress (tangential and radial) at the center of the specimen is given by

$$\sigma_{max}(r) = \frac{3P(1+\nu)}{4\pi t^2}\left[1 + 2\ln\left(\frac{a}{b}\right) + \frac{1-\nu}{1+\nu}\left(1 - \frac{b^2}{2a^2}\right)\frac{a^2}{R^2}\right] \tag{2.18}$$

where P is the applied load, ν is Poisson's ratio, t is the specimen thickness, a is the radius of the supporting ring, b is the area of uniform constant stress and R is the radius of the specimen [79][81][77].

The one major disadvantage of the BOR test is the dependency of the contact area on the load. This has led to disagreement on how to estimate the area of uniform constant stress, b. Shetty et al. [82] are amongst those who have come up with equations to determine this area [77]. They applied the solution by Kirstein and Woolley to the BOR method and performed a study on Al_2O_3 disks where data obtained by biaxial testing was compared to data from three- and four-point bending tests. Weibull analysis based on finite element analyses was applied on the data and Hertz's elastic contact theory was used to estimate the contact area, b [82]. The contact radius is then defined by Eq. (2.19)

$$z = \left[\frac{3Pr}{4}\left(\frac{1-\nu_1^2}{E_1} + \frac{1-\nu_2^2}{E_2}\right)\right]^{1/3} \tag{2.19}$$

where subscript 1 denotes the specimen and subscript 2 the loading ball, r is the radius of the loading ball and E is the elastic modulus of the two materials [83][81].

To take into account the small loading area, Eq. (2.19) is combined with the relationship between z, t and b_{eq} inspired by Westergaard [84]. This solution considers the deformation of the specimen as a result of the vertical stresses and is presented in Eq. (2.20) [81].

$$b_{eq} = \begin{cases} \sqrt{1.6z^2 + t^2} - 0.675t, & \text{for z} < 1.724\text{t} \\ z, & \text{for z} > 1.724\text{t} \end{cases} \tag{2.20}$$

Combining Eq. (2.20) and Eq. (2.18), the modified equation for the maximum stress experienced by the specimen, presented in Eq. (2.21), is obtained. Chae et al. [81] showed that inclusion of the equivalent radius attributed to Westergaard was critical to achieve good agreement between numerical and analytical solutions.

$$\sigma_{max} = \frac{3P(1+\nu)}{4\pi t^2}\left[1 + 2\ln\left(\frac{a}{b_{eq}}\right) + \frac{1-\nu}{1+\nu}\left(1 - \frac{b_{eq}^2}{2a^2}\right)\frac{a^2}{R^2}\right] \tag{2.21}$$

This model makes the assumption that the fracture will occur within the area below the loading ball, where the stress is highest. However, as flaws are randomly distributed in ceramics one can not exclude the possibility of a failure in region II or III in Fig. 2.16. Therefore, Frandsen [85] applied Weibull statistics to determine the probability of failure depending on the stress distribution of the entire specimen. The analytical solution was in later work verified by several finite element models [86][87].

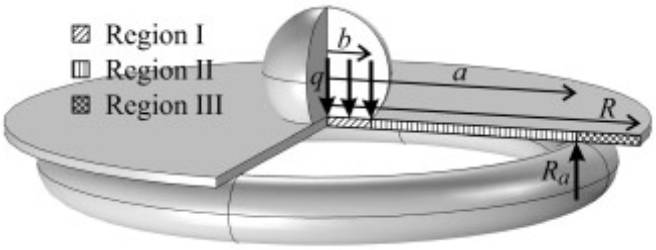

Figure 2.16: A schematic illustration of the three zones through a disk during the BOR-test. Regions I, II and III having a radius of b, a and R, respectively [85].

2.5.3 Hardness

Hardness is defined as "the resistance with which a body counters the penetration of another (little deformable) body" [88]. To test this property, the specimen is subjected to a stress by applying a force on a rigid indenter made of a harder material.

The resistance to deformation is thus defined by

$$H = \frac{F}{A} \tag{2.22}$$

where H is the hardness, F is the force applied during testing and A is the area of the indentation mark. The resulting hardness of the specimen is closely linked to its structure, environment, composition, microstructure and porosity. A material with strong and continuous bonding, such as SiC, will exhibit high hardness [88].

To measure the hardness experimentally, methods such as Brinell, Rockwell, Vickers and Knoop are used. Vickers is a microindentation testing method, and is commonly performed on ceramics [89]. A small diamond indenter with pyramidal geometry is used to make impressions on the specimen surface. Using the Vickers technique the hardness is calculated by the following equation

$$HV = \alpha \frac{F}{d^2} \tag{2.23}$$

where α is a constant dependent on the indenter shape, F is the applied force in kgf and d is the average of the horizontal and vertical length of the diagonals of each indent in mm. For the Vickers profile the value of α is 1.8544. [90]

The hardness of a material is dependent on the porosity. Milman et al. [91] showed that an increase in the porosity of sintered SiC from 5 to 16 % led to a decrease in the Vickers hardness from 20 to 10 GPa. This was because the amount of pores available to collapse under the load had increased [92]. When measuring the hardness of a porous material it is therefore important to use a high load, because the indenter mark is larger and thus the ensemble of porosity below this mark is more representative [91][88]. Ryshkevitch [91] proposed the following relationship between HV and porosity (similar to that of strength and porosity in Eq. (2.17)).

$$HV = HV_0 \cdot e^{-Bp} \tag{2.24}$$

Here, HV_0 is the hardness of the material with no porosity, B is an experimental constant and p is the porosity. This agreed well with the experimental results obtained in the study by Milman et al. [91].

Hardness increases with decreasing grain size because the reduced grain size leads to more grain boundaries where dislocations can pile up. The dislocations will lead to a stress concentration and thus a larger force is necessary to cause material flow in the specimen [89]. The study by Rice et al. [93] was in agreement with this relationship, but the data was too limited to conclude for the specific case of SiC. Other studies [94][95] report that for very fine or very coarse powders of SiC this relation does not hold.

Karandikar et al. [94] did not observe a clear trend relating grain size to hardness for sintered SiC with average grain sizes in the range 2-10 µm. They suggested that variation in local microstructural features such as porosity, grain elongation and grain orientation could be the cause of this because of the small indent.

2.5.4 Fracture Toughness

The point of fracture for a material can be considered in terms of the stress concentration at the tip of a crack. The stress concentration is commonly denoted by a stress intensity factor, K_I, for loads perpendicular to the crack. When the applied load leads to unstable crack propagation and thus fracture, the stress intensity, K_I, reaches a critical point, K_{Ic}. This is known as a materials fracture toughness [2][96].

To calculate the fracture toughness based on the Vickers micro-indentation technique, many have tried to derive an equation. Some of the most frequently used equations were derived by Anstis et al. [97] and Niihara and Miyoshi [96]. A study [98] on spark plasma sintered SiC used the equation by Anstis presented in Eq. (2.25)

$$K_{IC} = 0.016\left(\frac{E}{HV}\right)^{1/2}\left(\frac{P}{c^{3/2}}\right) \tag{2.25}$$

where E is Young's modulus, H is the Vickers hardness calculated by Eq. (2.23), P is the applied load and c is the average crack length.

The fracture toughness of ceramic materials can be enhanced by altering their microstructure such that they can either withstand or delocalize the stress at the crack tip. This can be achieved by mechanisms such as crack shielding or bridging [2]. Some ceramics can also be self-reinforced due to phase transformations during sintering. This behaviour has been observed upon sintering of SiC, where the plate-like structure of α-SiC formed by β-grains increase the fracture toughness through crack deflection [4].

2.6 Failure Analysis

The fracture of a ceramic is a result of the complex interdependence of the conditions, local environment, sample geometry, applied stress and material properties [99]. Therefore, it is extremely important to perform failure analyses to isolate the origin of failure. This will help determine why the failure occurs and which measures should be considered to meet the required criteria of the specimen. This can be efficiently done by fractography, which is "the examination of the fractured or damaged hardware in an effort to reconstruct the sequence and cause of fracture" [2].

The process often begins with a visual inspection of the reconstructed fractured ceramic. In some cases this alone can give an indication of where the fracture originated from the pattern formed by the cracks. Further inspection of this area, typically by scanning electron microscopy, will then help identify why the fracture occurred. This can be high stress, cluster of pores, an inclusion in the material, material degradation etc [2][99].

At fracture initiation the velocity is zero, but the crack quickly accelerates through the material. As the crack propagates it interacts with the stress field and microstructure, and this often leaves distinct features on the fracture surface. [99] The region closest to the origin is referred to as the mirror zone and is characterized by a smooth and flat appearance. Further out, as the crack slightly deviates from its plane, faint radial ridges are formed and create the region called the mist. As the ridges become larger they are referred to as hackle [2]. These zones are illustrated in Fig. 2.17.

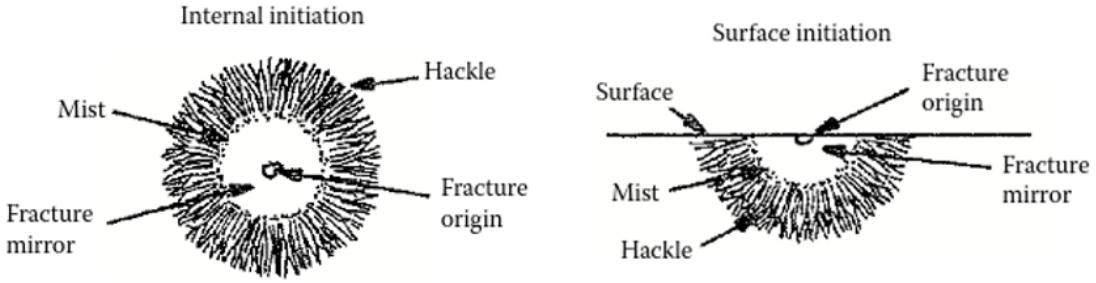

Figure 2.17: The typical features observed around the fracture origin of a ceramic specimen and their location depending on where the fracture is initiated [2].

However, these zones are not always clearly visible. If the ceramic specimen has a very coarse or bimodal microstructure, the features presented in Fig. 2.17 may not be distinct enough for measurements. One of the most powerful tools to proceed with the fracture analyses in these cases is to look at reference images and other case studies [99].

3 Methods and Experimental Details

3.1 Powders and Apparatus

The powders presented in Table 3.1 were provided by Washington Mills, and were produced by the Acheson process. The equipment listed in Table 3.2 were used to prepare and analyse the as-received powders and the sintered samples.

Table 3.1: Overview of the as-received powders, their trade names and their impurity content measured by Washington Mills. The P indicates that it is a powder and the main polytype is the α (6H, 4H, 15R) or β (3C). The numbers (250, 60) are based on the trade names used by Washington Mills.

Powder	**"Trade name"**	**Free C** [%]	**Free Si** [%]	**SiO_2** [%]	**Metals** [ppm]	**Comment**
P-α250	250u	0.02	0.26	0.29	<5	Coarse powder
P-α60	-	0.02	0.26	0.29	<5	Coarse powder
P-α	5u	0.2	0.25	0.4	<10	Sintering aid
P-β	β-SiC	0.07	0.02	0.65	<10	Sintering aid

Table 3.2: Description of which equipment were used for each step of the experimental procedures.

Equipment/Method	**Model**	**Procedure**
Roller Mill	Technotest	Mixing powders
Rotary evaporator	BUCHI R-210	Drying suspensions
X-ray diffraction	Bruker D8 Advance DaVinci	Phase analyses
Raman spectrometer	WITec Alpha 300R	Phase analyses
Laser diffraction	HORIBA Partica LA-960	Measure particle size distribution
Electron microscope	Hitachi S-3400N	Study microstructure
Sintering	Fuji - Dr. Sinter SPS 825	Sinter with pressure
Polishing	Peenmatic 750 S	Remove graphite foil
Vacuum desiccator		Determine porosity
Polishing machine	Struers Tegramin-30	Polish samples
Nitrogen adsorption	Micromeritics FlowPrep 060	Degassing powders
Nitrogen adsorption	Micromeritics 3Flex 3500	Measure specific surface area
Ball-on-ring	Instron 5543	Measure biaxial strength
Vickers indentation	Innovatest Nova 360	Measure hardness

3.2 Procedure

A flow chart describing the experimental activities is presented in Figure 3.1.

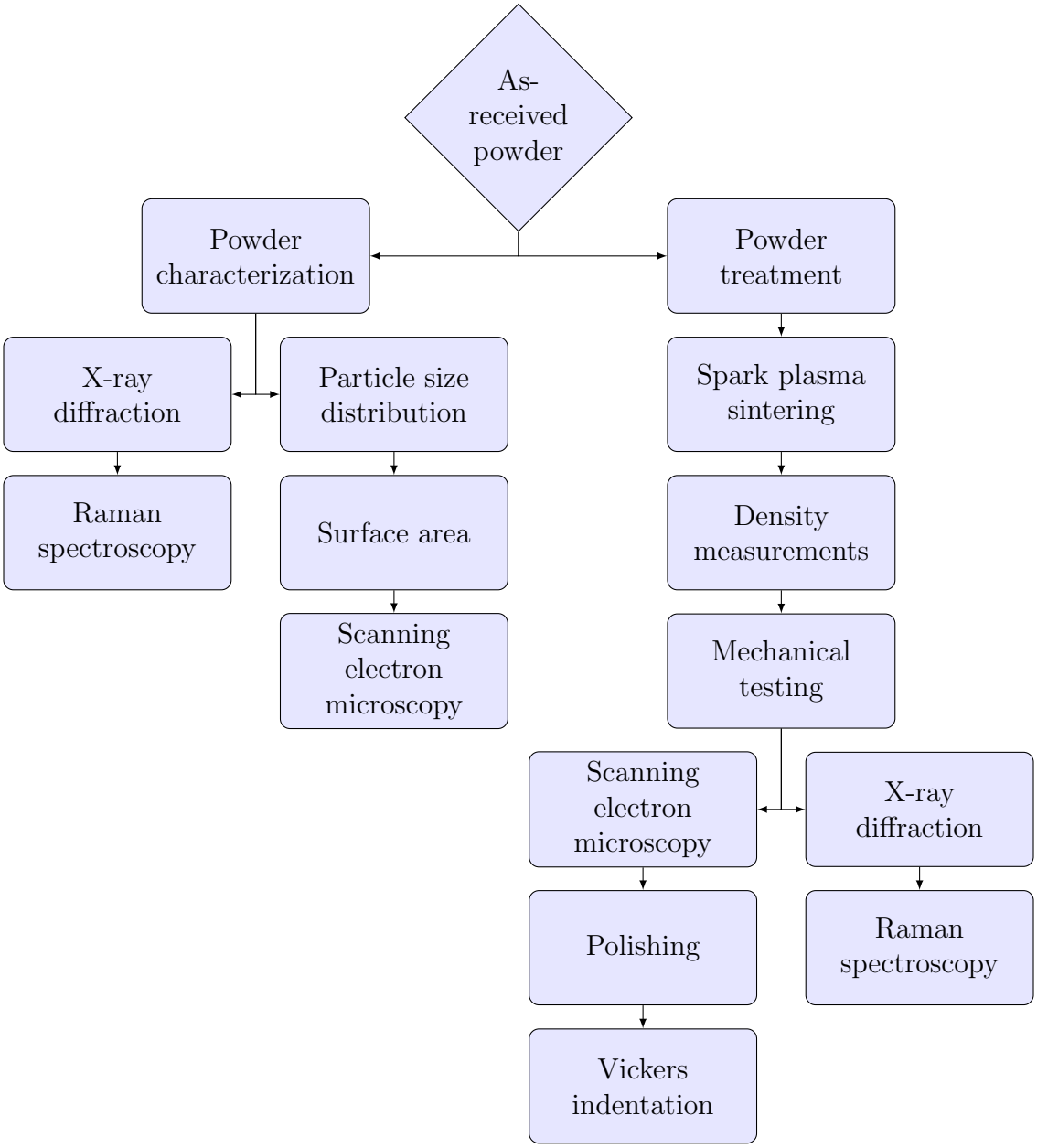

Figure 3.1: Flow chart describing the flow of the main experimental activities.

3.3 Powder Treatment

Powder mixtures P-α60/α and P-α60/β were made by mixing P-α60 (27 g) with P-α (3 g) and P-β (3 g), respectively, by ball milling for 4 h. The powders were added to two separate polyvinyl chloride (PVC) flasks (250 mL) together with 120 yttrium stabilized ZrO_2 (YSZ) balls and 100 % ethanol (50 mL).

After mixing, the YSZ-balls were removed by using a low-mesh sieve when pouring the suspension into a beaker flask. Ethanol was evaporated at 60 °C and 175 mbar using a rotary evaporator. The dried powders were stored in glass jars with lids for further use, and their notation and composition are presented in Table 3.3.

Table 3.3: Composition of the powder mixtures.

SiC-powder	**P-α60 [wt%]**	**P-α [wt%]**	**P-β [wt%]**
P-α60/α	90	10	0
P-α60/β	90	0	10

3.4 Powder Characterization

The as-received powders were analyzed according to their particle size distribution (PSD) by laser diffraction, using the HORIBA Partica LA-960. SiC powder (0.5 g $\pm$ 0.1 g) was added directly to the distilled water circulating through the system and the PSD was measured three times for each powder. The system was rinsed with distilled water between each measurement.

The specific surface areas of the fine SiC-powders, P-α and P-β, were measured by N_2 absorption. The powders were degassed for 12 h using the Degas Smartprep for 3Flex. The degassed powders were weighed before mounting them to the 3Flex 3500. The MicroActive software was used to set the program described in Table 3.4 and measure the N_2 isotherms. Surface area was measured using the 5-point BET method.

Table 3.4: The temperature program used for N_2 absorption measurements of the SiC-powders.

Step	**Temperature [°C]**	**Rate [°C/min]**	**Time[min]**
1	30	10	10
2	90	10	60
3	250	10	720
4	25	10	60

The microstructure and morphology of the powders were investigated by scanning electron microscopy (SEM) at 15 kV using a secondary electron detector on a Hitachi S3400-N. The powders were mixed in ethanol to disperse any agglomerates from the drying process and a droplet of the suspension was placed on the stubs using a pipette. For better adhesion and conductivity carbon tape was used on the stubs.

The phase composition of the as-received powders and the powder mixtures was analysed by X-Ray diffraction (XRD) using the DaVinci1 with a Bragg-Brentano geometry and CuK_α radiation (1.5406 Å). The powders were analysed in the 2Θ-range 30° - 80° with a variable divergence slit (6 mm) and a step size of 0.010°/step.

A qualitative analysis of the as-received powder composition was performed by Raman spectroscopy using a backscattering geometry and white-light illumination (532 nm) from a monochromatic diode laser. The powders were placed between two glass plates under the laser and observed at room temperature. To reduce the fluorescence the laser power was reduced to 20 mW and the measurements were made on flat surfaces which appeared normal to the laser. Ten measurements were performed on each powder, where each measurement consisted of ten accumulations using a 10 s integration time.

3.4.1 Spark Plasma Sintering

An illustration of the set-up used during the spark plasma sintering is presented in Fig. 3.2. A two punch graphite die (28 mm diameter) was lined with graphite foils on the inside before inserting one graphite punch and adding SiC-powder (5.0 g). The die was carefully shaken to achieve an even distribution of powder before placing the punch on top. A uniaxial press was used to stabilize and align the powder with the pyrometer measurement hole by applying a pressure of 5 MPa.

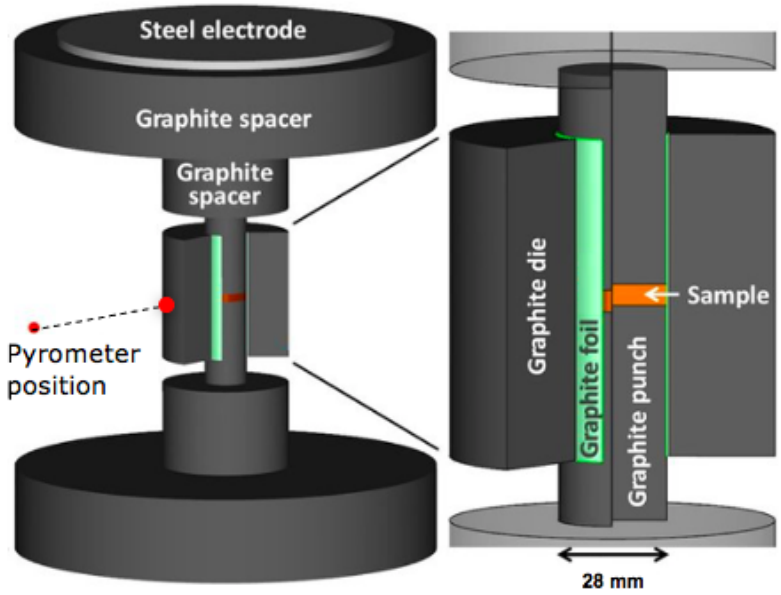

Figure 3.2: A schematic of the set-up used during spark plasma sintering. [100]

The die was covered by a layer of graphite felt (20 mm thickness) before placed symmetrically between the electrodes in the vacuum chamber of the Dr. Sinter SPS 825. Additional graphite disks were used to adjust the height of the die so that it was aligned with the window to the external pyrometer. An additional layer of graphite felt was added around the graphite die to reduce heat loss due to radiation, and steel covers were placed around the sample without blocking the pyrometer view. The chamber was evacuated to a pressure of 25 Pa and the sintering program displayed in Fig. 3.3 was used. The thermal cycle applied corresponds to a heating rate of 100 °C min^{-1} to the maximum temperature of 1900 °C, a dwell time of 5 min and cooling rate of 100 °C min^{-1}.

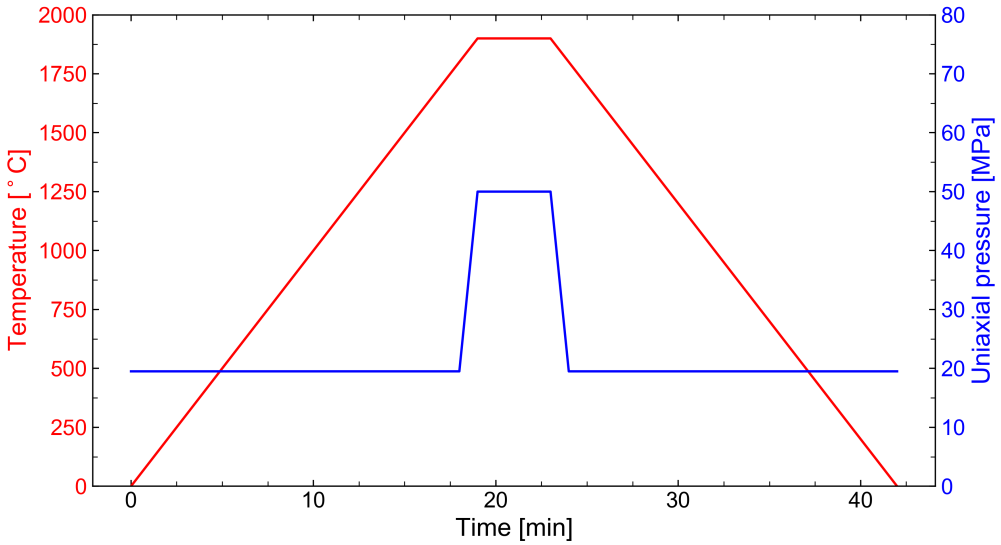

Figure 3.3: The temperature and pressure program for spark plasma sintering with heating and cooling rates of 100 °C min^{-1} and 5 min holding time at 1900 °C and 50 MPa.

Table 3.5: The name, composition and sintering parameters of the samples.

Sample	**P-α60** [wt%]	**P-α** [wt%]	**P-β** [wt%]	**Temperature** [°C]	**Pressure** [MPa]	**Time** [min]
S-α60-1	100	0	0	1900	50	5
S-α60-2	100	0	0	1900	50	5
S-α60-3	100	0	0	1900	50	5
S-α60/α-1	90	10	0	1900	50	5
S-α60/α-2	90	10	0	1900	50	5
S-α60/α-3	90	10	0	1900	50	5
S-α60/β-1	90	0	10	1900	50	5
S-α60/β-2	90	0	10	1900	50	5
S-α60/β-3	90	0	10	1900	50	5
S-β	0	0	100	1900	50	20

A uniaxial press was used to push the sample out of the graphite die after sintering and the graphite foil was removed by microblasting. The sample and sintering characteristics are presented in Table 3.5. One sample of 100 % P-β was sintered for 20 min to investigate the phase composition.

3.4.2 Density Measurements

The density of the samples was measured from geometrical data using a caliper. The bulk density and porosity of each sample was also measured by Archimedes method. The sintered samples were placed in a beaker inside a vacuum desiccator. The desiccator was evacuated to 20 mbar and held for 20 min before introducing isopropanol through an inlet tube. The samples were immersed in isopropanol for 30 min while maintaining the vacuum. Air was carefully introduced through the inlet tube and the samples were kept in the isopropanol at ambient pressure for another 30 min.

The mass of the immersed sample(s) in isopropanol was recorded. Each sample was weighed while immersed in isopropanol. The excess isopropanol on the surface of a sample was removed using a damp tissue and the mass was recorded. The collected data was used to calculate the bulk density, as well as the open, closed and total porosity, as shown in Appendix C.

3.4.3 Phase Composition

Sintered samples were analyzed by XRD to determine phase composition. The samples were analysed in the 2Θ-range 30°- 80°using a variable divergence slit (6 mm), CuK_α radiation (1.5406 Å) and a step size of 0.010°/step. Version 6 of the EVA software was used to identify the phases by comparing to known diffractograms from the International Centre of Diffraction Data (ICDD).

A quantitative assessment was performed by Rietveld refinement using the TOPAS (Total pattern analysis solution; Bruker AXS, Version 5) software on each XRD data file individually. The emission profile, background and instrument settings were loaded and the structure entries of the considered polytypes (3C, 4H, 6H and 15R) were imported. The Rietveld refinement was performed and the calculated diffraction pattern was compared to the measured pattern.

The polytypes of the sintered samples were identified by Raman spectroscopy using backscattering geometry and white-light illumination (532 nm) on the WITec Alpha 300R. Analyses were performed on polished samples (see Table 3.6) as their flat surface was ideal to achieve high intensities. The fluorescence was reduced by using a laser power of 20 mW. Each sample was measured ten times, where each measurement had an integration time of 10 s and provided a mean of ten accumulations.

3.4.4 Mechanical Strength

The biaxial strength of the sintered samples was measured by the ball-on-ring (BOR) test using Instron 5543. The samples were placed on a ring holder of steel (radius 10 mm). A steel loading ball (radius 3 mm) was then centered on top of the sample using a steel plate with a small cavity in the centre. The set-up can be seen in configuration B in **??**. This set-up was assembled below the loading cell where the height was adjusted manually until the ball was stabilized on top of the sample.

The Bluehill software was used to set the loading rate of 1 mm/min, sample dimensions and compression mode. The chosen program was then initiated and the extension and load was measured every 20 ms. The loading was continued until fracture. Young's modulus was estimated by localizing the the linear region of the stress-strain curve of each sample and using the measured data to calculate the slope by

$$E = \frac{\sigma_2 - \sigma_1}{\epsilon_2 - \epsilon_1} \tag{3.1}$$

where σ is the measured stress and ϵ is the measured strain at points 1 and 2 [2].

3.4.5 Microstructure

Each fractured sample was reconstructed to localize the fracture origin and the fracture surface was investigated by scanning electron microscopy. Attention was payed to the lower surface during the BOR-test, as the sample is more likely to fracture from tensile stress than compressive stress. An accelerating voltage of 15 kV was applied together with a probe current of 40 nA. A secondary electron detector was used to obtain images at different working distances and magnifications.

3.4.6 Hardness

The fractured samples were cast in epoxy which hardened overnight. Polishing was performed using the Struers Tegramin-30 with diamond disks and suspension down to a 1 µm finish. To achieve this finish, the samples were placed symmetrically to balance the sample holder and polished as described by Table 3.6. The samples and sample holder were cleaned using an ultrasonic bath with distilled water.

Table 3.6: The types of diamond disks and suspensions used during each step of the polishing, as well as the applied load, time and speed.

Step	**Disk**	**Suspension**	**Load [N]**	**Time [min]**	**Speed [rpm]**
1	MD-Piano	Water	30	5	150
2	MD-Allegro 9µm	DiaPro All/Lar 9	20	5	150
3	MD-Dac 3µm	DiaPro Dac 3	20	3	150
4	MD-Nap 1µm	DiaPro Nap-B1	20	4	150

Hardness measurements were performed by Vickers micro-indentation on polished samples using the Innovatest Nova 360. A 2 kg load was applied for 10 sec to make ten indents on each sample. The hardness was then calculated from the following equation

$$HV = 1.8544\frac{F}{d^2} \tag{3.2}$$

where F is the applied load [kgf] and d is the average of the horizontal and vertical length of the diagonals of each indent [µm]. To avoid interference from edge defects the indents were made at least 3 mm from the edges. Further, the space between the indents was a minimum of four times the size of the indent to make sure they did not affect each other. [101]

4 Results

4.1 Powder Characterization

The particle size distributions of the as-received powders are presented in Fig. 4.1. The distributions obtained by laser diffraction are relatively narrow considering the mean particle sizes and indicate nonagglomerated powders. The coefficient of variation presented in Table 4.1 is highest for P-α and the calculations are described in Appendix A. The surface area and estimated particle size of the two sintering aids measured by nitrogen absorption and assuming spherical particles are presented in Table 4.2.

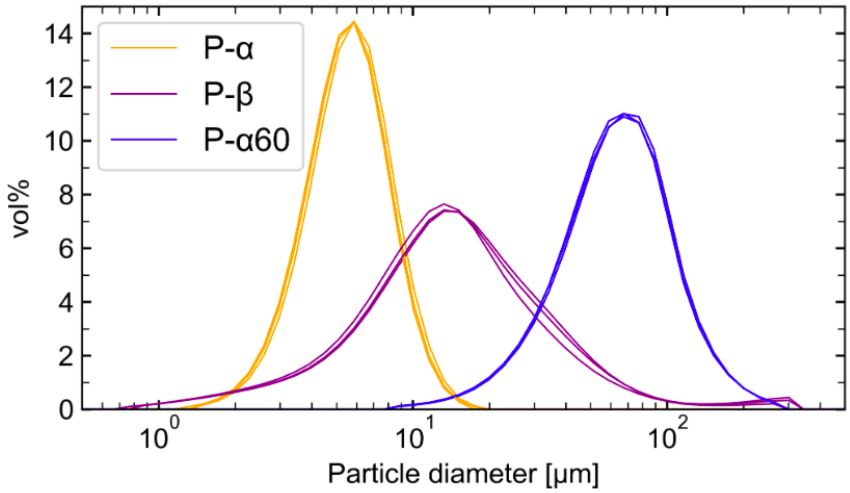

Figure 4.1: Particle size distributions of the as-received powders measured by laser diffraction. Each powder was measured three times.

Table 4.1: The mean particle size and the coefficient of variation [45] of the as-received powders obtained by laser diffraction and calculations described in Appendix A.

Powder	Mean Particle Size [µm]	C_V
P-α60	60	0.5
P-α	6	1.4
P-β	12	0.4

Table 4.2: The specific surface area and calculated particle size of the sintering aids assuming spherical particles.

Powder	Specific surface area [m^2/g]	Particle size [µm]
P-α	1.4	14
P-β	0.7	28

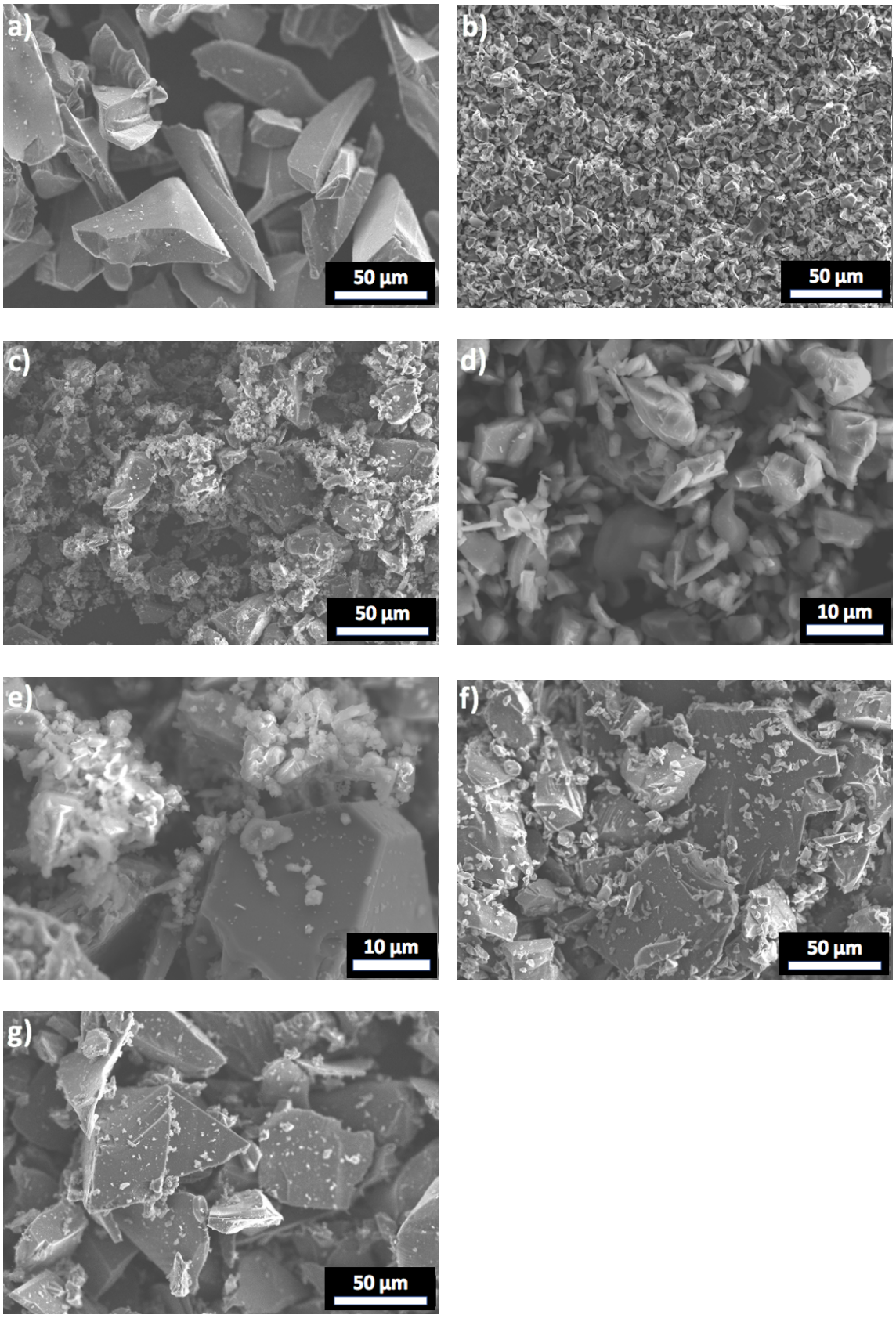

Figure 4.2: SEM micrographs of the as-received powders, P-α60 (a), P-α (b, d) and P-β (c, e) and the powder mixtures P-α60/α (f) and P-α60/β (g).

SEM images of the as-received powders presented in Fig. 4.2a - Fig. 4.2e show particles with elongated and non-spherical morphology with sharp edges. Some particles have a plate-like structure and in the P-β powder crystals with cubic morphology are observed. The micrographs presented in Fig. 4.2d and Fig. 4.2e show a broader variation in particle size for the P-β powder than P-α. Fig. 4.2f and Fig. 4.2g show a homogeneous distribution of the sintering aids with P-α60 in P-α60/α and P-α60/β, respectively.

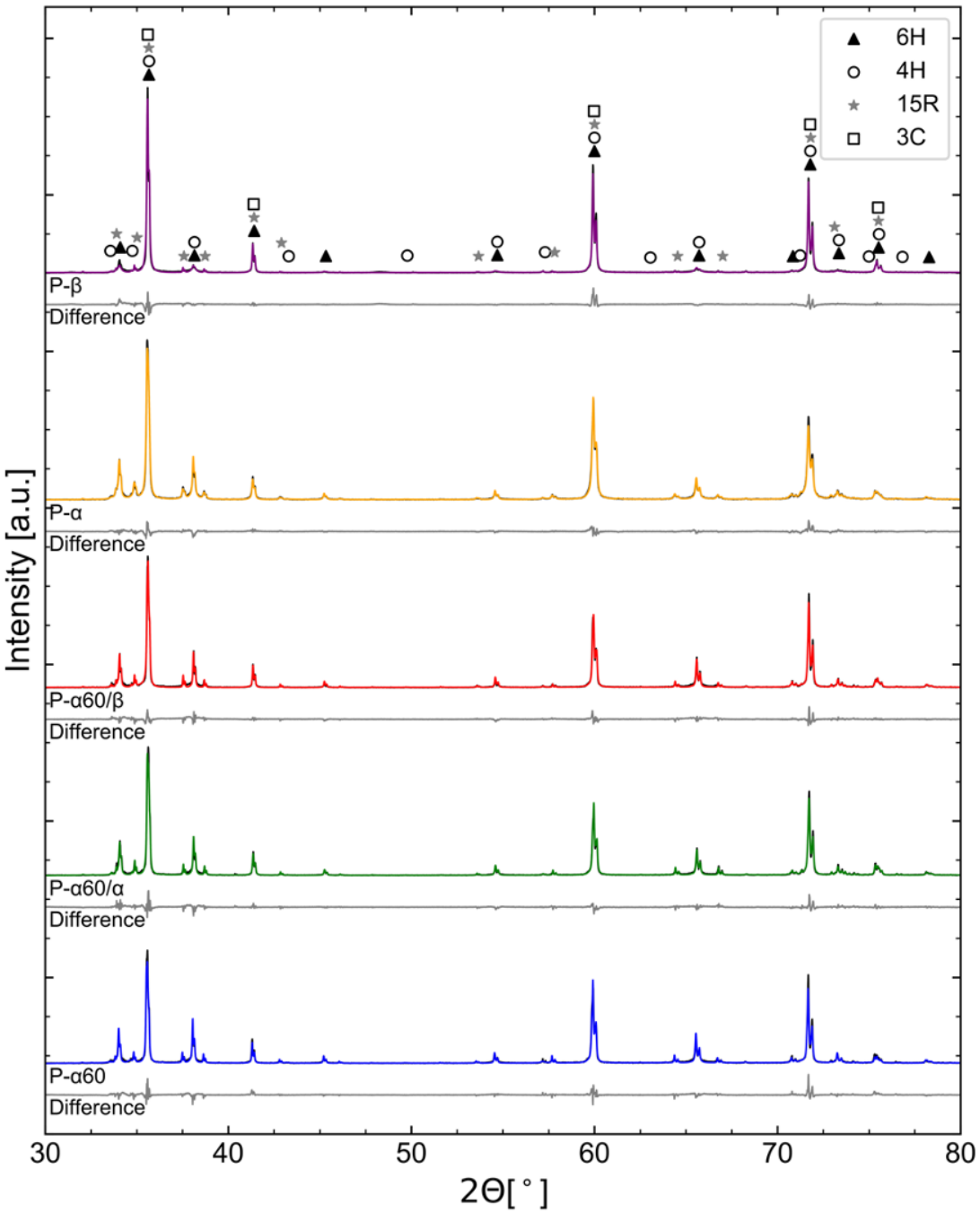

Figure 4.3: X-ray diffractograms of as-received SiC-powders and powder mixtures with their respective fitted diffractograms and differences from TOPAS. Markers show the reported reflections for 6H, 4H, 15R and 3C.

XRD patterns of the as-received powders and the powder mixtures are presented in Fig. 4.3, together with the diffraction pattern calculated by Rietveld refinement in TOPAS and the difference between the measured and calculated pattern. Each diffraction pattern shows diffraction lines of several SiC-polytypes. A slight shift in the 2Θ position of all diffraction lines is observed. Peak splitting is observed due to Cu-Kα_2 contamination. Rietveld refinement of the XRD-patterns of the as-received powders show that the dominating polytype of P-α60 and P-α is 6H. No cubic SiC was observed. 3C (70 %) and 6H (20 %) were present in P-β. Polytypes 4H, 6H and 15R are present in P-α60, P-α60/α and P-α60/β.

Table 4.3: The relative weight percentages of 4H (PDF 04-010-5697), 6H (PDF 04-010-5698), 15R (PDF 04-008-4948) and 3C (PDF 00-029-1129) in the as-received powders obtained by Rietveld refinement.

Powder	**Phase**	**Quantity [wt%]**	$\mathbf{R_{wp}}$
P-α60	4H	6.4	15
	6H	67.2	
	15R	26.4	
P-α	4H	5.7	9
	6H	82.9	
	15R	11.4	
P-β	4H	3.3	14
	6H	19.7	
	15R	6.7	
	3C	70.3	

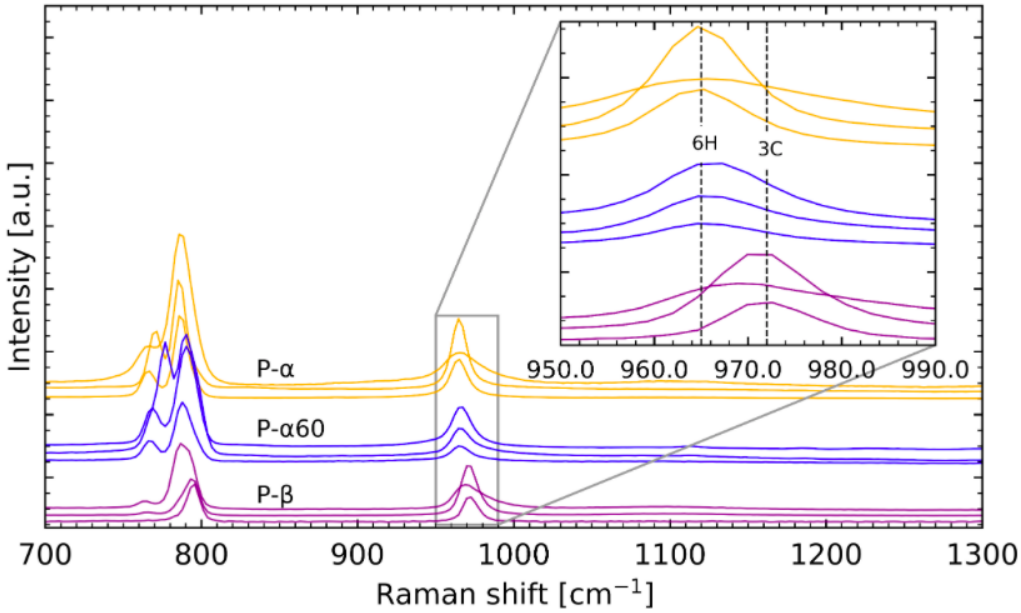

Figure 4.4: Raman spectra of the as-received powders P-α, P-α60 and P-β. The Raman shift for the two polytypes 3C and 6H are shown in the inset.

Fig. 4.4 presents the three Raman spectra of the as-received powders. Reproducible measurements of P-α60 and P-α result in a Raman band at 965 cm^{-1}. The Raman spectra of P-β show some variation as Raman shift is observed at 972 cm^{-1} and in the range range 960 - 980 cm^{-1}.

4.2 Spark Plasma Sintering

The relative displacement in the z-direction during spark plasma sintering is presented in Fig. 4.5. Densification occurs when the relative displacement increases within the 5 min holding time initiated at the dashed line. Before the dashed line each sample is compressed due to the increased uniaxial pressure from 20 MPa to 50 MPa. When the load reached 50 MPa the 5 min holding time begins and the displacement curves demonstrate some expansion as the slope decreases. Densification then occurs as the slope increases without further changes in pressure or temperature. The majority of the densification occur within the first 100 s of the holding time.

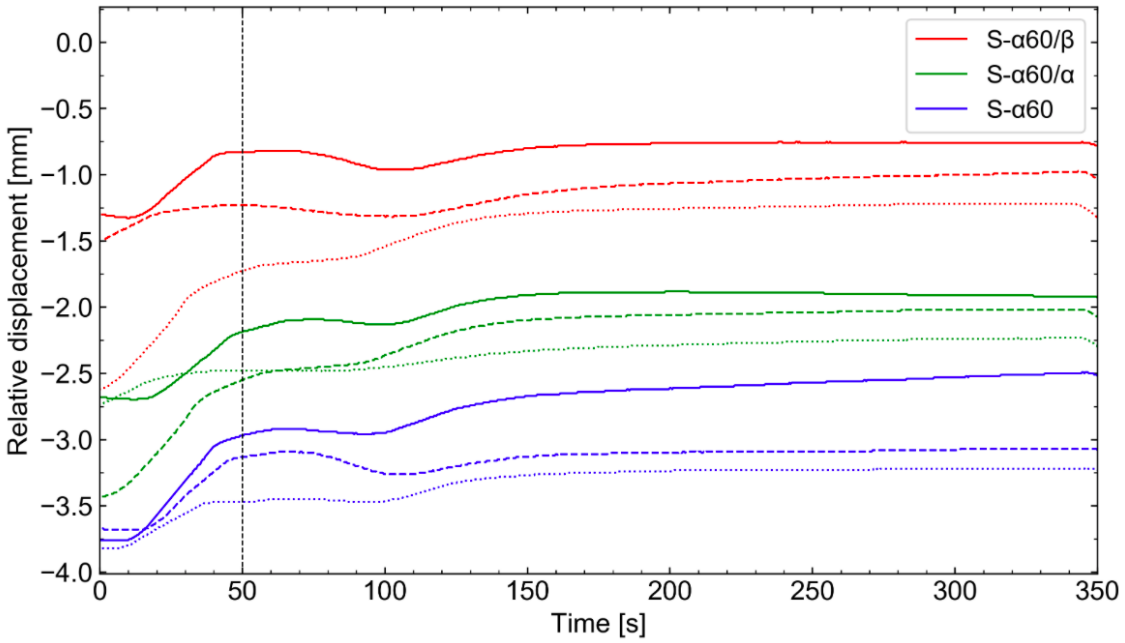

Figure 4.5: The measured displacement during the 5 min holding time of spark plasma sintering. For each composition the top line is sample 1, middle line sample 2 and bottom line sample 3.

4.3 Density and Porosity of Sintered Silicon Carbide

Table 4.4 shows the calculated density and porosity of each sample measured by Archimedes method. The relative density increases when adding sintering aids, but only by a maximum of 8 %. Addition of P-α to P-α60 results in the highest relative density, varying between 77 - 80 %. The relative density of S-α60/β was 75 - 76 %. Porosity was open for each sample as described by calculations in Appendix C.

Table 4.4: The relative density and total porosity of the sintered samples.

Sample	**Relative density** [%]	**Total porosity** [%]
S-α60-1	72	28
S-α60-2	73	27
S-α60-3	74	26
S-α60/α-1	77	23
S-α60/α-2	78	22
S-α60/α-3	80	20
S-α60/β-1	76	24
S-α60/β-2	75	25
S-α60/β-3	76	24

4.4 Fracture Surface Analyses

Photos of reconstructed samples after the ball-on-ring test are shown in Fig. 4.6a, Fig. 4.6c and Fig. 4.6e. The fracture origin of each sample is located below the position of the ball during testing. The microstructures presented in Fig. 4.6b, Fig. 4.6d and Fig. 4.6f, show that the area around the fracture origin appears homogeneous and that the fracture surfaces are transgranular. No significant variations in porosity are observed from the micrographs.

Evidence of the effect of the spark plasma between adjacent particles is observed for all compositions and is presented in Fig. 4.7a - Fig. 4.7c. Areas marked by red circles show necking between grains. The fracture surface of pure β-SiC show hexagonal morphology with a plate-like structure of the grains after sintering, marked by red arrows in Fig. 4.7d.

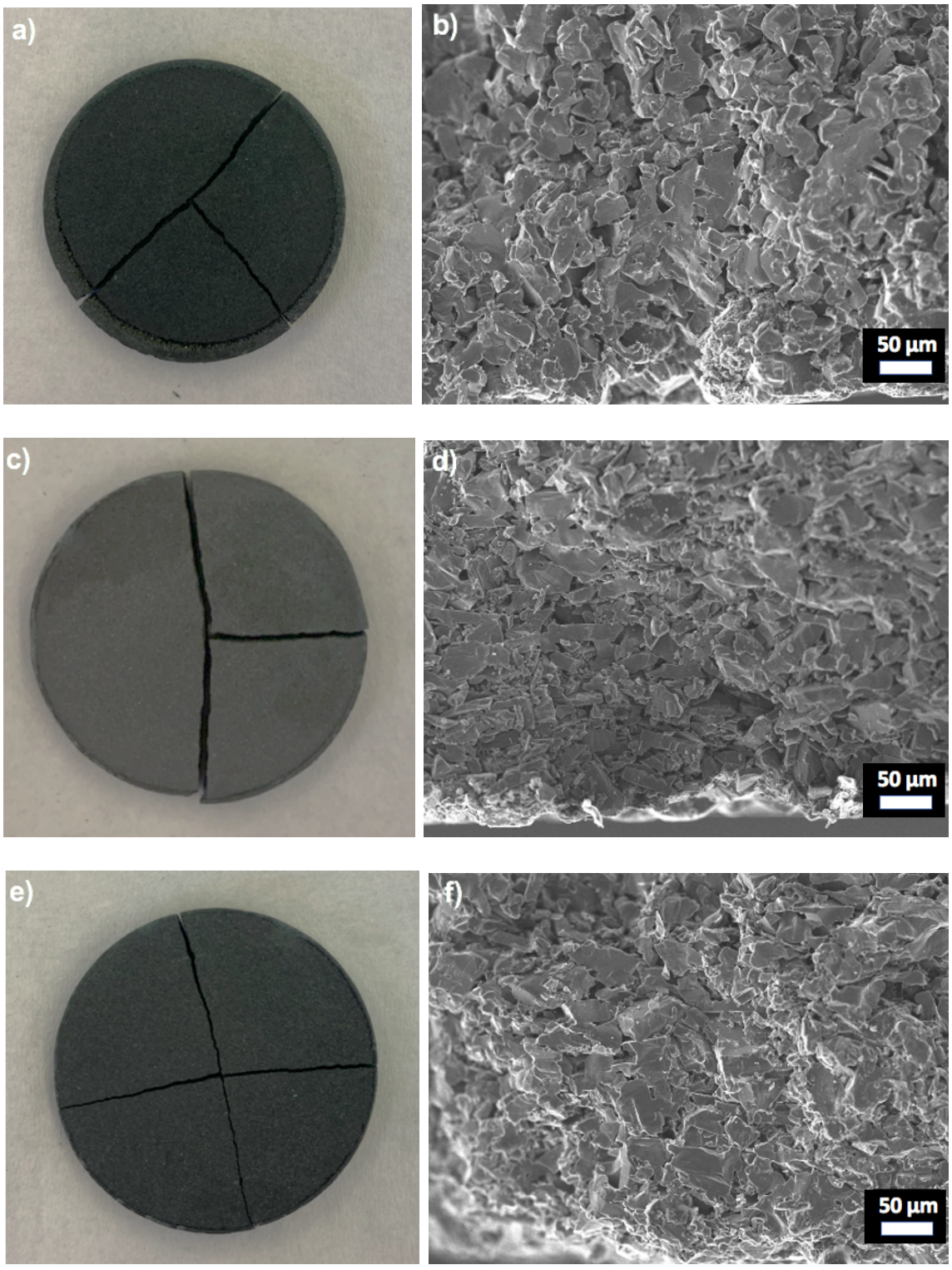

Figure 4.6: Photos of reconstructed samples of a) S-α60, c) S-α60/α and e) S-α60/β and SEM micrographs of their respective fracture surfaces.

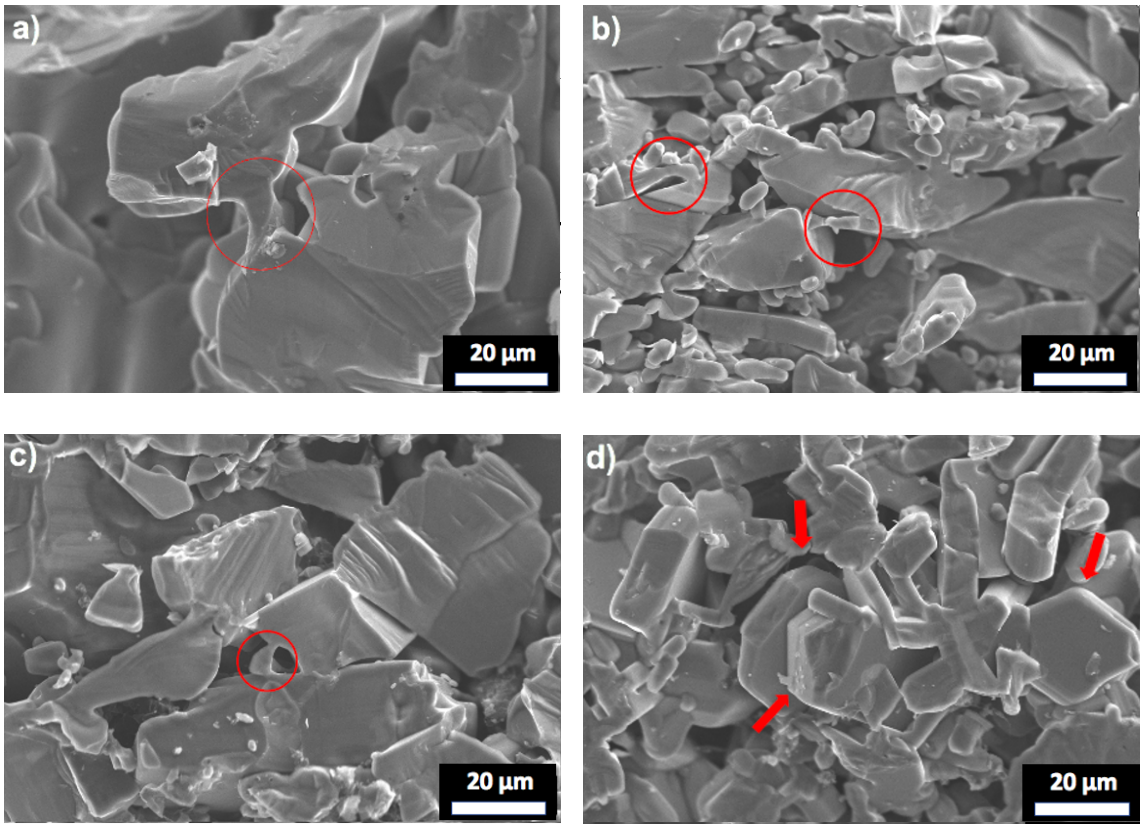

Figure 4.7: SEM micrographs of the fracture surface of a) S-α60, b) S-α60/α and c) S-α60/β. Red circles highlight the effect of the spark plasma between particles and the red arrows show grains with hexagonal morphology in the sintered β-SiC.

4.5 Phase Composition of Sintered Silicon Carbide

X-ray diffractograms of the sintered samples and the corresponding powders, P-α60, P-α60/α, P-α60/β and P-β, are presented in Figs. 4.8 - 4.11, respectively. The diffractograms for P-α60 and S-α60 show diffraction lines for 4H ($2\Theta = 57.3°$), 6H ($2\Theta = 45.3°$) and 15R ($2\Theta = 37.6°$), confirming the presence of these polytypes. The relative intensity of these reflections have decreased after sintering, while intensities at $2\Theta = 35.6°$ and $2\Theta = 60.0°$ have increased. All 3C reflections overlap with reflections of 4H, 6H and 15R.

X-ray diffractograms of P-α60/α and S-α60/α confirm the coexistence of polytypes 4H, 6H and 15R from diffraction lines at $2\Theta = 34.7°$, $2\Theta = 70.8°$, and $2\Theta = 37.6°$, respectively. Increased intensities of reflections at $2\Theta = 35.6°$, $2\Theta = 60.0°$ and $2\Theta = 71.8°$ are observed after sintering. Similar trends are presented in Fig. 4.10, but the increased intensity is mainly observed at $2\Theta = 35.6°$ and $2\Theta = 75.5°$.

Fig. 4.11 shows that the intensity of most reflections are higher in the P-β powder than the sintered sample. The polytypes 4H, 6H and 15R are identified by diffraction lines as for Figs. 4.8 - 4.10.

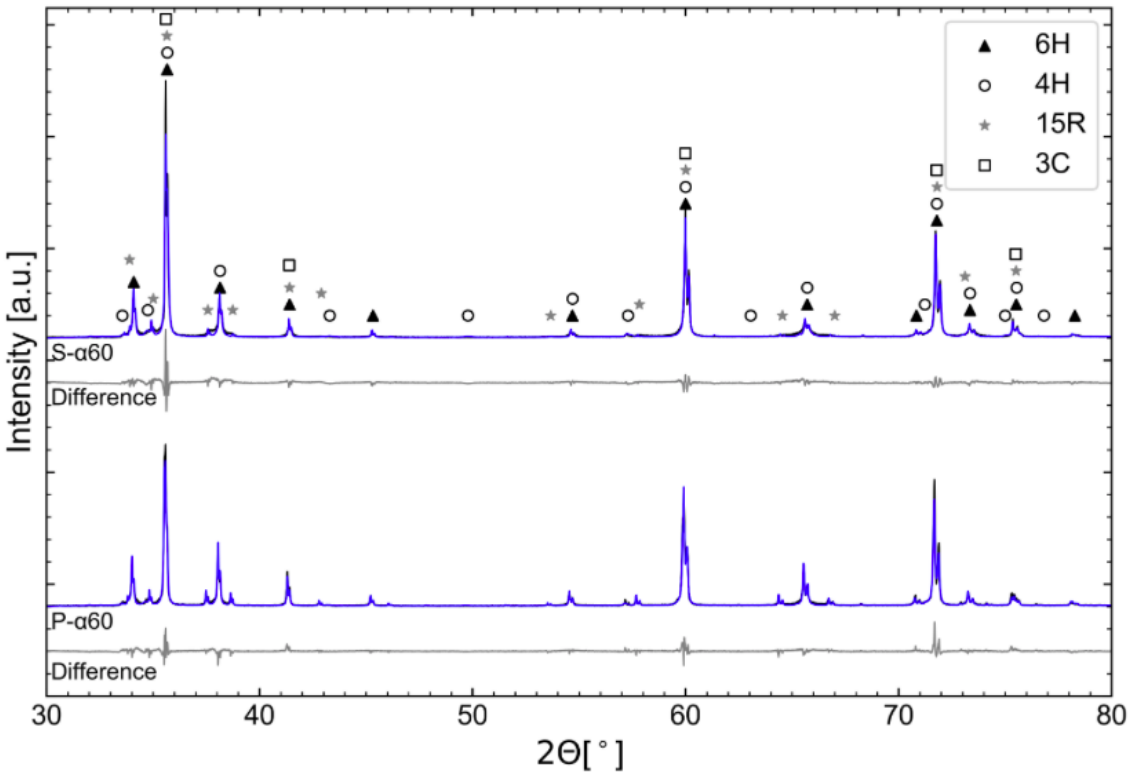

Figure 4.8: X-ray diffractograms of P-α60 and S-α60. Markers show the reported reflections for 6H, 4H, 15R and 3C.

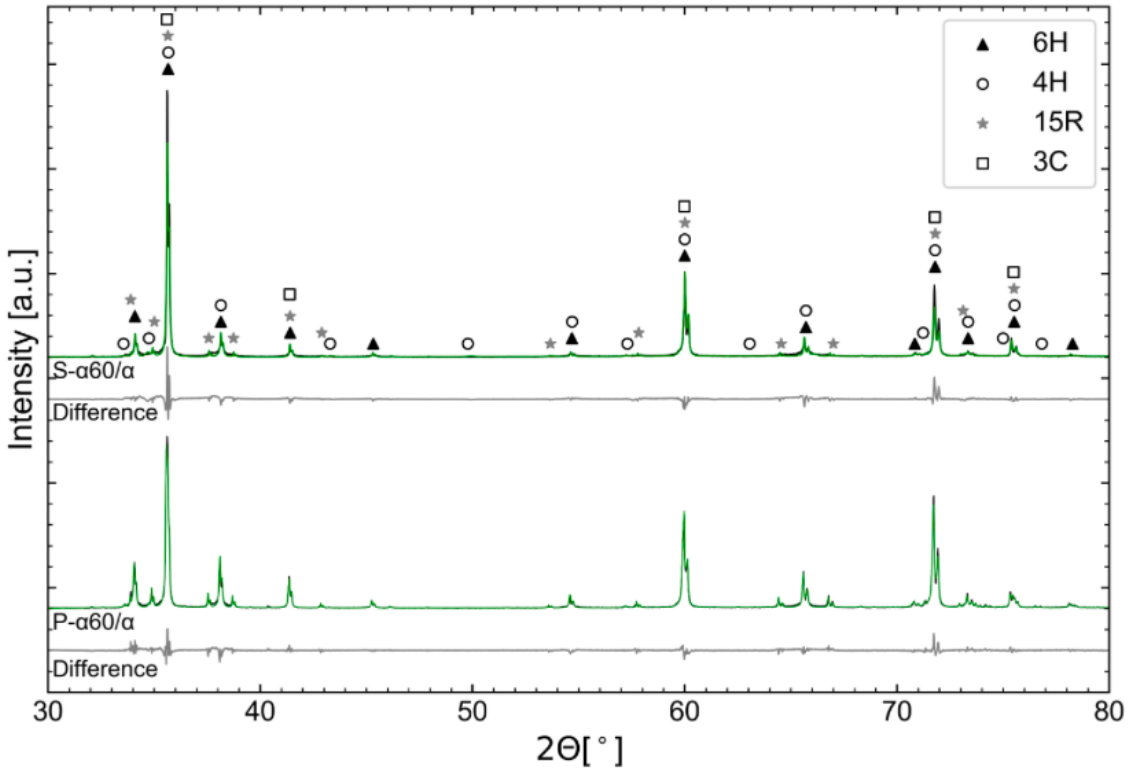

Figure 4.9: X-ray diffractograms of P-α60/α and S-α60/α. Markers show the reported reflections for 6H, 4H, 15R and 3C.

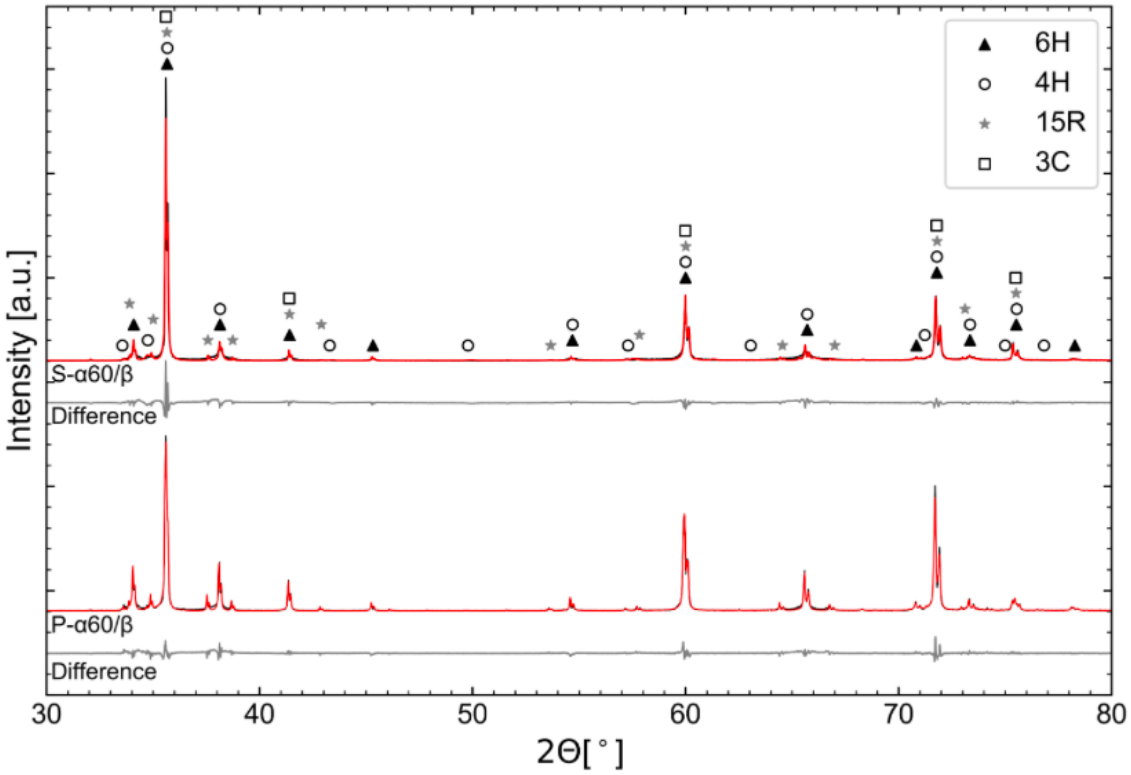

Figure 4.10: X-ray diffractograms of P-$\alpha 60/\beta$ and S-$\alpha 60/\beta$. Markers show the reported reflections for 6H, 4H, 15R and 3C.

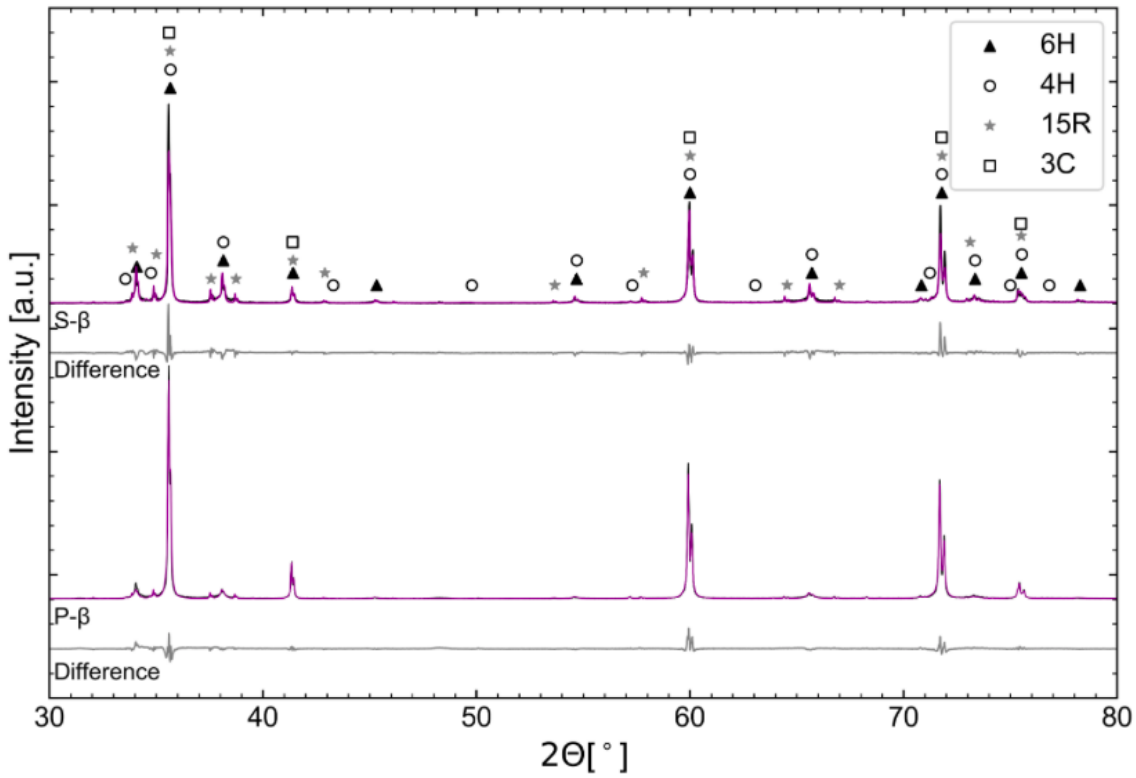

Figure 4.11: X-ray diffractograms of P-β and S-β. Markers show the reported reflections for 6H, 4H, 15R and 3C.

Results of the Rietveld refinement of XRD patterns of sintered samples are presented in Table 4.5. 6H is the main phase in the sintered samples, and smaller quantities of 4H and 15R are detected. No 3C is present after sintering.

Table 4.5: The relative weight percentages of 4H (PDF 04-010-5697), 6H (PDF 04-010-5698) and 15R (PDF 04-008-4948) in the sintered samples obtained by Rietveld refinement.

Powder	**Phase**	**Quantity [wt%]**	$\mathbf{R_{wp}}$
S-α60	4H	7.2	15
	6H	74.7	
	15R	18.1	
S-α60/α	4H	6.8	16
	6H	80.4	
	15R	12.8	
S-α60/β	4H	9.2	13
	6H	81.3	
	15R	9.5	

Raman spectra of the as-received P-α60 are presented in Fig. 4.12. A Raman band is observed at 965 cm^{-1}, confirming the presence of 6H. The Raman shift at 972 cm^{-1} is not observed in any of the spectra, indicating that the powder does not contain 3C polymorph. The only Raman band observed for the sintered sample is located at 965 cm^{-1}.

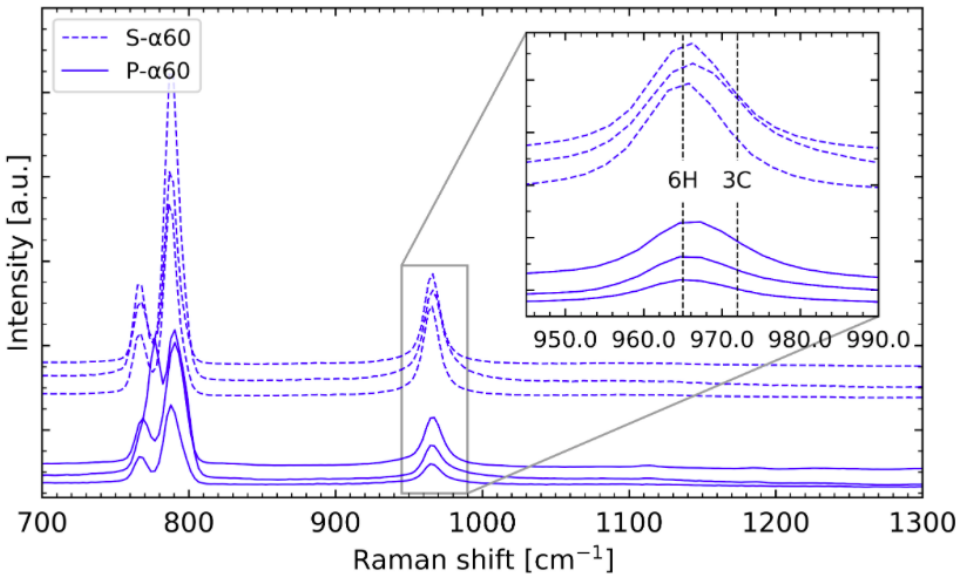

Figure 4.12: Raman spectra of as-received P-α60 and S-α60.

The Raman spectra of as-received P-β show a Raman band at the 3C shift, 972 cm^{-1}, for two point measurements. One measurement shows a band covering the range 960 - 980 cm^{-1} and thus includes both 3C and 6H. After sintering (20 min) each Raman spectra show a shift at 965 cm^{-1}.

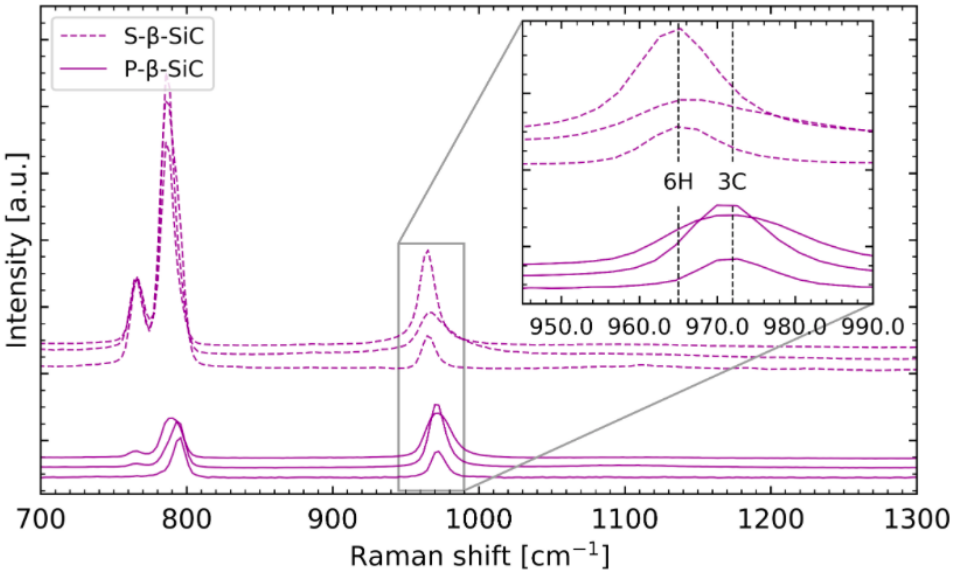

Figure 4.13: Raman spectra of as-received P-β and S-β sintered for 20 min.

Fig. 4.14 shows the Raman spectra of P-α60/β and the sintered S-α60/β sample. For the powder, Raman bands of both 3C and 6H are observed at 972 cm^{-1} and 965 cm^{-1}, respectively. After sintering (5 min) a shift at 965 cm^{-1} is observed.

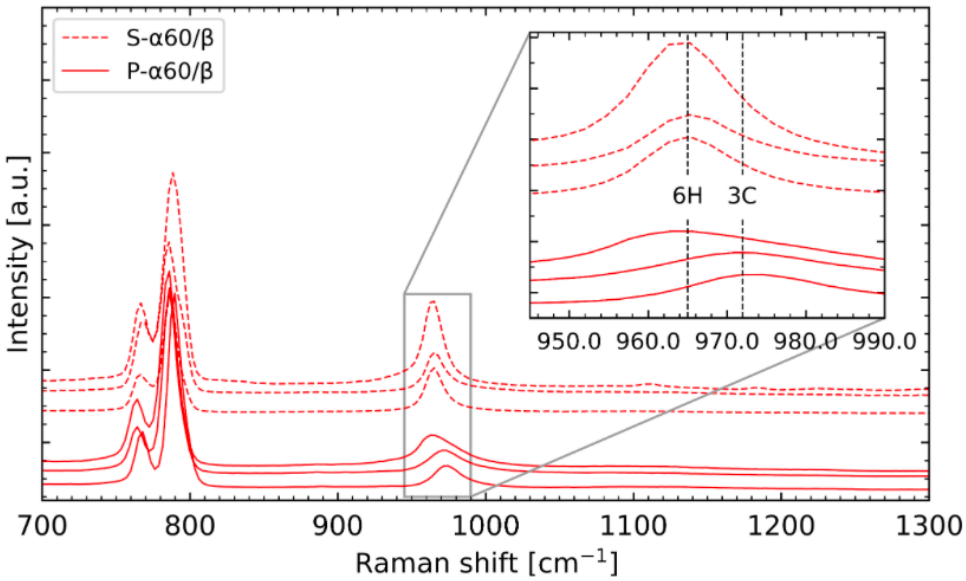

Figure 4.14: Raman spectra of the powder mixture P-α60/β and the sintered S-α60/β sample.

4.6 Mechanical Properties of Sintered SiC

Fig. 4.15 shows the stress-strain relationship of the SiC samples presented in Table 3.5. Each sample demonstrates a non-elastic behaviour during compression. The effect of α-SiC and β-SiC as sintering aids is evident as the critical stress is significantly lower for S-α60 than S-α60/α and S-α60/β. The deviations from linear behaviour observed for S-α60/α-3, S-α60/β-2 and S-α60/β-3 are due to irregular surfaces after microblasting and porosity close to the sample surface beneath the position of the loading ball.

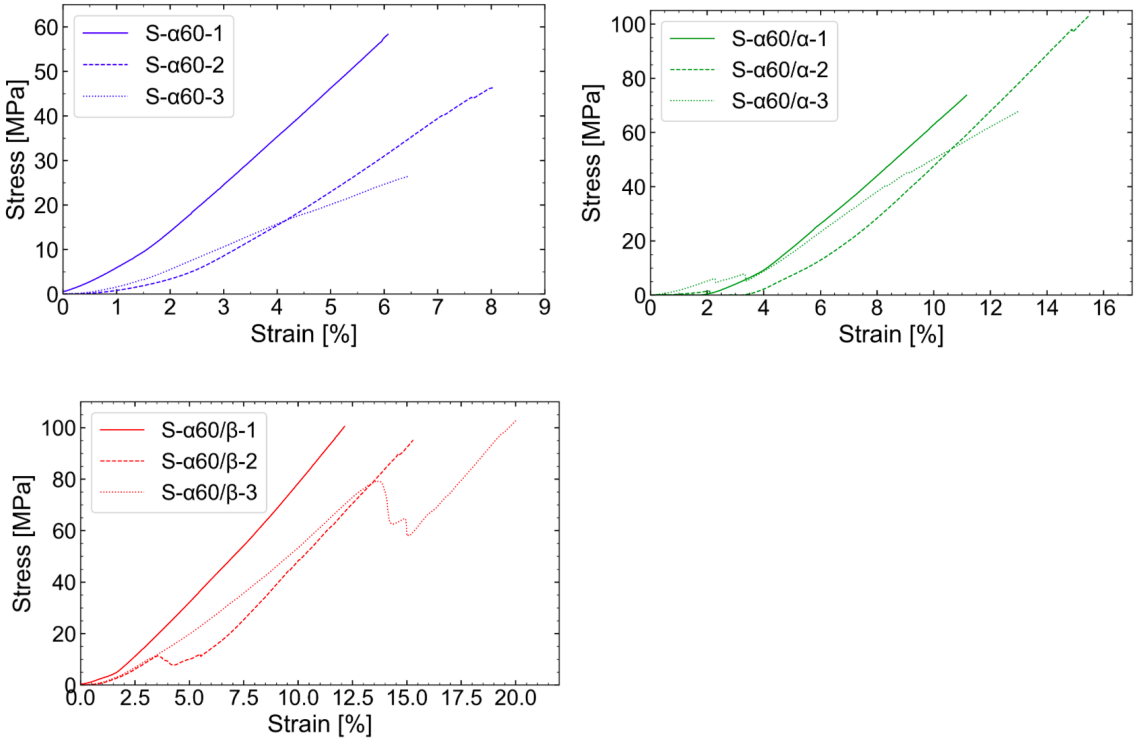

Figure 4.15: The compressive stress and strain measured during ball-on-ring testing of spark plasma sintered S-α60, S-α60/α and S-α60/β.

Table 4.6 presents the mean Young's modulus, biaxial strength and apparent hardness of the SiC samples. An increase in the Young's modulus is observed when adding sintering aids to P-α60. There are significant variations in the standard deviation, where the most evident deviation is observed for S-α60, having the lowest estimated Young's modulus. The biaxial strength more than doubles when using α-SiC and β-SiC as sintering aids. The mean biaxial strength is highest for S-α60/β, which also has the smallest standard deviation.

Table 4.6: Calculated mean with standard deviation of the Young's modulus, biaxial strength and apparent hardness for each composition of sintered SiC. Data for each measurement are presented in Appendix D.2 and Appendix E.

Sample	**Young's Modulus [GPa]**	**Biaxial Strength [MPa]**	**Apparent hardness [HV]**
S-α60	78 ± 25	7 ± 2	375 ± 30
S-α60/α	84 ± 19	20 ± 3	173 ± 14
S-α60/β	93 ± 3	21 ± 2	224 ± 27

The apparent hardness of S-α60, S-α60/α and S-α60/β is presented in Fig. 4.16 and Table 4.6. The measured data are reported in Appendix E. S-α60 has significantly higher hardness than S-α60/α and S-α60/β, despite having the lowest biaxial strength and elasticity. Fig. 4.17 shows SEM micrographs of indents on the S-α60 (a), S-α60/α (b) and S-α60/β (c) surfaces. The indents are indistinct due to the high degree of porosity.

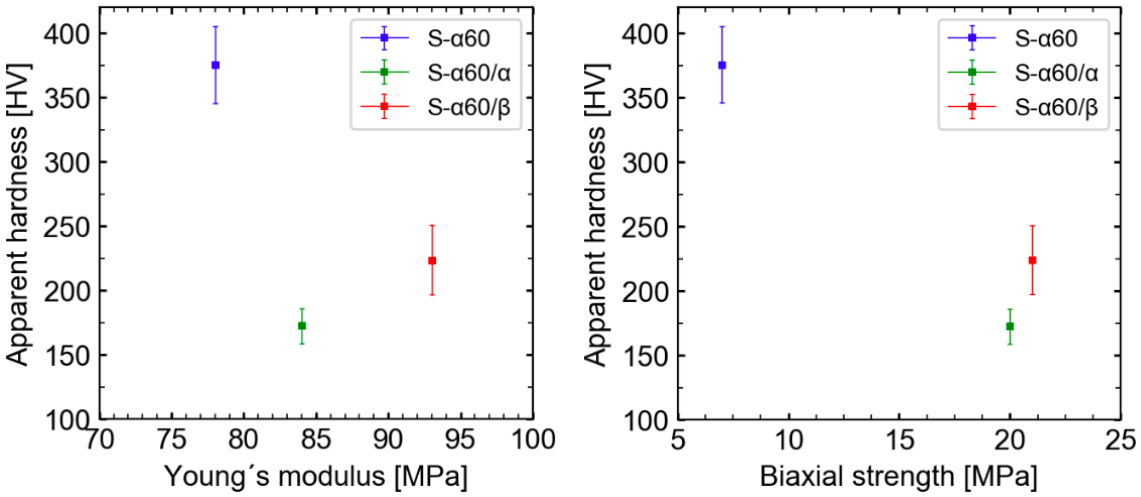

Figure 4.16: The measured hardness of S-α60, S-α60/α and S-α60/β plotted against the estimated Young´s modulus and biaxial strength.

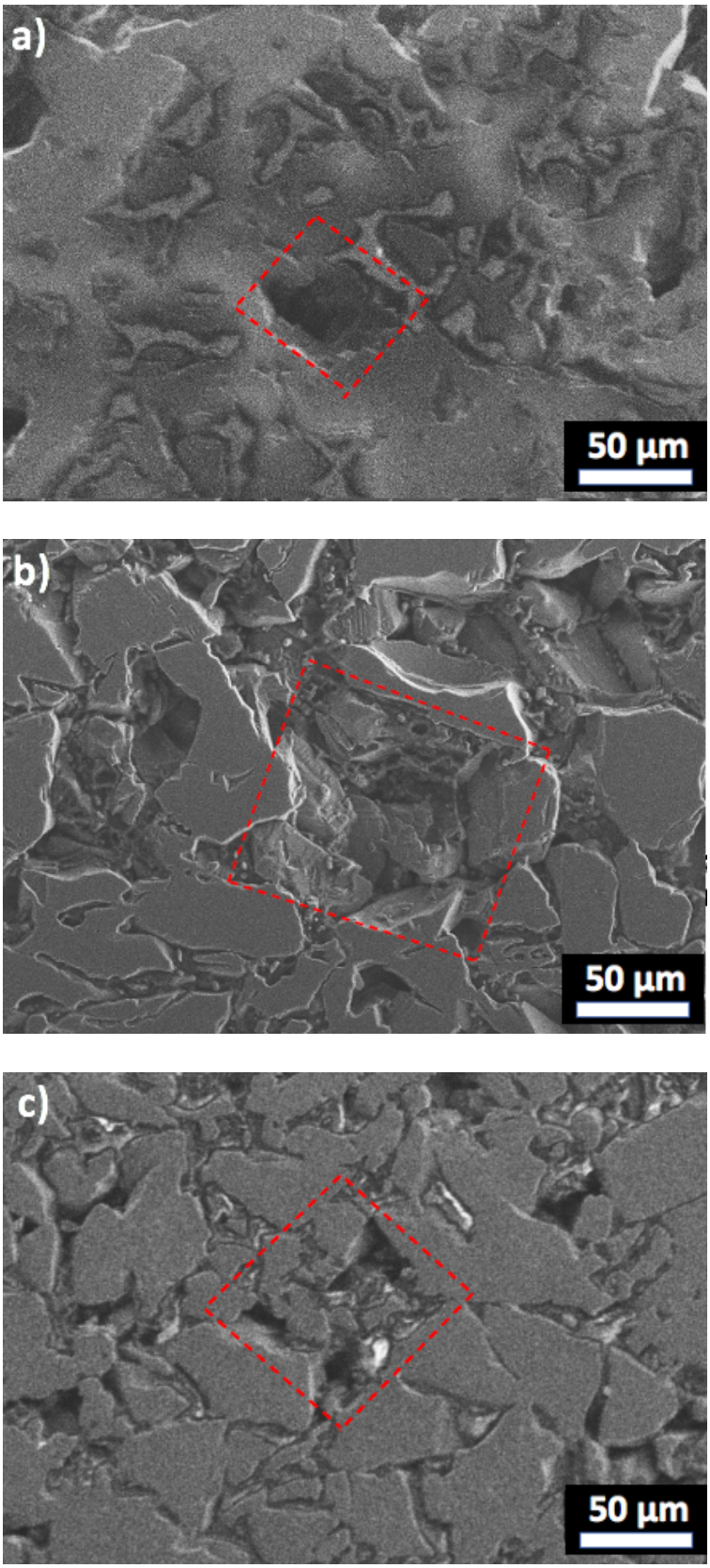

Figure 4.17: SEM micrographs of S-α60 (a) S-α60/α (b) and S-α60/β (c) after Vickers micro-indentation.

5 Discussion

5.1 Powder Properties

The particle size distributions presented in Fig. 4.1 are in good agreement with the micrographs in Fig. 4.2. The broad PSD of P-β compared to P-α is ideal to achieve a higher packing density. However, the smaller mean particle size of the P-α (5 µm) provides a higher surface area, which will increase the driving force for densification. In addition, the high coefficient of variation of P-α compared to P-β means that the sinterability of P-α60/α should be superior to that of P-α60/β, according to Khalil et al. [45]. The homogeneous distribution of P-α and P-β in P-α60 is ideal to obtain a homogeneous microstructure after sintering.

P-α has the highest specific surface area of the sintering aids, as expected from the particle size distributions. However, the measurements are based on the assumption of spherical particles, which the micrographs clearly demonstrate is not the case. In addition, the work by Elder et al. [49] suggests that the surface area is significantly reduced when oxygen is removed from the surface of the SiC powder by SiO_2 reduction.

Table 3.1 show that some elemental C is present in the as-received powder. The C can react with SiO_2 according to Eq. (5.1) in the temperature range 1100 to 1300 °C [102].

$$C(s) + SiO_2(s) \rightarrow SiO(g) + CO(g) \tag{5.1}$$

This reaction can therefore explain the increased partial pressure observed at approximately 1150 °C. Further, the work by Tangstad [103] states that reduction of SiO_2, and thus removal of oxygen, occurs above 1800 °C by Eq. (5.2).

$$2SiO_2(s) + SiC(s) \longrightarrow 3SiO(g) + CO(g) \tag{5.2}$$

This is below the sintering temperature used in the present work, and as presented by Fig. 5.1 the partial pressure during SPS increases between 1800 and 1900 °C. This is attributed to oxygen removal by Eq. (5.2), because the amount of elemental C is not sufficient to remove all SiO_2 by Eq. (5.1). Because of the low initial surface area, non-spherical particles and oxygen removal causing further reduction of surface area, the densification during spark plasma sintering is not further discussed with regards to the surface area of the as-received sintering aids.

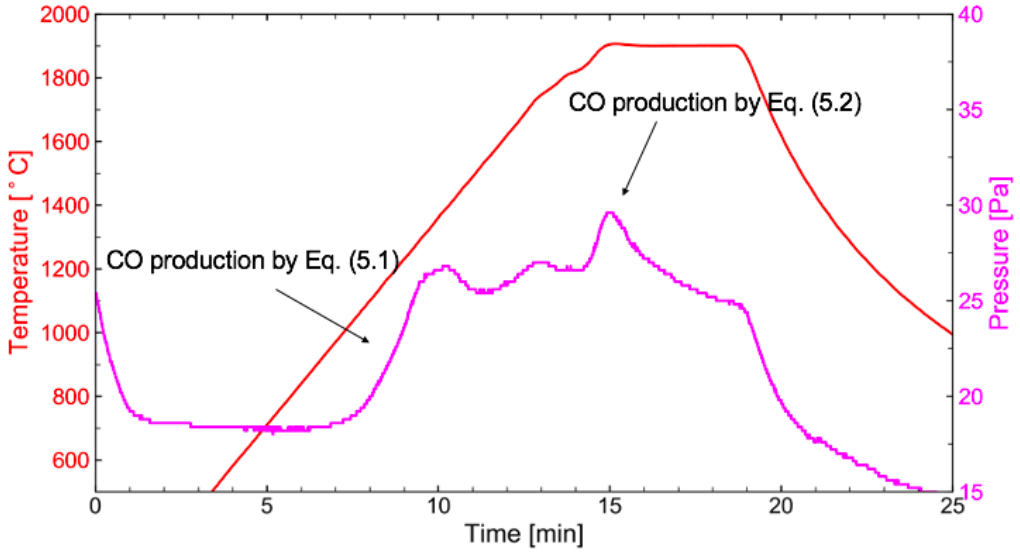

Figure 5.1: The measured temperature and gas pressure in the vacuum chamber during spark plasma sintering of P-α60. The gas pressure increases above 1800 °C as indicated in the figure.

Qualitative phase analysis by XRD of the as-received powders and powder mixtures was challenging due to overlapping diffraction lines of 3C with 4H, 6H and 15R. The relative intensities observed at $2\Theta = 35.6°$, $2\Theta = 60.0°$ and $2\Theta = 71.8°$ were significantly higher than other diffraction lines. For 6H, the diffraction lines at $2\Theta = 35.6°$, $2\Theta = 60.0°$ and $2\Theta = 71.8°$ are caused by reflections from the (1 0 2), (1 0 8) and (1 0 10) planes, respectively. The high intensity of these diffraction lines was therefore attributed to preferred orientation along the [1 0 1] direction. Alignment in this specific crystallographic direction may be caused by the plate-like grains of the as-received powders, presented in Fig. 4.2.

Raman spectroscopy of the as-received powders and powder mixtures was conducted to establish the presence of 3C in P-β and P-α60/β. Reference measurements of P-α60 and P-α show that they do not contain any cubic SiC. As one Raman spectrum of P-β show overlap of the 3C and 6H shifts, 6H is likely present in P-β. This is expected, as there is a gradual transition from α-SiC to β-SiC moving radially outwards from the core in the Acheson furnace.

Because the 3C polymorph was only observed in the Raman spectrum of P-β, the 3C structure was only included when assessing the P-β powder in the Rietveld refinement. The best fit of P-β was observed when 3C was the dominating phase (70 %), with small amounts of 4H, 6H and 15R present. This is in good agreement with the X-ray diffractogram and Raman spectrum. The deviations between the refined XRD pattern and measured XRD pattern are mainly due to high intensities. Slight peak broadening of selected diffraction lines is attributed to the inevitable presence of stacking faults, while the over-representation of specific diffraction lines arise from preferred orientation.

5.2 Optimization of the Spark Plasma Sintering

The first powder that was sintered, α250, typically followed the curve marked "α250 Success" in Fig. 5.2. However, variations were observed in the applied current, and during one sintering the program was shut down automatically due to too large changes in the z-axis displacement. This is described by the curve labeled "α250 Decomposed" in Fig. 5.2. The applied current was significantly higher than for the successful experiments, and visual inspection of the graphite die showed that the SiC had decomposed. According to the binary phase diagram presented in Fig. 2.4 the true temperature must have been significantly higher than the measured temperature of 1870 °C. During the next experiment using the P-α250, the current followed the same trend as the decomposed sample, and the sintering was therefore manually shut down.

The process variables were the same, the powders came from the same batch, the graphite equipment was checked and an additional pyrometer was used to confirm that the one in use was correct. The most likely problem was thought to be poor contact within the die due to the coarse grain size. In addition, the presence of oxides can cause local overheating according to Locci et al. [40]. Another powder (60 µm) was tested, and after five rounds of sintering the current always followed the solid curve named "α60 Success" in Fig. 5.2. P-α250 was replaced by P-α60, and it was concluded that the coarse grain size was the problem, not the presence of SiO_2 on the powder surface.

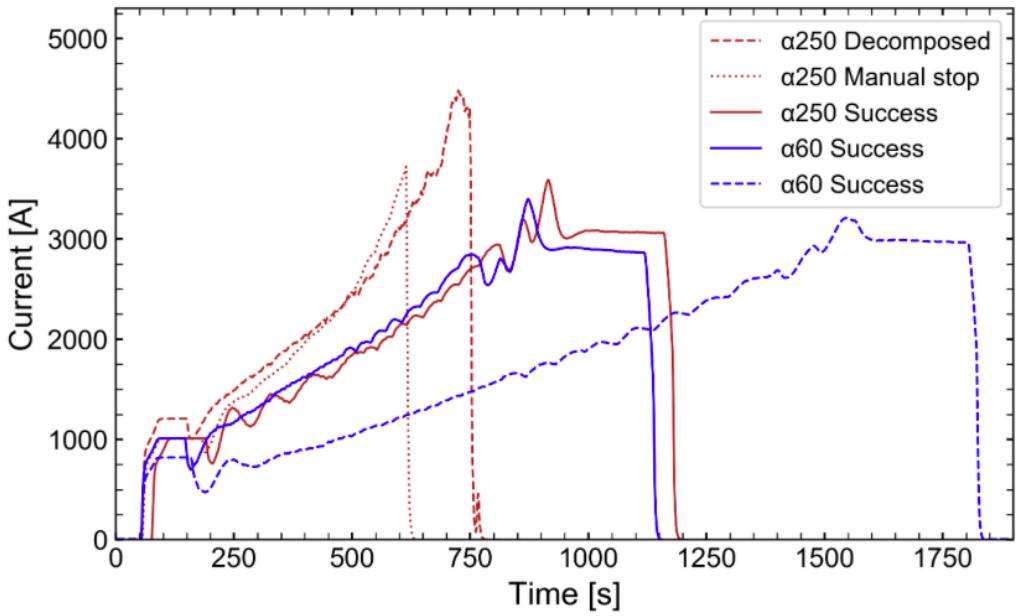

Figure 5.2: The measured current upon spark plasma sintering of α-SiC powders with different particle sizes.

When the same problem of high current reappeared for P-α60/α-3 on the final sintering, another sintering program was tested. The power volume was reduced from 60 % to 50 % to restrict the power, and thus the current.

To compensate for this the heating rate was changed from 100 °C min^{-1} to 50 °C min^{-1} as described by the dashed line named "α60 Success" in Fig. 5.2. This allowed the SiC-powder to follow the pre-set program despite a lower power supply. The sintering temperature, pressure and holding time were kept the same. The sample was then successfully sintered by SPS despite a lower current, and the sample characterization did not reveal any differences due to the altered program.

5.3 Properties of Spark Plasma Sintered Silicon Carbide

5.3.1 Phase Composition

Preferred orientation is evident from the X-ray diffractograms of the sintered samples. The plate-like grains presented in Fig. 4.2 may become preferentially oriented due to the uniaxial pressing during SPS. [46] In addition, Grasso et al. [104] argue that preferred orientation can occur during spark plasma sintering of SiC due to thermal gradients. Because SiC has a higher resistivity than graphite, a thermal gradient will evolve in the axial direction during SPS. This facilitates for directional transport of gaseous species, and plate-like structures of α-SiC, similar to those in Fig. 4.7d, may form. As 6H is the dominating polytype after sintering it is likely that the high intensity of selected diffraction lines is caused by preferred orientation along the [1 0 1] direction.

Comparing the quantitative phase analyses of the as-received powders with the sintered samples it is evident that the 4H content has remained the same or increased. The presence of Al in the as-received powders is considered likely by visual inspection, owing to the black color. The relatively stable quantities of 4H in this work is therefore in accordance with the findings of Knippenberg, who stated that Al stabilizes the 4H polymorph [19]. The dominating presence of 6H polymorph after sintering also agrees with Fig. 2.10, which shows that 6H has the largest stability region around the sintering temperature.

Since the fraction of β-SiC in P-α60/β is relatively low, the Raman spectrum of P-β was measured to establish the presence of 3C. Some broadening of the 972 cm^{-1} Raman band is observed, which is expected for a polycrystalline sample. However, the Raman spectra of several measurements show reproducible results of a Raman band at 972 cm^{-1} for P-β and at 965 cm^{-1} for S-β. The shift from 972 cm^{-1} to 965 cm^{-1} was observed for S-α60/β as well and thus confirmed a phase transformation from 3C to 6H using the sintering program described by Fig. 3.3. This is in agreement with the work of Hidehiko [53], who observed a simultaneous reduction of 3C and increase of 6H in the temperature range 1800 - 1900 °C. Lodhe [52] observed the same transition above 1600 °C, using SiC that was pyrolyzed in an Ar atmosphere before SPS.

5.3.2 Density and Microstructure

The relative density of the spark plasma sintered samples increased most when using α-SiC as a sintering aid, from a mean of 73 % without sintering aids, to 78 %. A smaller increase was measured for the samples containing 10 wt% β-SiC, with an average of 76 %. This coincides with the theory introduced by Khalil et al.[45], as P-α had the highest coefficient of variation and smallest mean particle size. Biswas [7] reported a relative density above 98 % at similar sintering conditions, but the SiC particles were in the range 30 - 50 nm. Montón et al. [44] produced samples of 91 % relative density by SPS at 2200 °C when the mean grain size was 2 µm.

These results indicate that the time necessary to reach a specific degree of densification relies heavily on the particle size, which is in agreement with Fig. 2.7. Assuming grain boundary diffusion is the only sintering mechanism, estimations by Eq. (2.11) show that a powder with mean particle size 250 µm would require 25 h sintering to reach 73 % densification, which for P-α60 (60 µm) took 5 min.

In addition to the particle size and PSD, the phase transformation from 3C to 6H has an effect on the densification. Table 2.1 shows that the transformation involves a slight decrease in density. According to Knippenberg [19] the phase transformation occurs by grain boundary diffusion. This would lead to densification because the phase transformation increases the mobility such that atoms rearrange and pores and dislocations diffuse along grain boundaries more rapidly [32] [19] [52]. However, Grasso et al. [104] state that the transformation occurs by gas phase, which would make the process coarsening. To determine how significant the effects of a phase transformation are, experiments performed with identical grain size and PSD would be necessary. In this study the densification is a sum of many variables.

Because the relative density was below 93 % the samples did not approach the final stage of solid-state sintering [36][2]. This is also confirmed by measurements by Archimedes method and SEM images, which showed that the porosity was open and that the pores were interconnected. Since the samples were at the intermediate stage of sintering the grain surface curvature and pore stability is not considered to be of importance, in accordance with the work of Kang. [32]

Because the measured z-displacement during sintering takes into account the graphite spacers and punches in addition to the powder, the obtained data presented in Fig. 4.5 will only be used for qualitative purposes. This is because thermal gradients in the graphite equipment can impact the measurements. For a quantitative assessment of the densification the data obtained by Archimedes method are sufficient.

The slopes describing the relative z-displacement during SPS show some variation for each sample composition, S-α60, S-α60/α and S-α60/β (Fig. 4.5). The trends of expansion and shrinkage appear similar for the samples. The observed expansion from 50 - 100 s may come from thermal instability in the graphite equipment before thermal equilibrium is established. Each curve indicates that densification occurs between approximately 100 and 150 s in Fig. 4.5.

The fracture surface microstructures of S-α60, S-α60/α and S-α60/β presented in Fig. 4.6 were homogeneous, coinciding with the homogeneous distribution of sintering aids observed by SEM imaging of the powder mixtures. The SEM micrographs show no abnormal grain growth, but the images presented in Fig. 4.7 show an evident change in grain morphology compared to the as-received powders. Consequently, densification by solid state sintering has occurred.

Necking between the grains is observed in the SEM images presented in Fig. 4.7a - Fig. 4.7c. The necks marked by red circles resemble those referred to as "spark plasma" by Zhang et al. [39] and are observed for S-α60, S-α60/α and S-α60/β. Zhang et al. [39] documented this phenomenon upon SPS of Cu nano-particles. This observation may confirm that necking between particles occur by the mechanism described by Fig. 2.9.

5.3.3 Mechanical Properties

From the stress-strain curves presented in Fig. 4.15 and Table 4.6 it is evident that additions of α-SiC and β-SiC to P-α60 has increased the biaxial strength of the sintered samples. An increase is expected from the increased density. However, although S-α60/α demonstrated a higher mean density than S-α60/β, the estimated biaxial strength was lower. Higher strength at lower density of S-α60/β indicates that β-SiC is more beneficial as a sintering aid than P-α if high strength is the goal. Grasso et al. [104] and Abderrazak [4] state that the phase transformation 3C $\rightarrow$ 6H creates plate-like grains which grow perpendicular to the applied load during SPS. Thus, the fracture toughness is enhanced through crack deflection. This may increase the biaxial strength also for S-α60/β.

The estimations of the biaxial strength are based on the measured stress and applied load during fracture of the samples. Fig. 4.15 shows that for S-α60/β the stress is almost identical for the three samples, giving a low standard deviation. The deviations in strain are attributed to the positioning of the loading ball and an uneven surface after microblasting. A slight displacement of the loading ball, e.g. by "falling" into a pore at the surface when the load is applied, would result in significant increase of the strain, but be too small for the Instron 5543 to recognise this as a sample fracture. The most evident example of such behaviour is described by the curve of S-α60/β-3 in Fig. 4.15.

The gauge length and load are set to zero right before initiating the test, meaning that if the operator does not adjusts the height between the mechanical load cell and test specimen identically for each sample, the measured strain is affected by this. For example, it is observed for S-α60/α-2 that the stress does not increase before the strain is close to 4 %, while for S-α60-1 the stress increases immediately. The entire stress-strain curve is then shifted to the right and the strain at fracture is not the real strain. Large variations in the Young's modulus are observed for S-α60 and S-α60/α without any clear relation to the density or dimension of the samples listed in Table D.3. This is also attributed to local variations of the sample surfaces and small variations in the positioning of the loading ball.

Fracture analysis by reconstruction of the samples revealed that the fracture origin was below the loading ball for each sample, corresponding to zone I in Fig. 2.16. This point is where the equibiaxial stress is the highest, and indicates that the sample is homogeneous. The model described by Eq. (2.21) is therefore valid for calculating the biaxial strength from the ball-on-ring test causing the fracture. Because of the high porosity and large grain size of the samples, the microstructure of the fracture surfaces revealed no distinct features such as mist and hackle. Microstructural flaws such as abnormal grain growth or clusters of porosity were not identified by SEM imaging. The biaxial strength is therefore likely to be dependent on the grain size and porosity rather than the flaw size.

A decrease of the apparent hardness calculated by Eq. (2.23) was observed for increasing strength, elasticity and porosity. This is the opposite of what is expected by e.g. Ryshkevitch, as demonstrated by Fig. 5.3. It is believed that the high hardness of S-α60 compared to S-α60/α ans S-α60/β is due to crushing of the surface in addition to the desired plastic deformation. Relative to values found in literature [4], the estimates of hardness presented in Fig. 4.15 are low. The varying hardness may be caused by the coarse grain size relative to the size of the indent, as described by Karandikar et al. [94].

Because of the indistinct indents, no further load was applied in an attempt of estimating the fracture toughness by Eq. (2.25). Hardness measurements by nanoindentation might have given more defined indents, but this was considered to not be representative for the entire sample.

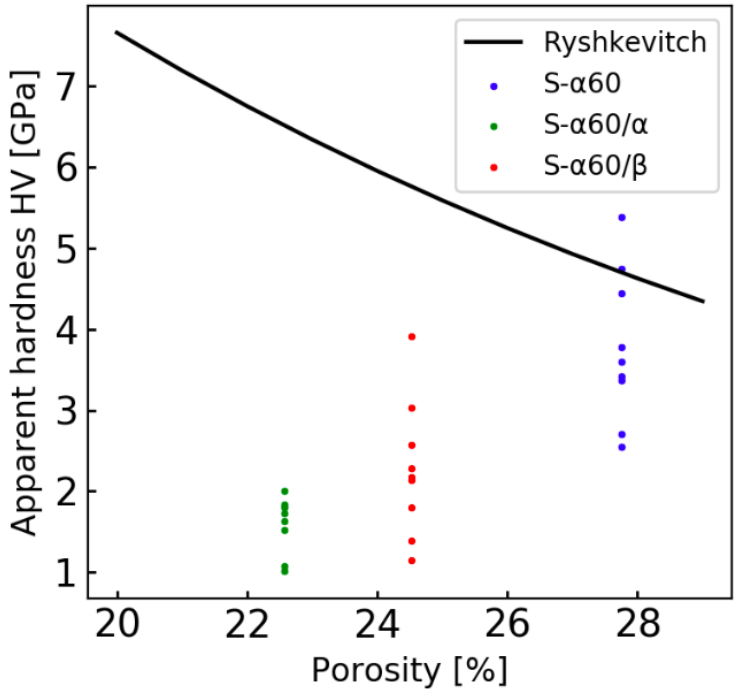

Figure 5.3: The measured hardness of S-α60, S-α60/α and S-α60/β compared to the estimated strength by Eq. (3.2) by Ryshkevitch [74].

5.4 Proposed Mechanism for the Density and Strength Behaviour

The higher strength of S-α60/β relative to S-α60/α is attributed to better necking between the grains, and proposed mechanisms to explain this behavior are illustrated in Fig. 5.4. Upon increasing the temperature, a momentarily high-temperature state between particles causes formation of SiC gas, which is then transformed to spark plasma by ionization as described by Fig. 2.9. Further, the temperature increase also initiates the 3C $\rightarrow$ 6H phase transformation, which according to Grasso et al. [104] occurs by evaporation-condensation.

The formation of spark plasma via gas phase is assumed to be similar for S-α60/α and S-α60/β, as their fracture surfaces demonstrate similar microstructures (Fig. 4.7). However, the mass transport by evaporation-condensation is only described for the 3C $\rightarrow$ 6H transformation. As evaporation-condensation is a coarsening sintering mechanism, this might be the cause of the lower density of S-α60/β compared to S-α60/α.

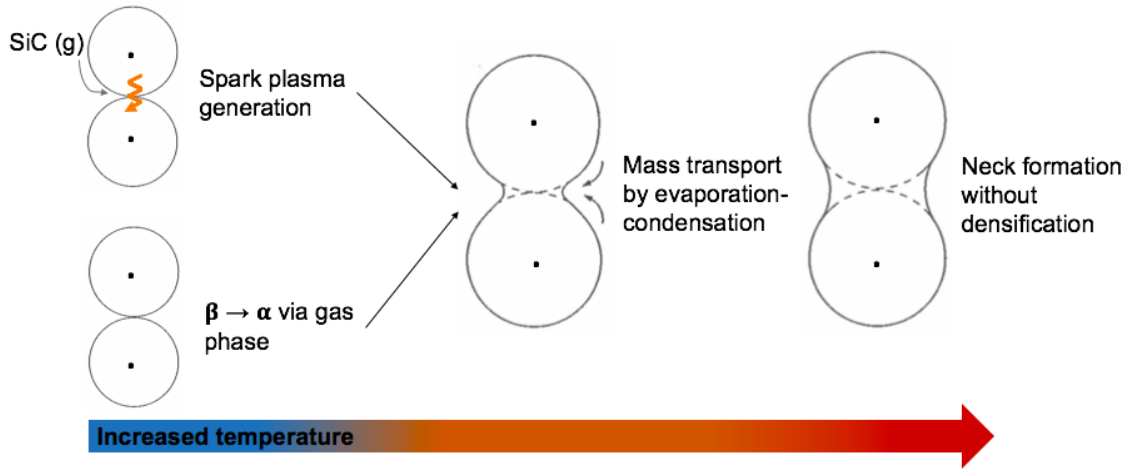

Figure 5.4: Proposed mechanism for strength increase without densification by formation of spark plasma and SiC-gas by the 3C $\rightarrow$ 6H phase transformation.

However, the necks formed by spark plasma sintering demonstrate a distinct concave curvature, as shown by Fig. 4.7. The SiC gas formed by the phase transformation will therefore condense at these sites. This results in increased necking between the grains, and despite the higher porosity the biaxial strength increases.

The 3C $\rightarrow$ 6H phase transformation may also increase the biaxial strength of S-α60/β due to formation of plate-like grains, like those observed for S-β in Fig. 4.7d. However, similar morphology was not observed for S-α60/β, even though the Raman spectra presented in Fig. 4.14 confirmed the phase transformation. This is presumably because the phase content of 6H is much higher in P-α60/β than P-β, providing more nucleation sites for the α-SiC transformed from β-SiC.

According to Eom and Kim [56] this leads to many small grains, rather than few large grains, and the effect on the biaxial strength is therefore assumed to be small compared to that observed by Abderrazak [4]. The correlation between biaxial strength and density is therefore attributed to the phase transformation from 3C to 6H via gas phase, as this facilitates for better necking between grains.

6 Conclusion

The present study has investigated the effect of using α-SiC and β-SiC as sintering aids for spark plasma sintering of a coarse α-SiC powder. The samples were successfully sintered to cohesive samples and a method of qualitative phase analysis was established.

A relative density of 73 % was obtained for the as-received P-α60 after spark plasma sintering. Addition of 10 wt% α-SiC and 10 wt% β-SiC increased the relative density to 78 % and 76 %, respectively. The sintered samples demonstrated a homogeneous microstructure with open porosity. Plate-like morphology identified as the 6H polytype was revealed by SEM imaging of the fracture surfaces of samples containing β-SiC before sintering.

X-ray diffraction of the as-received powders and powder mixtures established the presence of polytypes 4H, 6H and 15R. Raman spectroscopy further confirmed that 3C was the main phase of the P-β powder. Quantitative phase analysis of X-ray diffractograms by Rietveld refinement concluded that 6H was the main phase of P-α60 and P-α. After sintering, 4H, 6H and 15R were identified by XRD, but Raman spectroscopy showed that no 3C was present. It was concluded that a phase transformation from 3C to 6H had occurred during SPS.

The effect of sintering aids was evident on the estimated biaxial strength from the ball-on-ring tests. The highest biaxial strength was measured for S-α60/β, with a mean of 21 MPa. The higher strength despite lower density compared to S-α60/α was attributed to better necking due to the 3C $\rightarrow$ 6H phase transformation via evaporation-condensation. The apparent hardness decreased with increasing porosity, modulus of elasticity and biaxial strength, but the high degree of porosity and crushing of the surface yields high uncertainty of these results.

7 Further Work

To fully isolate the effect of using α-SiC and β-SiC as sintering aids all parameters except the polytype should be identical. This includes the phase purity and particle size distributions, which were not identical in the present study. A study conducted at different sintering temperatures and holding times could further help establish the conditions at which this phase transformation is initiated. This would help minimize the energy required to obtain the desired properties.

Because the sintered samples demonstrated high porosity, reduction of the grain size and optimization of the sintering program is recommended if higher density is desired. To produce samples of low density and high strength it would be interesting to increase the amount of β-SiC, as the phase transformation induced by spark plasma sintering appears to be beneficial for the biaxial strength. Further investigations of the sample microstructures may also give information on the area of the necks formed during SPS. To improve the validity of the results, more samples must be sintered to perform further analyses and mechanical testing. The Weibull modulus of the samples could then be calculated to obtain more information on the homogeneity of the microstructure.

Bibliography

[1] A. C. Sparavigna, "The Invention of Carborundum, the Synthetic Silicon Carbide," *Philica*, 2018.

[2] D. W. Richerson and W. E. Lee, *Modern Ceramic Engineering*. Boca Raton, Florida: Taylor & Francis, 2018.

[3] S. Nakashima and H. Harima, "Raman investigation of SiC polytypes," *Physica status solidi (a)*, vol. 162, no. 1, pp. 39–64, 1997.

[4] H. Abderrazak and E. S. B. H. Hmida, "Silicon carbide: Synthesis and properties," in *Properties and Applications of Silicon Carbide* (R. Gerhardt, ed.), ch. 16, Rijeka: IntechOpen, 2011.

[5] V. A. Izhevskyi, "Review article: Silicon carbide. structure, properties and processing.," *Scielo Brazil*, vol. 46, no. 297, pp. 4–13, 2000.

[6] G. L. Harris, *Properties of Silicon Carbide*. Washington DC: Inspec, 1995.

[7] K. Biswas, "Solid state sintering of SiC-ceramics," *MSF*, vol. 624, pp. 71–89, 2009.

[8] D. A. Ray, S. Kaur, R. A. Cutler, and D. K. Shetty, "Effect of additives on the activation energy for sintering of silicon carbide.," *Journal of the American Ceramic Society*, vol. 91, no. 4, pp. 1135 – 1140, 2008.

[9] F. Bechstedt, P. Käckell, A. Zywietz, K. Karch, B. Adolph, K. Tenelsen, and J. Furthmüller, "Polytypism and properties of silicon carbide," *Physica status solidi (b)*, vol. 202, no. 1, pp. 35–62, 1997.

[10] S. Jayakumari, *Formation and characterization of β-and α-Silicon Carbide produced during Silicon/Ferrosilicon process*. PhD thesis, 2020.

[11] K. Momma and F. Izumi, "*VESTA3* for three-dimensional visualization of crystal, volumetric and morphology data," *Journal of Applied Crystallography*, vol. 44, pp. 1272–1276, Dec 2011.

[12] P. Pirouz and J. W. Yang, "Polytypic transformations in SiC: the role of tem," *Ultramicroscopy*, vol. 51, no. 1, pp. 189–214, 1993.

[13] M. Carl, "Influence of sintering environment on the spark plasma sintering of maxthal 312 (nominally-Ti_3SiC_2) and the role of powder particle size on densification," *Journal of Alloys and Compounds*, vol. 801, 2019.

[14] M. Weller, T. Overton, J. Rourke, and F. Armstrong, *Inorganic Chemistry*. Glasgow, Scotland: Oxford University Press, 2014. Chapter 2.

[15] T. Kimoto and J. A. Cooper, *Fundamentals of Silicon Carbide Technology. Growth, Characterization, Devices and Applications*. Singapore: John Wiley & Sons, 2014. Ch. 2.

[16] "Washington mills - silicon carbide properties." https://www.washingtonmills.com/silicon-carbide/sic-properties, 2021. Accessed: 23.01.2022.

[17] Z. Ren, P. Jin, X. Cao, Y. Zheng, and J. Zhang, "Mechanical properties and slurry erosion resistance of SiC ceramic foam/epoxy co-continuous phase composite," *Composites Science and Technology*, vol. 107, pp. 129–136, 2015.

[18] K. Yamada and M. Mohri, *Properties and Applications of Silicon Carbide Ceramics*. Dordrecht, Netherlands: Springer, 1991. Ch. 1.

[19] W. F. Knippenberg, "Growth phenomena in silicon carbide," *Philips Research Reports*, vol. 18, no. 3, pp. 161–274, 1963.

[20] P. Raj, G. S. Gupta, and V. Rudolph, "Silicon carbide formation by carbothermal reduction in the acheson process: A hot model study," *Thermochimica acta*, vol. 687, 2020. 178577.

[21] L. Lilja, *4H-SiC Epitaxy Investigating Carrier Lifetime and Substrate Off-Axis Dependence*. PhD thesis, Linköping, Sweden, Dec. 2018.

[22] P. J. Wellmann, "Power electronic semiconductor materials for automotive and energy saving applications – SiC, GaN, Ga_2O_3, and diamond," *Zeitschrift für anorganische und allgemeine Chemie*, vol. 643, no. 21, pp. 1312–1322, 2017.

[23] A.-K. Søiland, "Silicon for solar cells," 2004.

[24] R. N. Hall, "Electrical contacts to silicon carbide," *Journal of Applied Physics*, vol. 29, no. 6, pp. 914–917, 1958.

[25] L. Ottem, "Løselighet og termodynamiske data for oksygen og karbon i flytende legeringer av silisium og ferrosilisium," 1993.

[26] K. Yanaba, Y. Matsumura, T. Narushima, and Y. Iguchi, "Effect of alloying elements on carbon solubility in liquid silicon equilibrated with silicon carbide," *Materials Transactions, JIM*, vol. 39, no. 8, pp. 819–823, 1998.

[27] H. Dalaker and M. Tangstad, "The solubility of carbon in liquid silicon and its dependence on the boron levels," 2008.

[28] I. J. McColm and N. J. Clark, *Forming, Shaping and Working of High-Performance Ceramics*. Blackie and Son, 1988.

[29] H. Djohari, J. I. Martínez-Herrera, and J. J. Derby, "Transport mechanisms and densification during sintering: I. viscous flow versus vacancy diffusion," *Chemical Engineering Science*, vol. 64, no. 17, pp. 3799–3809, 2009.

[30] H. Djohari and J. Derby, "Transport mechanisms and densification during sintering: Ii. grain boundaries," *Chemical Engineering Science - Chem Eng Sci*, vol. 64, 2009.

[31] T. Molla, *Modeling Macroscopic Shape Distortions during Sintering of Multilayers*. PhD thesis, 2014.

[32] S.-J. L. Kang, "11 - grain growth and densification in porous materials," in *Sintering*, pp. 145–170, Oxford: Butterworth-Heinemann, 2005.

[33] A. K. Mohamed, "Ceramics: Sintering and microstructure," 2010.

[34] M. N. Rahaman, *Ceramic Processing and Sintering*. Marcel Dekker, Inc, 1995.

[35] S. Skjelstad, "Environmentally friendly substitute of phenolic resin in solid state sintered silicon carbide," 2020.

[36] R. M. German, "Sintering simplified: Surface area, density, and grain size relations," *Materials Science Forum*, vol. 835, pp. 50–75, 2016.

[37] M. Suárez, A. Fernández, J. L. Menéndez, R. Torrecillas, H. U. Kessel, J. Hennicke, R. Kirchner, and T. Kessel, "Challenges and opportunities for spark plasma sintering: A key technology for a new generation of materials," in *Sintering Applications*, ch. 13, Rijeka, Italy: IntechOpen, 2013.

[38] O. Guillon, J. Gonzalez-Julian, B. Dargatz, T. Kessel, G. Schierning, J. Räthel, and M. Herrmann, "Field-assisted sintering technology/spark plasma sintering: Mechanisms, materials, and technology developments," *Advanced Engineering Materials*, vol. 16, no. 7, pp. 830–849, 2014.

[39] Z. Y. Hu, Z. H. Zhang, X. Cheng, F. C. Wang, Y. F. Zhang, and S. L. Li, "A review of multi-physical fields induced phenomena and effects in spark plasma sintering: Fundamentals and applications," *Materials & Design*, vol. 191, p. 108662, 03 2020.

[40] A. M. Locci, A. Cincotti, S. Todde, R. Orrù, and G. Cao, "A methodology to investigate the intrinsic effect of the pulsed electric current during the spark plasma sintering of electrically conductive powders," *Science and Technology of Advanced Materials*, vol. 11, no. 4, p. 045005, 2010.

[41] S. Diouf and A. Molinari, "Densification mechanisms in spark plasma sintering: Effect of particle size and pressure," *Powder Technology*, vol. 221, pp. 220–227, 2012.

[42] J. Diatta, G. Antou, N. Pradeilles, and A. Maître, "Numerical modeling of spark plasma sintering — discussion on densification mechanism identification and generated porosity gradients," *Journal of the European Ceramic Society*, vol. 37, no. 15, pp. 4849–4860, 2017.

[43] T. Yamamoto, H. Kitaura, Y. Kodera, T. Ishii, M. Ohyanagi, and Z. A. Munir, "Consolidation of nanostructured β-SiC by spark plasma sintering," *Journal of the American Ceramic Society*, vol. 87, no. 8, pp. 1436–1441, 2004.

[44] A. Montón, F. Maury, G. Chevallier, C. Estournès, M. Ferrato, and D. Grossin, "Densification of surface-modified silicon carbide powder by spark-plasma-sintering," *Journal of the European Ceramic Society*, vol. 41, no. 15, pp. 7543–7551, 2021.

[45] S. Vajpai, N. Z. Khalil, M. Ota, and K. Ameyama, "Effect of particle size distribution on SiC ceramic sinterability," *Materials transactions*, vol. 56, 12 2015.

[46] M.-A. Jensen, M. S.and Einarsrud and T. Grande, "Preferential grain orientation in hot pressed tib2," *Journal of the American Ceramic Society*, vol. 90, no. 4, pp. 1339–1341.

[47] J. K. Lee, J. G. Park, E. G. Lee, D. S. Seo, and Y. Hwang, "Effect of starting phase on microstructure and fracture toughness of hot-pressed silicon carbide," *Materials Letters*, vol. 57, no. 1, pp. 203–208, 2002.

[48] H. J. Skarpeid, "The effect of carbon and boron carbide additions in pressure assisted sintered silicon carbide," 2017.

[49] P. Elder and V. Krstic, "Effect of surface area on densification of β-sic powders below 2000° c," *Journal of materials science letters*, vol. 8, no. 8, pp. 941–943, 1989.

[50] M. S. Dutta, A. Bandyopadhyay, and B. Chaudhuri, "Sintering of nano crystalline */alpha* silicon carbide by doping with boron carbide," *Bulletin of Materials Science*, vol. 25, pp. 181–189, 06 2002.

[51] D. Lundqvist, "On the crystal structure of silicon carbide and its content of impurities," *Acta Chemica Scandinavica*, vol. 2, no. 1, p. 177, 1948.

[52] M. Lodhe, N. Chawake, D. Yadav, and M. Balasubramanian, "On correlation between $\beta \longrightarrow \alpha$ transformation and densification mechanisms in SiC during spark plasma sintering," *Scripta Materialia*, vol. 115, pp. 137–140, 2016.

[53] H. Tanaka, N. Hirosaki, T. Nishimura, D. Shin, and S. Park, "Nonequiaxial grain growth and polytype transformation of sintered α-silicon carbide and β-silicon carbide," *Journal of the American Ceramic Society*, vol. 86, no. 12, pp. 2222–2224, 2003.

[54] A. Ortiz, F. Sánchez-Bajo, F. L. Cumbrera, and F. Guiberteau, "X-ray powder diffraction analysis of a silicon carbide-based ceramic," *Materials Letters*, vol. 49, no. 2, pp. 137–145, 2001.

[55] S. Kukushkin and A. Osipov, "Techniques for polytypic transformations in silicon carbide," *Phys. Solid State*, vol. 61, pp. 1389–1393, 2019.

[56] J.-H. Eom and Y.-W. Kim, "Effect of initial α-phase content on microstructure and flexural strength of macroporous silicon carbide ceramics," *Metals and materials international*, vol. 18, no. 2, pp. 379–383, 2012.

[57] G. Bernard-Granger and C. Guizard, "Spark plasma sintering of a commercially available granulated zirconia powder: I. sintering path and hypotheses about the mechanism(s) controlling densification," *Acta Materialia*, vol. 55, no. 10, pp. 3493–3504, 2007.

[58] S. Stølen and T. Grande, *Surfaces, Interfaces and Adsorption*, ch. 6, pp. 157–195. John Wiley & Sons, Ltd, 2003.

[59] Z. Xu, L. Liu, and Z. He, "Nanocutting mechanism of 6h-SiC investigated by scanning electron microscope online observation and stress-assisted and ion implant-assisted approaches.," *Int J Adv Manuf Technol*, vol. 106, p. 3869–3880, 2020.

[60] V. V. Pujar and J. D. Cawley, "Effect of stacking faults on the x-ray diffraction profiles of β-SiC powders," *Journal of the American Ceramic Society*, vol. 78, no. 3, pp. 774–782, 1995.

[61] A. Chauhan and P. Chauhan, "Powder xrd technique and its applications in science and technology," *J Anal Bioanal Tech*, vol. 5, no. 212, 2014.

[62] A. Ortiz, F. Sánchez-Bajo, N. P. Padture, F. L. Cumbrera, and F. Guiberteau, "Quantitative polytype-composition analyses of SiC using x-ray diffraction: a critical comparison between the polymorphic and the rietveld methods," *Journal of the European Ceramic Society*, vol. 21, no. 9, pp. 1237–1248, 2001.

[63] D. W. Baker, H. R. Wenk, and J. M. Christie, "X-ray analysis of preferred orientation in fine-grained quartz aggregates," *The Journal of Geology*, vol. 77, no. 2, pp. 144–172, 1969.

[64] H. A. Melia, C. T. Chantler, L. F. Smalea, and A. J. Illiga, "The characteristic radiation of copper kα1,2,3,4," *Acta Cryst*, vol. 75, no. 3, pp. 527–540, 2019.

[65] P. Vandenabeele, *Theoretical Aspects*, ch. 1, pp. 1–38. John Wiley & Sons, Ltd, 2013.

[66] P. Colomban and G. Gouadec, *Raman Scattering : Theory and Elements of Raman Instrumentation*, pp. 11–29. 01 2008.

[67] S. I. Nakashima, M. Higashihira, K. Maeda, and H. Tanaka, "Raman scattering characterization of polytype in silicon carbide ceramics: Comparison with x-ray diffraction," *Journal of the American Ceramic Society*, vol. 86, no. 5, pp. 823–829, 2003.

[68] R. Püsche, M. Hundhausen, L. Ley, K. Semmelroth, F. Schmid, G. Pensl, and H. Nagasawa, "Temperature induced polytype conversion in cubic silicon carbide studied by raman spectroscopy," *Journal of Applied Physics*, vol. 96, no. 10, pp. 5569–5575, 2004.

[69] N. H. MacMillan, "The theoretical strength of solids," *Journal of Materials Science*, vol. 7, no. 2, pp. 239–254, 1972.

[70] R. J. Stokes, pp. 343–400. US Government Printing Office, Washington, DC: NBS Special Publication, 1972.

[71] J. R. Kelly, "Perspectives on strength," *Dental Materials*, vol. 11, no. 2, pp. 103–110, 1995.

[72] F. P. Knudsen, "Dependence of mechanical strength of brittle polycrystalline specimens on porosity and grain size," *Journal of the American Ceramic Society*, vol. 42, no. 8, pp. 376–387, 1959.

[73] L. Li and M. Aubertin, "A general relationship between porosity and uniaxial strength of engineering materials," *Canadian Journal of Civil Engineering*, vol. 30, pp. 644–658, 02 2011.

[74] E. Ryshkewitch, "Compression strength of porous sintered alumina and zirconia," *Journal of the American Ceramic Society*, vol. 36, no. 2, pp. 65–68, 1953.

[75] J. S. Ramos, "Influence of the geometry of ceramic specimens on biaxial flexural strength: experimental testing and finite element analysis.," *Cerâmica [online]*, vol. 64, no. 369, pp. 120–125, 2018.

[76] R. Morrell, "Biaxial flexural strength testing of ceramic materials.," measurement good practice guide, Teddington, December 2007.

[77] G. de With and H. H. M. Wagemans, "Ball-on-ring test revisited," *Journal of the American Ceramic Society*, vol. 72, no. 8, pp. 1538–1541, 1989.

[78] K. Wan, W. Zhu, and G. Pezzotti, "Methods of piezo-spectroscopic calibration of thin-film materials: I. ball-on-ring biaxial flexure," *Measurement Science and Technology*, vol. 17, p. 181, 12 2005.

[79] A. F. Kirstein and R. M. Woolley, "Symmetrical bending of thin circular elastic plates on equally spaced point supports," *J. Res. Natl. Bur. Stand. C*, vol. 71C, no. 1, pp. 1–10, 1967.

[80] W. A. Bassali, "The transverse flexure of thin perforated elastic plates supported at several points," *Mathematical Proceedings of the Cambridge Philosophical Society*, vol. 53, no. 3, p. 744–754, 1957.

[81] S.-H. Chae, J.-H. Zhao, D. Edwards, and P. Ho, "Verification of ball-on-ring test using finite element analysis," pp. 1–6, 06 2010.

[82] D. K. Shetty, A. R. Rosenfield, W. H. Duckworth, and P. R. Held, "A biaxial-flexure test for evaluating ceramic strengths," *Journal of the American Ceramic Society*, vol. 66, no. 1, pp. 36–42, 1983.

[83] P. M. McGuiggan, J. S. Wallace, D. T. Smith, I. Sridhar, Z. W. Zheng, and K. L. Johnson, "Contact mechanics of layered elastic materials: experiment and theory," *Journal of Physics D: Applied Physics*, vol. 40, pp. 5984–5994, sep 2007.

[84] H. M. Westergaard, "Stresses in concrete pave- ments computed by theoretical analysis," *Public Roads*, vol. 7, no. 2, pp. 25–35, 1926.

[85] H. L. Frandsen, "The small displacement elastic solution to the ball-on-ring testing method," *Mechanics of Materials*, vol. 55, pp. 33–40, 2012.

[86] H. L. Frandsen, "Weibull statistics effective area and volume in the ball-on-ring testing method," *Mechanics of Materials*, vol. 73, pp. 28–37, 2014.

[87] A. E. Lupercio, E. Moshkelgosha, R. C. Winters, C. Doyle, M. Mamivand, A. T. Nelson, and B. J. Jaques, "Ball-on-ring test validation for equibiaxial flexural strength testing of engineered ceramics," *Journal of the American Ceramic Society*, vol. 3, no. 3, 2021.

[88] K. Herrmann, *Hardness Testing: Principles and Applications*. ASM International, 2011.

[89] W. D. J. Callister and D. G. Rethwisch, *Materials Science and Engineering: An Introduction*, ch. 9. Wiley, 2020.

[90] J. Wade-Zhu, S. Ghosh, P. Claydon, and H. Wu, "Contact damage of silicon carbide ceramics with different grain structures measured by hertzian and vickers indentation," *Journal of the European Ceramic Society*, vol. 35, pp. 1725–1736, 2015.

[91] Y. Milman, S. Chugunova, I. Goncharova, T. Chudoba, W. Lojkowski, and W. Gooch, "Temperature dependence of hardness in silicon–carbide ceramics with different porosity," *International Journal of Refractory Metals and Hard Materials*, vol. 17, no. 5, pp. 361–368, 1999.

[92] S. Brown, J. Cherry, H. Davies, S. Mehmood, N. Lavery, and J. Sienz, "Investigation into the effect of process parameters on microstructural and physical properties of 316l stainless steel parts by selective laser melting," *International Journal of Advanced Manufacturing Technology*, 02 2014.

[93] R. W. Rice, C. C. Wu, and F. Boichelt, "Hardness–grain-size relations in ceramics," *Journal of the American Ceramic Society*, vol. 77, no. 10, pp. 2539–2553, 1994.

[94] P. G. Karandikar, G. Evans, S. Wong, and M. K. Aghajanian, *Effects of Grain Size, Shape and Second Phases on Properties of Sintered SiC*, pp. 67–81. John Wiley & Sons, Ltd, 2009.

[95] C. Pan, L. Zhang, W. Jiang, W. Setyawan, L. Chen, Z. Li, N. Liu, and T. Wang, "Grain size dependence of hardness in nanocrystalline silicon carbide," *Journal of the European Ceramic Society*, vol. 40, no. 13, pp. 4396–4402, 2020.

[96] G. D. Quinn and R. C. Bradt, "On the vickers indentation fracture toughness test," *Journal of the American Ceramic Society*, vol. 90, no. 3, pp. 673–680, 2007.

[97] G. Anstis, P. Chantikul, B. Lawn, and D. Marshall, "A critical evaluation of indentation techniques for measuring fracture toughness: I, direct crack measurements," *Journal of the American Ceramic Society*, vol. 64, no. 9, pp. 533–538, 1981.

[98] J. Yi, W. Xue, Z. Xie, W. Liu, L. Cheng, J. Chen, H. Cheng, and Y. Gao, "Enhanced toughness and hardness at cryogenic temperatures of silicon carbide sintered by sps," *Materials Science and Engineering: A*, vol. 569, pp. 13–17, 2013.

[99] M. D. Hayes, D. B. Edwards, and A. R. Shah, "Fractography basics," in *Fractography in Failure Analysis of Polymers* (M. D. Hayes, D. B. Edwards, and A. R. Shah, eds.), Plastics Design Library, pp. 48–92, Oxford: William Andrew Publishing, 2015.

[100] G. Manière, C.and Lee and E. Olevsky, "All-materials-inclusive flash spark plasma sintering," *Scientific Reports*, vol. 7, 11 2017.

[101] T. I. O. for Standardization (ISO), "Iso-14705-2016." https://yiqi-oss.oss-cn-hangzhou.aliyuncs.com/aliyun/71576/Company/Solution/20210705-691476658.pdf, 2016. Accessed 16.05.2022.

[102] K. Wiik, "Kinetics of reactions between silica and carbon," 1990.

[103] M. Tangstad, "Reaction rates of $2\,SiO_2 + SiC = 3\,SiO + CO$ in pellets at elevated temperatures," *Aspects Min Miner Sci.*, vol. 3, no. 2, 2019.

[104] S. Grasso, E.-Y. Kim, T. Saunders, M. Yu, A. Tudball, S.-H. Choi, and M. Reece, "Ultra-rapid crystal growth of textured sic using flash spark plasma sintering route," *Crystal growth design*, vol. 16, no. 4, pp. 2317–2321, 2016.

[105] J. K. Mackenzie, "The elastic constants of a solid containing spherical holes," *Proceedings of the Physical Society. Section B*, vol. 63, no. 1, pp. 2–11, 1950.

Appendix

A Coefficient of Variation

According to Khalil et al. [45], the coefficient of variation can be derived from Eq. (2.14). The weighted mean and the weighted standard deviation are calculated by Eq. (A.1) and Eq. (A.2), respectively.

$$\overline{X} = \Sigma_{i=1}^{n} x_i f_i / \Sigma_{i=1}^{n} f \tag{A.1}$$

$$s = \sqrt{\Sigma x^2 f - ((\Sigma x f)^2 / \Sigma f) / \Sigma f - 1} \tag{A.2}$$

Here x is the particle size and f is the frequency of particles for size x [45]. The results of the calculations are presented in Table A.1.

Table A.1: The weighted mean particle size, the weighted standard deviation and the calculated coefficient of variation of the as-received powders.

Powder	$\overline{X}$	**s**	$\mathbf{C}_V$
P-α60	70.6	37.7	0.5
P-α	5.9	2.3	1.4
P-β	22.0	31.6	0.4

B X-Ray Diffraction Patterns

Fig. B.1 presents the X-ray diffractograms of the as-received powders and powder mixtures after being stripped of CuK_{α}-2 contribution causing the peak splitting observed in Fig. 4.3.

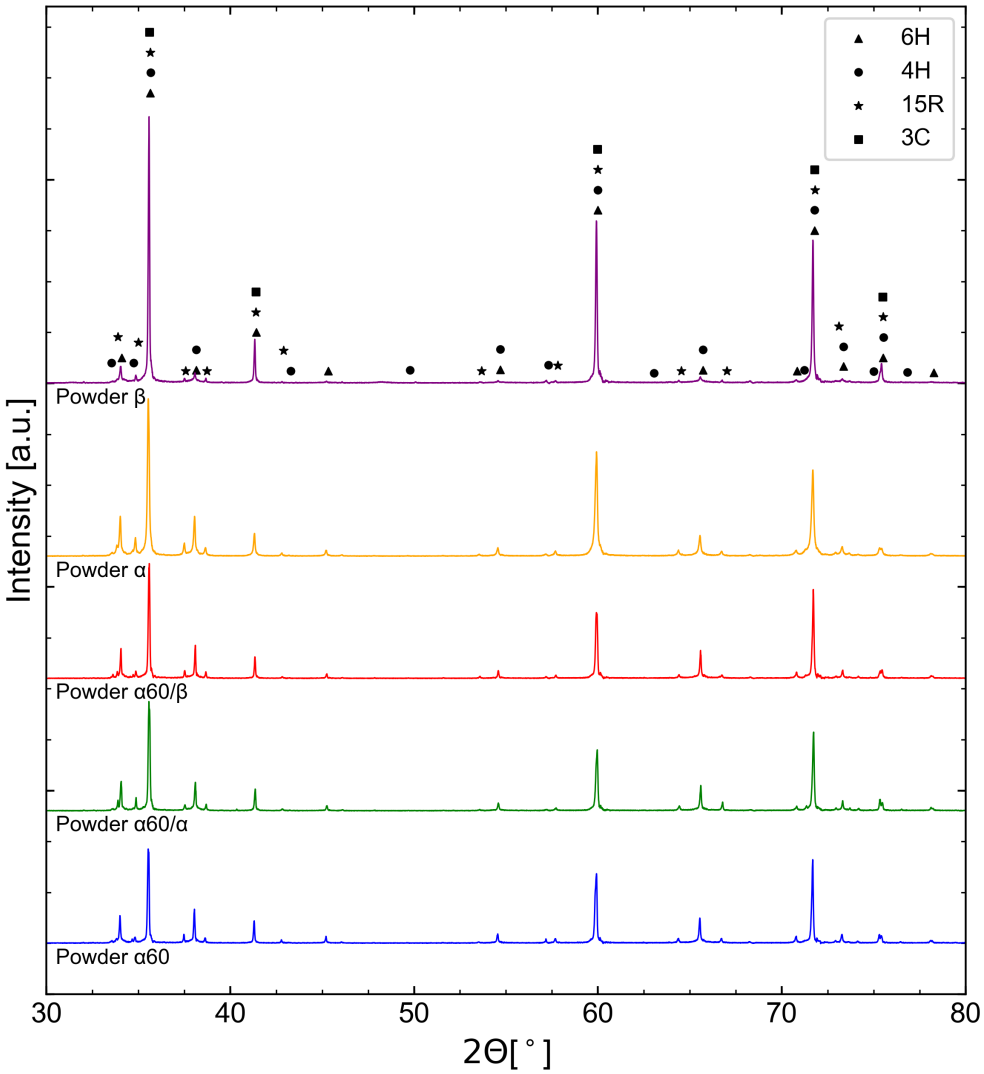

Figure B.1: X-ray diffractograms of as-received SiC-powders and powder mixtures where each polytype is identified by a marker.

C Density and Porosity Calculations

Tables C.1 and C.2 present the dimensions of the sintered samples, as well as the mass before, during and after immersion in isopropanol. These are further used to calculate the density and porosity of each sample, which are given in Table C.3. A calculation of each value is presented using S-α60-1 as an example.

Table C.1: The dimensions of the sintered samples measured with a caliper after polishing.

Sample	**Diameter** [mm]	**Height** [mm]
S-α60-1	28.41	3.49
S-α60-2	28.39	3.40
S-α60-3	28.53	3.48
S-α60/α-1	28.25	3.10
S-α60/α-2	28.11	3.39
S-α60/α-3	28.37	3.38
S-α60/β-1	28.30	3.20
S-α60/β-2	28.43	3.33
S-α60/β-3	28.44	3.34

Table C.2: The dry mass of each sample, the mass when emerged in isopropanol and the mass in air after immersion.

Sample	**Dry** (m_1) [g]	**In isopropanol** (m_2) [g]	**In air** (m_3) [g]
S-α60-1	4.8950	3.6882	5.3566
S-α60-2	5.1029	3.8480	5.5613
S-α60-3	4.9851	3.7458	5.4020
S-α60/α-1	4.6349	3.4993	4.9737
S-α60/α-2	4.7594	3.5973	5.0839
S-α60/α-3	4.9954	3.7796	5.3114
S-α60/β-1	4.8035	3.6266	5.1940
S-α60/β-2	4.9893	3.7599	5.3799
S-α60/β-3	4.8906	3.6890	5.2695

Apparent Density

The apparent density was calculated by Equation C.1 [2]

$$\rho = \frac{m_1}{\pi \cdot r^2 \cdot h} \tag{C.1}$$

where m_1 is the mass of the sintered sample and r and h are the radius and height of the sintered sample, respectively. Using S-α60-1 as an example, the calculation is as follows.

$$\rho_{a,S-\alpha60-1} = \frac{4.8950\,\mathrm{g}}{\pi \cdot 1.421\,\mathrm{cm}^2 \cdot 0.349\,\mathrm{cm}} = \underline{2.21\,\mathrm{g/cm^3}} \tag{C.2}$$

Bulk Density

The bulk density of the samples was calculated by

$$\rho_b = \frac{m_1}{m_3 - m_2} \cdot \rho_{liq} \tag{C.3}$$

where m_1 is the dry weight of the sample, m_2 is the weight when immersed in isopropanol, and m_3 is the weight in air directly after immersion [2]. ρ_{liq} is the density of isopropanol during weighing and is dependent on temperature. During weighing of S-α60-1 the temperature of isopropanol was measured at 18 °C, resulting in the following density.

$$\rho_{liq} = -0.0009 \cdot T + 0.8018 = \underline{0.818\,\mathrm{g/mL}} \tag{C.4}$$

Using the data from Table C.1 and Table C.2, the bulk density for each sample was calculated as for S-α60-1 below.

$$\rho_{b,S-\alpha60-1} = \frac{4.8950\,\mathrm{g}}{5.3566\,\mathrm{g} - 3.6882\,\mathrm{g}} \cdot 0.818\,\mathrm{g/mL} = 2.30\,\mathrm{g/mL} = \underline{2.30\,\mathrm{g/cm^3}} \tag{C.5}$$

Porosity

From the densities the total, closed and open porosity of each sample was calculated.

The total porosity was calculated by Equation C.6.

$$\text{Total porosity} = 1 - \frac{\rho_b}{\rho_\text{t}} \tag{C.6}$$

where ρ_t is the theoretical density of the material. For SiC this is $3.19\,\text{g/cm}^3$.

Further, open porosity was determined by Equation C.7.

$$\text{Open porosity} = \frac{m_3 - m_1}{m_3 - m_2} \tag{C.7}$$

The closed porosity can be calculated by Equation C.8.

$$\text{Closed porosity} = \text{Total porosity} - \text{Open porosity} \tag{C.8}$$

Finally, the relative density was calculated by Eq. (C.9).

$$\text{Relative density} = \frac{\rho_b}{\rho_t} \tag{C.9}$$

The results are included in Table C.3.

Table C.3: The apparent density, bulk density and relative density to theoretical density, as well as total porosity, closed porosity and open porosity of the sintered samples. Theoretical density used was $3.19\,\text{g/cm}^3$.

Sample	**Density** [g/cm^3]		**Density**[%]	**Porosity**[%]		
	Apparent	Bulk	Relative	Total	Closed	Open
S-α60-1	2.2	2.3	72	28	0	28
S-α60-2	2.4	2.3	73	27	0	27
S-α60-3	2.2	2.4	74	26	1	25
S-α60α-1	2.4	2.5	77	23	0	23
S-α60α-2	2.3	2.5	78	22	0	22
S-α60α-3	2.3	2.5	80	20	0	20
S-α60β-1	2.4	2.4	76	24	0	24
S-α60β-2	2.4	2.4	75	25	0	25
S-α60β-3	2.3	2.4	76	24	0	24

D Mechanical Properties

D.1 Preliminary Estimations of Biaxial Strength

The maximum load of the Instron 5543 mechanical load cell is 1 kN and a preliminary estimation of the sample strength was therefore performed to ensure fracture of the samples. Equations 2.17, 2.19 and 2.20 were solved using the data presented in Table D.1. For specimen with a porosity in the range 0 - 30 % the elastic modulus can vary as described by Eq. (D.1) [105][91]

$$E_1 = E_0 \frac{1}{1-2\nu_1}\left[(1-2\nu_1) - \frac{3}{2}(1-\nu_1)p\right] \tag{D.1}$$

where E_0 is the elastic modulus and ν_1 Poisson's ratio of the dense material, and p is the porosity.

Table D.1: Description of the parameters for equations 2.17 - 2.21.

Symbol	Description	Value	Unit
ν_1	Poisson's ratio of SiC	0.14	-
ν_2	Poisson's ratio of steel	0.33	-
a	Radius of ring holder	10.0	mm
b	Radius of loading ball	3.5	mm
E_0	Young's modulus of dense SiC	414	GPa
E_2	Young's modulus of steel	180	GPa
B	Empirical constant	7.0	-

The necessary load to achieve fracture was calculated by Eq. (D.2) and plotted for different sample thicknesses as a function of porosity as presented in Fig. D.1.

$$P = \frac{1}{\frac{3\sigma(1+\nu)}{4\pi t^2}\left[1 + 2\ln\left(\frac{a}{b_{eq}}\right) + \frac{1-\nu}{1+\nu}\left(1 - \frac{b_{eq}^2}{2a^2}\right)\frac{a^2}{R^2}\right]} \tag{D.2}$$

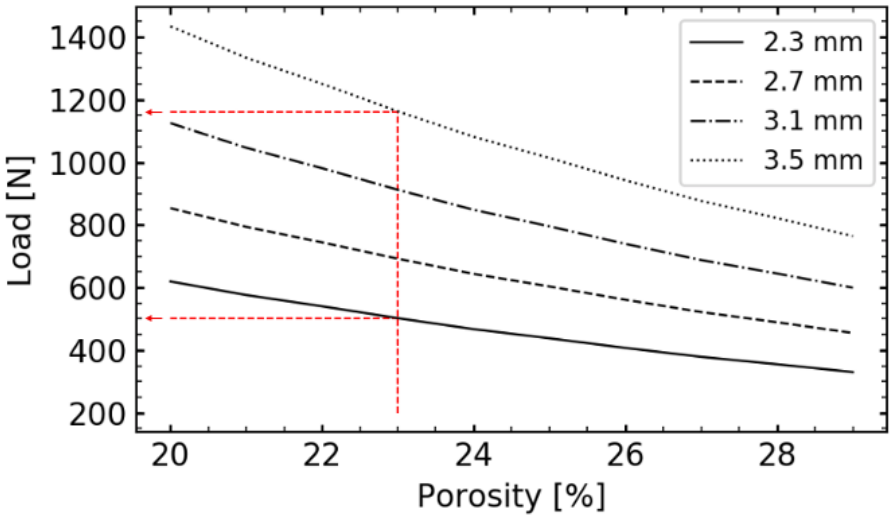

Figure D.1: The estimated load at which fracture will occur for a given porosity and sample thickness when performing the ball-on-ring test on sintered SiC.

Two samples of different thicknesses were then sintered to test their biaxial strength. Fig. D.2 presents the results of these experiments and shows that the necessary load was below what was expected from Fig. D.1 and the porosities in Table D.2. It was decided to continue using the 3.5 mm samples as they were less prone to edge defects after sintering.

Table D.2: The estimated elastic modulus, measured porosity, thickness and radius of the tested samples.

Sample	E_1 [GPa]	p [%]	t [mm]	R [mm]
S-α250	243	23	2.3	14.3
S-α250	243	23	3.5	14.3

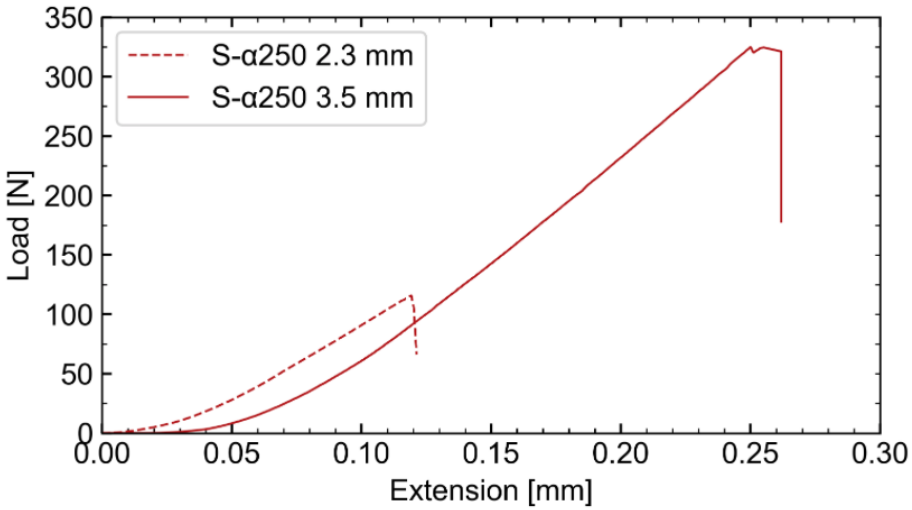

Figure D.2: The load applied to fracture a 2.3 mm and a 3.5 mm sample made of P-α250 using the ball-on-ring method.

D.2 Biaxial Strength Calculations from Ball-on-Ring

Equations 2.17, 2.19 and 2.20 were used to calculate the mean biaxial strength listed in Table 4.6 from data in Table D.1 and Table D.3. Data from the ball-on-ring tests were plotted as stress strain curves and the elastic modulus of the samples was estimated as the slope of the linear section of each curve. The thickness and diameter of the samples were measured by a digital caliper and the porosity by Archimedes method. Finally, the biaxial strength was calculated by Eq. (2.21).

Table D.3: The load at fracture, elastic modulus, porosity, thickness, radius and biaxial strength of each sintered sample.

Sample	**P [N]**	**E_1 [GPa]**	**p [%]**	**t [mm]**	**R [mm]**	**σ[MPa]**
S-α60-1	370	107	28	3.5	14.2	9
S-α60-2	293	77	27	3.4	14.2	8
S-α60-3	169	47	26	3.5	14.3	4
S-α60/α-1	462	91	23	3.1	14.1	19
S-α60/α-2	639	101	22	3.4	14.1	23
S-α60/α-3	429	57	20	3.4	14.1	17
S-α60/β-1	632	95	24	3.2	14.1	23
S-α60/β-2	603	89	25	3.3	14.2	19
S-α60/β-3	654	95	24	3.3	14.2	21

E Hardness

The apparent hardness of each sample is listed in Table E.1. The hardness was measured by Vickers micro-indentation and ten measurements were performed on each sample using a 2 kg load and a dwell time of 10 s. The mean hardness with standard deviation based on this table is presented in Section 4.6 and Section 4.6.

Table E.1: The apparent hardness measured for each composition of sintered samples using Vickers micro-indentation with 2 kg force and 10 s dwell time. Ten indents were made on each sample.

Sample	**Apparent Hardness [HV]**									
	1	**2**	**3**	**4**	**5**	**6**	**7**	**8**	**9**	**10**
S-α60	288	550	349	386	366	344	484	260	276	453
S-α60/α	252.2	155.3	104.0	184.3	110.1	184.0	166.8	204.3	176.5	187.8
S-α60/β	152.1	262.3	141.4	183.4	233.3	218.4	308.7	117.2	222.0	398.9